

**Effect of Stress Triaxiality on Constitutive Response and Failure of
Super Vacuum Die Cast AM60B Magnesium Alloy**

by

Dan Kraehling

A thesis
presented to the University of Waterloo
in fulfilment of the
thesis requirement for the degree of
Master of Applied Science
in
Mechanical Engineering

Waterloo, Ontario, Canada, 2014

© Dan Kraehling 2014

I hereby declare that I am the sole author of this thesis. This is a true copy of the thesis, including any required final revisions, as accepted by my examiners.

I understand that my thesis may be made electronically available to the public.

ABSTRACT

The effect of stress triaxiality on failure strain of as-cast magnesium alloy AM60B is examined. Experiments were performed on one uniaxial tension, two notched tension, and one near-biaxial hemispherical dome sample geometries to study the effect of stress triaxiality on the quasi-static constitutive and failure response of super vacuum die cast AM60B castings. Two sample material origins were used, introducing another variable; they were termed Phase I and Phase II. For all tests, local strains, failure location, and specimen elongation were tracked using two or three-dimensional digital image correlation (DIC) analysis. The uniaxial specimens were tested in two orthogonal directions to evaluate the anisotropy of the casting. The uniaxial and notched tensile specimens were tested at strain rates of 0.001 and 10 s^{-1} to determine the effect of strain rate on the constitutive response. Finite element models were developed to estimate effective plastic strain histories and stress state (triaxiality) as a function of notch severity.

Samples of all three tensile sample geometries consistently failed beginning at the notch root as opposed to the centre. They failed after accruing on average 14-16% effective plastic strain, and they also showed a marked lack of repeatability in the failure strain distribution, with a standard deviation on average 18% of the mean failure strain of each sample geometry. The Phase II samples showed significantly lower elongations to failure, which was attributed to elevated levels of porosity and segregated porosity bands. It was found that there is some degree of transverse anisotropy present in the AM60B castings (r -values of 1.0-1.1). The AM60B castings exhibit mild positive strain rate sensitivity, evidenced by an increase in maximum stress of 4-8% with a change in strain rate from 0.001 to 10 s^{-1} . Finally, higher stress triaxiality levels caused increases in maximum stress and decreases in elongation and local effective plastic strain at failure. This data will serve as the basis for the development of a damage-based constitutive model.

ACKNOWLEDGEMENTS

I would like to thank my supervisor, Professor Michael Worswick, for giving me the opportunity to undergo a MASc degree in his research group. I appreciate the time he was able to afford me and the talks we had together. His big picture ideas helped to enhance my small picture ideas by giving them more of a real-world purpose.

I would also like to express my appreciation for the financial support provided by the Magnesium Front-End Research and Development (MFERD) program, Tim Skszek and Cosma International, Automotive Partnership Canada (APC), the Natural Sciences and Engineering Research Council of Canada (NSERC), the Ontario Research Fund, and the Canada Research Chairs Secretariat.

Thank you to the diligent employees of the Engineering Machine Shop, particularly Rick Forgett, Mike Luckenhaus, Phill Laycock, Andrew Urschel, Jorge Cruz, and Fred Bakker, for a wide variety of support during the project.

I would like to acknowledge the guidance and support received from the members of the Forming and Impact Mechanics research group. In particular, thank you David Anderson, for helping me with my overall project progression, as well as instructing me on some of the finer points of using LS-DYNA. Thank you to José Imbert-Boyd for diligently managing the MFERD project for our research group. Thanks are also due to Alex Bardelcik for teaching me how to use the HISR and for answering all my technical questions.

The technical and administrative support staff at the University of Waterloo was indispensable in completing this work. A big thank you Eckhard Budziarek for helping me with countless odd jobs, including building a simple yet effective painting mount for my samples. Thank you to Jeff Wemp for his mastery of all things optical, and in particular, for his help in acquainting me with the use of the DIC system. Many thanks to Tom Gawel, Andy Barber, and Neil Griffett, for their collective support in using the equipment in the high pressure lab. Thanks are also due to Yuquan Ding for his assistance with using the SEM. Finally, a big kudos to Laurie

Wilfong, whose laser-like understanding of the prevailing rules, regulations, and many types of paperwork that were needed to be filled out was very reassuring in an otherwise uncertain environment.

And last but not least, a heartfelt thank you to my friends and family for their ever-present support and empathy. In particular, I would like to thank my parents, Paul and Zlata Kraehling, for always being there for me.

For my loving parents, Paul and Zlata Kraehling

TABLE OF CONTENTS

ABSTRACT.....	iii
ACKNOWLEDGEMENTS.....	iv
TABLE OF CONTENTS.....	vii
LIST OF FIGURES	ix
LIST OF TABLES.....	xiii
1 Introduction.....	1
1.1 Magnesium as a Structural Metal Candidate.....	1
1.2 Magnesium Crystallographic Structure.....	4
1.3 Constitutive Response of AM60B Magnesium.....	6
1.4 Characterization of Damage Processes within AM60B Magnesium.....	8
1.5 Current Research.....	13
2 Experimental Method	15
2.1 Material	15
2.2 Test Specimen Geometries.....	16
2.2.1 Tensile Specimens	16
2.2.2 Biaxial Specimens.....	18
2.3 Low Rate Tensile Test Method	19
2.4 High Rate Tensile Test Method	23
2.5 Biaxial Hemispherical Dome Test Method.....	25
2.6 Digital Image Correlation.....	27
2.7 Test Matrix	30
3 Experimental Results	32
3.1 Quantifying the Error Due to the Casting Process	32
3.2 Tensile Test Results	33
3.3 Hypothesis Tests	38
3.4 Anisotropy Evaluation.....	42
3.5 Considère Analysis.....	43
3.6 Effect of Strain Rate.....	45
3.7 Effect of Sampling Location within the Cast Component	46

3.8	Biaxial Hemispherical Dome Test Results.....	49
3.9	Metallographic Findings	53
3.10	Sandblasting Investigation.....	58
4	Numerical Model	60
4.1	General Approach	60
4.2	Tensile Model.....	60
4.3	Mesh Convergence Study	64
4.4	Biaxial Hemispherical Dome Test Model.....	66
5	Numerical Results.....	70
5.1	Numerical Tensile Model Results	70
5.2	Numerical Biaxial Hemispherical Dome Model Results	73
5.3	Stress Triaxiality and Failure Strain Trends.....	76
6	Discussion, Conclusions, and Future Work.....	80
6.1	Discussion	80
6.2	Conclusions	81
6.3	Future Work	82
	References.....	83
	Appendix A: Sample Characteristics	88
	Appendix B: Stress-Strain Curves	93

LIST OF FIGURES

Figure 1.1 – The hexagonal close packed (HCP) crystal structure of magnesium	4
Figure 1.2 – The twinning process, a) before, and b) after (taken from [8])	5
Figure 1.3 – Evidence of twinning in the tensile stress-strain response (taken from [18])	6
Figure 1.4 – Post-yield behaviour for AM60B across all tested strain rates (taken from [20])...	7
Figure 1.5 – Final strain to failure trend for specimens designed to exhibit a variety of stress triaxialities, and by extension, stress states (adapted from [22])	9
Figure 1.6 – The effective plastic strain levels reached upon failure, for a variety of stress states and materials [25] [26].....	10
Figure 1.7 – The collection of circumferentially notched tensile tests. Left: A schematic of the sample geometries adopted. Right: The resulting representative fracture surfaces, arranged as follows: a) R = 1 mm, b) R = 2 mm, c) R = 4 mm, and d) R = 8 mm (adapted from [27]).....	11
Figure 1.8 – An AM60B microstructure displaying a distinctive transition band.....	12
Figure 1.9 – Cross-sectional microstructures of, a) an AM60A sample, ready to be digitally analyzed in order to obtain an estimate of the volumetric porosity, b) an AM50 sample, exhibiting porosity segregation bands	13
Figure 2.1 – Top hat component, a) isometric view, b) die casting flow diagram, c) physical dimensions	15
Figure 2.2 – Tensile sample geometries used, a) uniaxial, b) a/R=0.25, c) a/R=1	17
Figure 2.3 – Top hat geometry with sample orientations	17
Figure 2.4 – An example of a biaxial hemispherical dome sample strained until fracture, and the blank/punch geometry [all stated dimensions in millimetres]	18
Figure 2.5 – Experimental setup for the quasi-static tests at a strain rate of 0.001 s^{-1}	19
Figure 2.6 – Lights and camera setup for the quasi-static tests at a strain rate of 0.001 s^{-1}	20
Figure 2.7 – A typical 0.001 s^{-1} test, showing engineering stress, strain, and instantaneous strain rate responses	22
Figure 2.8 – Experimental setup for the tests at a strain rate of 10 s^{-1}	24
Figure 2.9 – A typical 10 s^{-1} test, showing engineering stress, strain, and strain rate responses	24
Figure 2.10 – Experimental setup for the biaxial hemispherical dome tests, a) an overall view of the various systems involved, b) a close-up view of the lights and camera arrangement	25

Figure 2.11 – Schematic illustrating the stress state achieved in the hemispherical dome tests	26
Figure 2.12 – A typical speckle pattern, including digitally zoomed-in comparisons of the undeformed reference area of interest (AOI) to the deformed AOI. Subtle variations in pixel greyscale levels can be seen and are picked up by the image analysis software.	28
Figure 2.13 – Greyscale correlation between undeformed and deformed sub-images (taken from [48]).....	29
Figure 3.1 – Measured 0° uniaxial tensile test engineering stress-strain results	32
Figure 3.2 – An example Hencky first principal strain contour plot for an a/R=0.25 sample, at a nominal strain of 4.0%	34
Figure 3.3 – Median engineering stress-nominal strain curves for all stress states, orientations, and material origins under study.....	35
Figure 3.4 – Strength dependence on stress state and sample origin (sample means noted at the base of each column)	36
Figure 3.5 – Elongation to failure dependence on stress state and sample origin (sample means noted at the base of each column).....	36
Figure 3.6 – r-value curves of all Phase I uniaxial repeat tests.....	42
Figure 3.7 – The polynomial fits adopted for the Considère analysis	44
Figure 3.8 – Applying the Considère approach to selected Phase I 0° uniaxial tests	44
Figure 3.9 – Median engineering stress-nominal strain results for all geometries, orientations, and strain rates under study.....	45
Figure 3.10 – Selected 0° uniaxial tensile results, at a nominal strain rate of 0.001 s ⁻¹	47
Figure 3.11 – Selected 0° a/R = 0.25 tensile results, at a nominal strain rate of 0.001 s ⁻¹	48
Figure 3.12 – Selected 0° a/R = 1 tensile results, at a nominal strain rate of 0.001 s ⁻¹	48
Figure 3.13 – DIC contour plots of Hencky major strain, showing examples of the three observed failure locations, a) at the centre (expected), b) at the die fillet radius, and c) at an off-centre dome defect	50
Figure 3.14 – Force-displacement results of the biaxial hemispherical dome tests.....	51
Figure 3.15 – Major and minor strain plots obtained from the biaxial hemispherical dome tests, a) major strain vs. displacement, b) minor strain vs. displacement, c) minor/major strain ratio vs. displacement, d) major strain vs. minor strain	52
Figure 3.16 – Using pixel greyscale levels to determine void boundaries (in red)	54

Figure 3.17 – Example optical micrograph set displaying the length-thickness plane of a) a failed Phase I sample (M=8x), b) an untested Phase II sample (M=6.25x).....	54
Figure 3.18 – Example Phase I SEM fractographs displaying the width-thickness plane, a) uniaxial, b) a/R=0.25, c) a/R=1.....	56
Figure 3.19 – Example Phase II SEM fractographs displaying the width-thickness plane, a) uniaxial, b) a/R=0.25, c) a/R=1.....	56
Figure 3.20 – Random representative Phase II 0° oriented SEM micrographs (M=500x) taken near the centre of each fracture surface, a) uniaxial, b) a/R=0.25, c) a/R=1	57
Figure 3.21 – Optical micrographs (M=5x) of the nominally 2.8 mm thick unpolished length-thickness planes, a) pre-sandblasting, b) post-sandblasting.....	59
Figure 4.1 – Finite element meshes used, a) uniaxial tension, b) a/R=0.25 notched tension, c) a/R=1 notched tension.....	61
Figure 4.2 – Selected uniaxial tension results compared with proposed model curves demonstrating the sensitivity of the Ling parameter.....	63
Figure 4.3 – Using the maximum $\bar{\varepsilon}^p$ reached at the centre of the specimen as the optimization standard for the uniaxial tension mesh convergence study.....	65
Figure 4.4 – Converging towards the true $\bar{\varepsilon}^p$ level found at the geometric centre of the maximum elongation to failure experimental test, along with the computational time that was required in order to obtain it	66
Figure 4.5 – A detailed view of the mesh of the blank, which included transition elements on the x-y plane.....	67
Figure 4.6 – The four parts and their relative arrangements in the biaxial hemispherical dome test model, a) undeformed state, b) deformed state (15 mm displacement)	69
Figure 5.1 – Comparing model predicted engineering stress-nominal strain response to measured results.....	70
Figure 5.2 – Comparison of measured results (left) to model predicted results (right) for an a/R=0.25 sample, at a nominal strain of 4.0%	71
Figure 5.3 – Gauge length expansion versus width contraction for the a/R=0.25 geometry.....	72
Figure 5.4 – Gauge length expansion versus width contraction for the a/R=1 geometry.....	72

Figure 5.5 – Comparing model predictions to measured biaxial hemispherical dome data, a) force vs. displacement, b) major strain vs. displacement, c) minor strain vs. displacement, d) major strain vs. minor strain	73
Figure 5.6 – Comparison of predicted first principal strain contours (top-right quadrant) to measured results for a biaxial hemispherical dome test sample just prior to failure	74
Figure 5.7 – Von Mises stress contour plots of the biaxial hemispherical dome test, after the punch has displaced the blank by 13.9 mm, a) top/DIC camera facing surface view, b) bottom/punch contacting surface view	75
Figure 5.8 – Von Mises stress history at two distinct points on the specimen: the centre and the edge where the sample comes into contact with the die fillet radius.....	76
Figure 5.9 – $\overline{\varepsilon^p}$ histories at the centre and notch root on the specimen for the four geometries under study.....	77
Figure 6.1 – DIC image showing crack initiation beginning from the left notch root on an a/R=0.25 sample (elongation to failure = 4.2%).....	80

LIST OF TABLES

Table 1.1 – Comparison of Physical and Mechanical Properties of Various Materials [1].....	2
Table 1.2 – Comparison of Normalized Mechanical Properties of Various Materials.....	2
Table 1.3 – The elemental composition of AM60B [6].....	3
Table 1.4 – Average Tensile Mechanical Properties of AM60B (adapted from [20])	7
Table 2.1 – Test matrix for the main parameters that were tested.....	31
Table 3.1 – The actual nominal strain rates imparted upon the three different tensile sample geometries	37
Table 3.2 – The elongation to failure of all 0.001 s ⁻¹ 0° uniaxial tests (all figures in percent engineering strain)	39
Table 3.3 – A summary of the basic statistics	39
Table 3.4 – Significant difference summary matrix: Engineering stress at 2% nominal strain. 41	41
Table 3.5 – Significant difference summary matrix: Elongation to failure	41
Table 4.1 – Number of elements and solution time for each sample geometry.....	61
Table 4.2 – Number of elements used in the biaxial hemispherical dome test model, as seen in Figure 4.6.....	68
Table 5.1 – Average equivalent strain, stress triaxiality, and $\overline{\varepsilon^p}$ at failure for each of the three tensile geometries.....	79

1 INTRODUCTION

Transportation relies on the incorporation of materials of high strength and low weight. Focussing on the low weight end of the spectrum, magnesium is the lightest structural metal [1]. Elemental magnesium has a density of 1.74 g/cc, compared to 2.70 g/cc for aluminum and 7.87 g/cc for iron and steel. In the long term, therefore, it would be reasonable to expect magnesium to become more prevalent in our daily lives. If magnesium's ductility, energy absorbing abilities, and corrosion susceptibility can be improved upon, it may one day be the primary material of choice for use in transportation technologies.

1.1 Magnesium as a Structural Metal Candidate

In terms of magnesium's availability on the planet, it is in fact very plentiful. The Earth's crust and mantle has been estimated to contain 22.8 wt% magnesium, making it the world's second most abundant element, after only oxygen [2]. If we compare this value to iron's abundance, at 6.26 wt%, it doesn't seem like an overly large disparity [2]. However, after normalizing the weight percentages into volume percentages, it can be concluded that magnesium occupies roughly 15 times as much space in the crust and mantle as does iron. Aluminum works out to a similar conclusion. As a weight percentage aluminum makes up 2.35 wt% of the crust and mantle, and after converting to a volume basis it is again found that magnesium occupies roughly 15 times as much space as aluminum does [2].

Materials are seldom used in their elemental form, however. It is only by the intelligent design of alloy systems that the potential of the various elements can be fully brought out. In Table 1.1, representative alloys of the three previously discussed metals are compared with each other, and also with a polymer, which competes with magnesium on the low end of the weight spectrum.

Material	AM50 Mg	AISI 1015 Steel, as rolled	A6061-T6 Al	Plastics (PC/ABS)
Process/Product	die cast	sheet	extrusion	injection molding
Density [$\text{g}\cdot\text{cc}^{-1}$]	1.77	7.87	2.70	1.13
Elastic Modulus [GPa]	45	200	69	2.3
Yield Strength [MPa]	125	315	275	53
Ultimate Tensile Strength [MPa]	210	420	310	55
Elongation [%]	10	39	12	125

Table 1.1 – Comparison of Physical and Mechanical Properties of Various Materials [1]

Looking at the mechanical properties first, it is clear that steel is the best performing material. However, the conclusion changes if the properties are normalized by their densities (“specific” properties), as presented in Table 1.2.

Material	AM50 Mg	AISI 1015 Steel, as rolled	A6061-T6 Al	Plastics (PC/ABS)
Elastic Modulus/Density [$\text{GPa}\cdot\text{cc}\cdot\text{g}^{-1}$]	25	25	26	2
Yield Strength/Density [$\text{MPa}\cdot\text{cc}\cdot\text{g}^{-1}$]	71	40	102	47
Ultimate Tensile Strength/Density [$\text{MPa}\cdot\text{cc}\cdot\text{g}^{-1}$]	119	53	115	49
Price [$\text{\$USD}\cdot\text{kg}^{-1}$] [3]	\$3.00	\$0.70	\$2.40	\$2.00

Table 1.2 – Comparison of Normalized Mechanical Properties of Various Materials

The specific elastic moduli and specific elongation numbers of the three types of metals are comparable, but AM50 magnesium and A6061-T6 aluminum far outperform steel in terms of specific yield strength and specific ultimate tensile strength. Now, this is not to say that steel is always inferior in specific strength to these other options. There exist certain types of steel that exhibit >1 GPa in strength, such as boron-alloyed steel [4], which compromises on ductility.

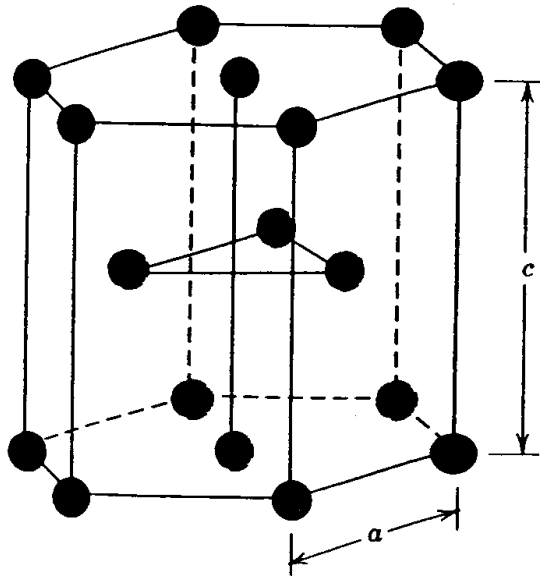
Included in Table 1.2 is the current approximate price of each material. Magnesium is the most expensive, so it is relegated to use either sparingly in specific weight-critical components, or in higher priced luxury cars. Aluminum is a direct competitor to magnesium, as it shows similar specific mechanical performance, but it does so at a slightly cheaper price. As the demand for magnesium alloys increases, the more mass-production operations will be instituted which in turn will drive price down. In fact, the price may eventually be lower than that of aluminum, as the vast reserves of magnesium locked away on the planet may suggest as inevitable. In order to prepare for this, characterization work is necessary now, so that if and when magnesium is the best material choice for economic reasons, a more seamless transition can be had when companies compete to be first to market. One area that requires characterization is the understanding of how the full range of different stress states affects the performance of the material. Also, to further focus the scope, the present research will deal solely with the study of a cast magnesium alloy, AM60B (elemental composition provided in Table 1.3). The focus is on castings because they can be formed into large monolithic structures, which allows fabrication of complex geometries suitable for integration into automotive structures, while also minimizing joining requirements. AM60B is produced by a super vacuum die casting process that seeks to minimize the levels of porosity by removing trapped gas cavities [5].

Element	Magnesium	Aluminum	Manganese	Trace Elements
% composition	94.0	5.5	0.2	0.3

Table 1.3 – The elemental composition of AM60B [6]

1.2 Magnesium Crystallographic Structure

For crystalline solids such as magnesium, the most common mechanism through which plastic deformation accrues is slip. Slip occurs when a body is stressed, causing dislocations to glide along specific crystallographic planes and directions (the slip system). Magnesium has a hexagonal close packed (HCP) crystal structure, with few active slip systems at room temperature (see Figure 1.1).



Type of Slip	Slip Plane	Slip Direction	Number of Slip Systems
Basal	{0001}	$\langle 11\bar{2}0 \rangle$	3
Prismatic	{10 $\bar{1}$ 0}	$\langle 11\bar{2}0 \rangle$	3
Pyramidal	{10 $\bar{1}$ 1}	$\langle 11\bar{2}0 \rangle$	6

[7,8]

Figure 1.1 – The hexagonal close packed (HCP) crystal structure of magnesium

Although there are a total of 12 independent slip systems listed in the figure above, only the basal slip systems are likely to be activated at room temperature. The prismatic and pyramidal slip systems have larger critical resolved shear stress (CRSS) levels that would need to be reached for those systems to be active. For example, in order to achieve prismatic slip at room temperature, the CRSS level required is about 100 times greater than that needed for basal slip [9,10]. It is because of this fact that magnesium at room temperature is considered to only have three operable slip systems: (0001)[11 $\bar{2}$ 0], (0001)[$\bar{1}$ 100], and (0001)[1 $\bar{1}$ 00]. In contrast, face-centred cubic (FCC) and body-centred cubic (BCC) metals offer 12 and 12-24 operable slip systems, respectively. This allows for FCC and BCC metals (e.g. aluminum and steel) to undergo extensive plastic deformation prior to fracture. This also means that HCP metals, having fewer slip systems along which dislocations may glide, are generally more brittle and

exhibit poor low temperature workability [11]. Taylor determined that five or more independent slip systems must be operable in order for a polycrystalline material to be able to work harden without causing grain boundary delamination and sudden brittle fracture [12].

Mechanical twinning is a secondary deformation mechanism that occurs in magnesium when the available slip systems are not thermodynamically predisposed to operate. This is often the case when the deformation takes place at low temperatures and/or at high rates of strain [8]. As depicted in Figure 1.2, a volume of atoms (located between two parallel twin planes that form within a single grain) change position as the matrix material on the right side of the twin deforms upwards and protrudes out from the polished surface, relieving the applied load. The open circles represent atoms that did not change position, the dashed circles represent the original location of atoms within the twin volume, and the solid circles represent the final location of atoms within the twin volume, having had to change location and orientation in order to avoid leaving a dislocation in the crystal lattice.

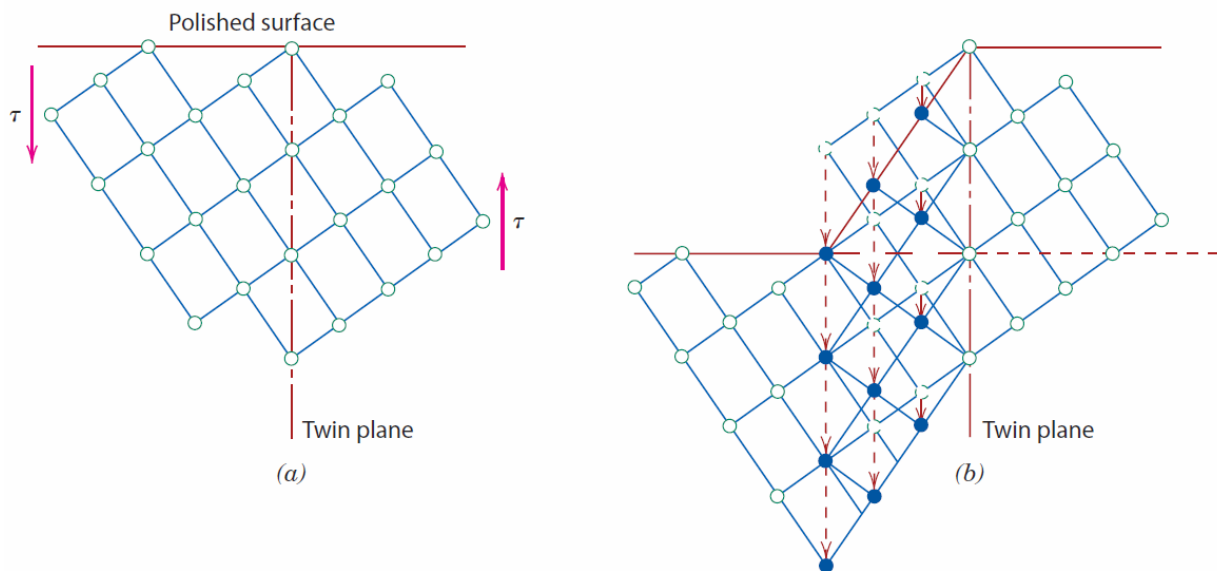


Figure 1.2 – The twinning process, a) before, and b) after (taken from [8])

This relief of applied load is very minor, but it can occur at locations all through the matrix in parallel. The macroscopic result is a significant delay in work hardening until greater strain levels are reached. In addition, small serrations in the stress signal can sometimes be detected

as twin plane sites build up stress and then subsequently twin in a matter of microseconds [13,14]. By comparison, the slip process is accomplished in a matter of milliseconds [13]. For magnesium alloys, this process most commonly occurs for the $(10\bar{1}2)[10\bar{1}1]$ tension twin [15,16,17]. The twinning process, being directional in nature, leads to tension-compression asymmetry for materials that make significant use of this deformation mechanism. For example, Figure 1.3 shows the stress-strain response that was observed during a tensile test of AZ31 magnesium. As can be seen from the “c-axis extension” stress-strain response, promptly after the elastic deformation the sample has delayed the typical work hardening phase, instead accumulating 4% strain at a consistent stress level before then initiating work hardening. This delay corresponds to the period over which deformation is accommodated by twinning within the sample.

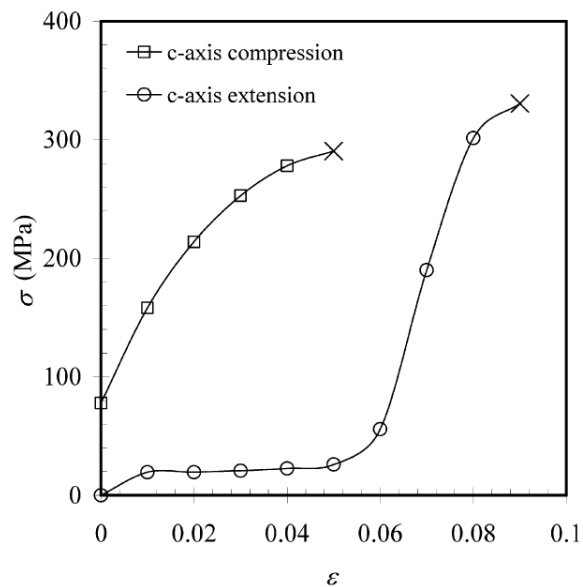


Figure 1.3 – Evidence of twinning in the tensile stress-strain response (taken from [18])

1.3 Constitutive Response of AM60B Magnesium

Several publications, e.g. [19,20] have investigated the uniaxial stress-strain response of AM60B magnesium, the alloy examined in the current research. Zeng et al. [19] found that flat uniaxial specimens extracted from AM60B extrusions subjected to a strain rate of $5.3 \times 10^{-3} \text{ s}^{-1}$ showed an ultimate tensile stress of $257 \pm 15 \text{ MPa}$ and true failure strain of 0.168 ± 0.042 . The uniaxial stress-strain response was also studied in Phase I of the Magnesium Front End

Research and Development (MFERD) project. The MFERD report [20] found that flat uniaxial specimens extracted from 2.5-3.2 mm thick AM60B cast plates subjected to a strain rate of $1 \times 10^{-3} \text{ s}^{-1}$ exhibited an ultimate tensile stress of $246 \pm 9.67 \text{ MPa}$ and elongation to failure of $12.5 \pm 1.48\%$. They also studied the strain rate sensitivity of the material, as shown in Figure 1.4 and summarized in Table 1.4.

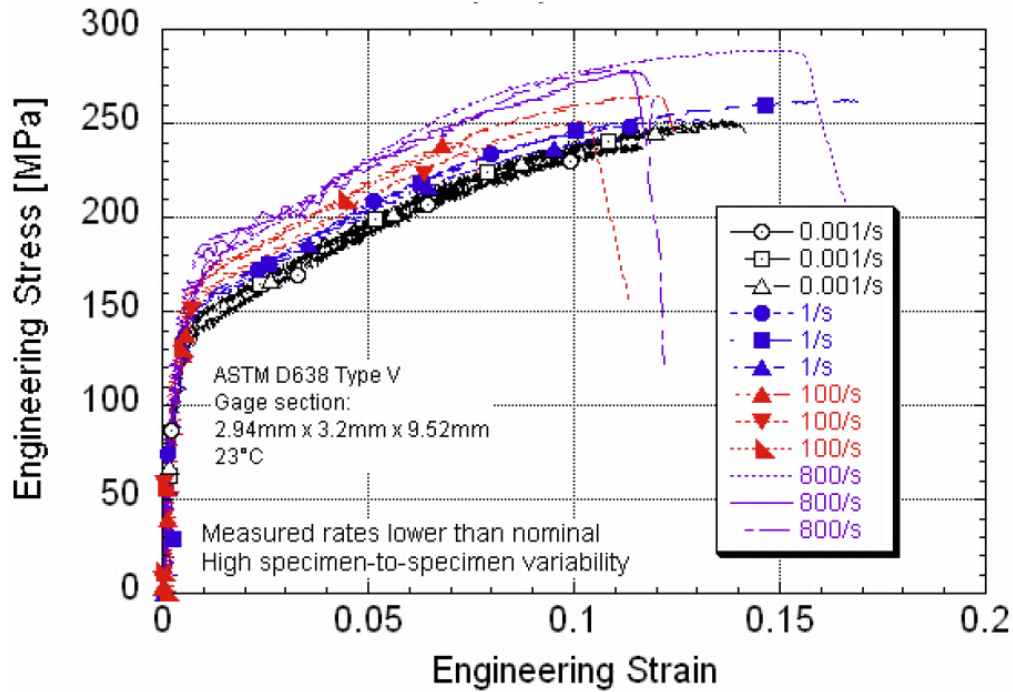


Figure 1.4 – Post-yield behaviour for AM60B across all tested strain rates (taken from [20])

Nominal Strain Rate [s^{-1}]	Engineering Yield Stress [MPa]	Engineering Ultimate Stress [MPa]	Engineering Stress at Failure [MPa]	Elongation to Failure [%]
0.001	119 ± 5.66	246 ± 9.67	246 ± 9.67	12.5 ± 1.48
1	115 ± 5.76	246 ± 13.5	245 ± 13.3	12.8 ± 3.84
100	123 ± 6.43	256 ± 10.9	256 ± 10.9	10.0 ± 1.82
800	144 ± 3.51	275 ± 12.8	274 ± 11.9	12.4 ± 2.42

Table 1.4 – Average Tensile Mechanical Properties of AM60B (adapted from [20])

The report found that AM60B displays small but positive strain rate sensitivity. However, the largest of the engineering yield and ultimate stress increases occurred within the strain rate increment of 100 to 800 s⁻¹. What makes this notable is that this is a particularly localized section of the strain rate spectrum, since 100-800 s⁻¹ encompasses less than one order of magnitude, whereas the other increments tested were two orders of magnitude apart from each other. AM60B was also seen to exhibit minimal necking and post-uniform elongation before final fracture. This behaviour is evidenced by the inclusion of the Engineering Stress at Failure column in Table 1.4; Engineering Stress at Failure was always nearly equal in magnitude to the Engineering Ultimate Stress. [20]

1.4 Characterization of Damage Processes within AM60B Magnesium

In the present work, the performance of cast AM60B components subjected to various stress states was evaluated. Stress state is often characterized in terms of stress triaxiality level, η , which is defined as:

$$\eta = \frac{\sigma_m}{\sigma_{eq}}, \quad (1)$$

where σ_m is the mean stress, and σ_{eq} is the equivalent stress.

Proceeding one step further, for a general tensorial state of stress at a point

$$\sigma = \begin{bmatrix} \sigma_{11} & \sigma_{12} & \sigma_{13} \\ \sigma_{21} & \sigma_{22} & \sigma_{23} \\ \sigma_{31} & \sigma_{32} & \sigma_{33} \end{bmatrix},$$

the mean and equivalent stresses are defined as follows:

$$\sigma_m = \frac{\sigma_{11} + \sigma_{22} + \sigma_{33}}{3} \quad (2)$$

$$\sigma_{eq} = \sqrt{\frac{1}{2} [(\sigma_{11} - \sigma_{12})^2 + (\sigma_{22} - \sigma_{33})^2 + (\sigma_{33} - \sigma_{11})^2 + 6(\sigma_{12}^2 + \sigma_{23}^2 + \sigma_{31}^2)]}. \quad (3)$$

The equivalent stress also corresponds to the von Mises stress.

It is of primary interest to characterize the failure strain as a function of stress triaxiality in the tensile domain, which is found when considering positive stress triaxiality levels. Negative

stress triaxiality levels indicate stress states in the compressive domain [21]. The inherent stress state created within the gauge area of the sample is largely dependent on the sample geometry and the direction in which the load is applied. A variety of tests exhibiting elevated stress triaxiality and corresponding strain levels reached upon failure is shown in Figure 1.5.

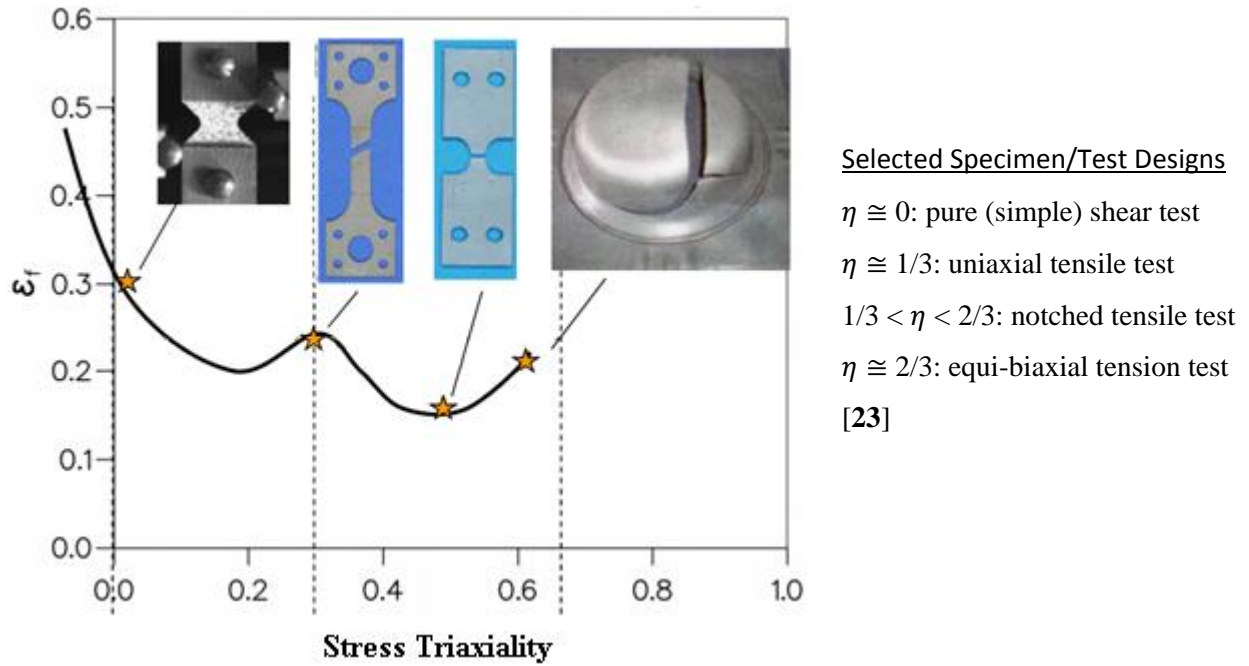


Figure 1.5 – Final strain to failure trend for specimens designed to exhibit a variety of stress triaxialities, and by extension, stress states (adapted from [22])

Many researchers have investigated the role of stress triaxiality on the performance of structural materials, e.g. [24,25,26] and found that increased stress triaxiality results in a loss of ductility (see Figure 1.6). However, these works have typically focused on more common structural materials, such as steel and aluminum.

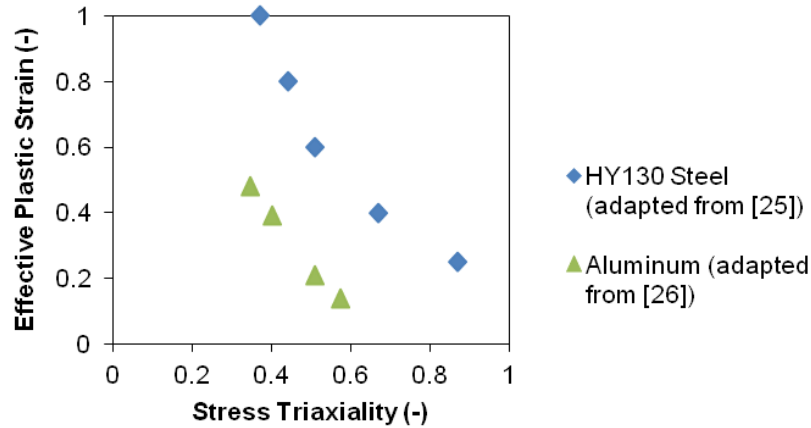


Figure 1.6 – The effective plastic strain levels reached upon failure, for a variety of stress states and materials [25] [26]

To date, there have been few studies investigating the role of stress triaxiality on the mechanical behaviour of AM60 magnesium. Yan et al. [27] found that uniaxial axisymmetric samples extracted from AM60 castings and subjected to a strain rate of $3.3 \times 10^{-4} \text{ s}^{-1}$ showed an ultimate tensile stress of $186 \pm 3 \text{ MPa}$ and elongation to failure of $8.5 \pm 0.1\%$. They also found that notched samples exhibited reduced ductility as compared to uniaxial samples. Work published by Gu et al. [28] found that flat uniaxial specimens extracted from AM60 cast plates subjected to a strain rate of $5 \times 10^{-4} \text{ s}^{-1}$ showed an ultimate tensile stress of $192 \pm 37 \text{ MPa}$ and true failure strain of 0.040 ± 0.025 . They also examined uniaxial compressive and shear stress states at the same strain rate. The uniaxial compression tests showed an ultimate compressive stress of $353 \pm 22 \text{ MPa}$ and true failure strain of 0.227 ± 0.024 . The shear tests showed an ultimate stress of $237 \pm 13 \text{ MPa}$ and true failure strain of 0.048 ± 0.012 .

The limited ductility of die cast magnesium alloys has an impact on numerical modeling. Chen et al. [29] found that numerical models would over predict the measured loading capacity if the constitutive model was based solely on uniaxial data. They recommend including damage parameters in a material model to correct this over prediction. Zhu et al. [30] evaluated several damage-focused material constitutive models to predict the performance of cast AM60B subjected to tensile, compressive, and four-point bending tests and found that a Johnson-Cook model that included the consideration of orthotropic damage was the most accurate.

For AM60, the fracture mechanism followed has been shown by Yan *et al.* [27] to depend on the severity of constraint condition, or in other words, the initial stress triaxiality level (see Figure 1.7). More particularly, while increasing the initial stress triaxiality level they found a transition point where the dominant failure mechanism changed from ductile tearing to quasi cleavage.

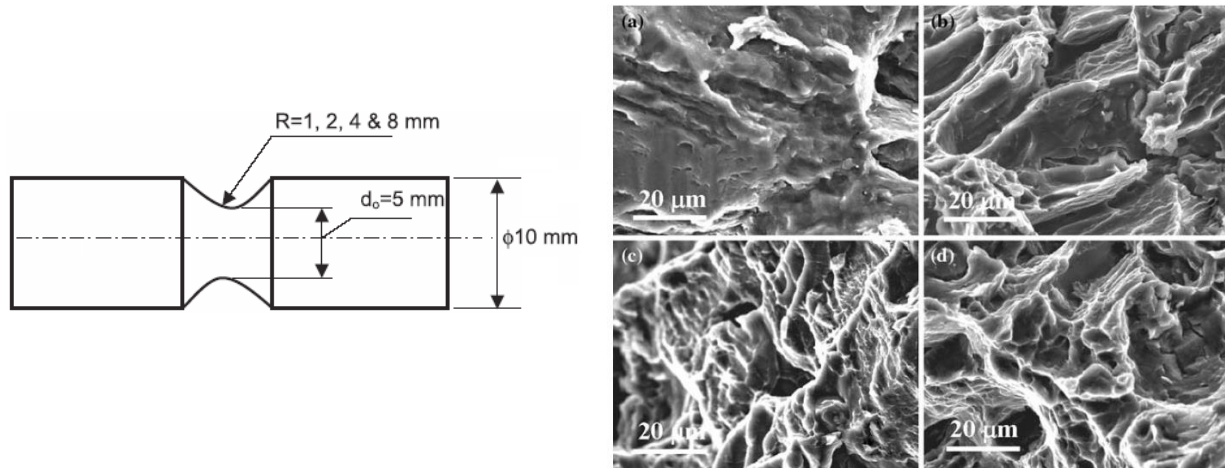


Figure 1.7 – The collection of circumferentially notched tensile tests. Left: A schematic of the sample geometries adopted. Right: The resulting representative fracture surfaces, arranged as follows: a) R = 1 mm, b) R = 2 mm, c) R = 4 mm, and d) R = 8 mm (adapted from [27])

AM60B is formed using a high pressure die casting process. In order to retain the benefits of using a cast product, as described earlier, the casting is chosen not to be followed up with a rolling or extrusion process. As a result, this introduces more issues involving microstructural nonuniformity than would be present otherwise [31,32,33,34]. As for the type of microstructural nonuniformities that are involved, a temperature gradient through the thickness of the cast part due to heat flowing out of the solidifying metal from the outer faces and into the surrounding die may be present. As seen in Figure 1.8, for example, a single axisymmetric AM60B tensile sample was cast, but a transition band corresponding to a zone enriched in 9wt% aluminum would always form [32].

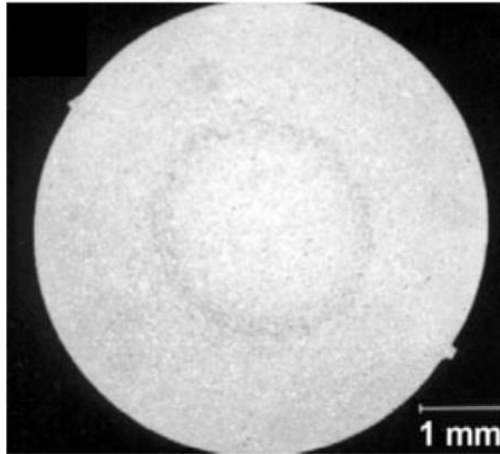


Figure 1.8 – An AM60B microstructure displaying a distinctive transition band

There may also be inclusions that were introduced into the solidifying casting. Possible origins include spallation from the ladle lining, as well as contaminants from prior uses of the mold. Another characteristic that arises as a result of employing a solely high pressure die casting process is that there is greater porosity present [33]. Porosity arises either due to solidification shrinkage or to gases being trapped during solidification [34]. Balasundaram and Gokhale [34] used digital image analysis to estimate the area fraction of porosity for a sectioned sample of AM60B, which would also represent an estimate for the bulk volumetric porosity. Using the image shown in Figure 1.9a, they estimated that the sample was 6.7% porous. In the work published by Chadha *et al.* [35], porosity was seen to accumulate in distinct bands (see Figure 1.9b). The author hypothesized that these bands tend to form if the volumetric porosity level is greater than 1.5%. Sannes *et al.* [36], having also encountered this microstructural morphology, reported that castings containing porosity segregation bands decrease the material's average elongation to failure by 45%.

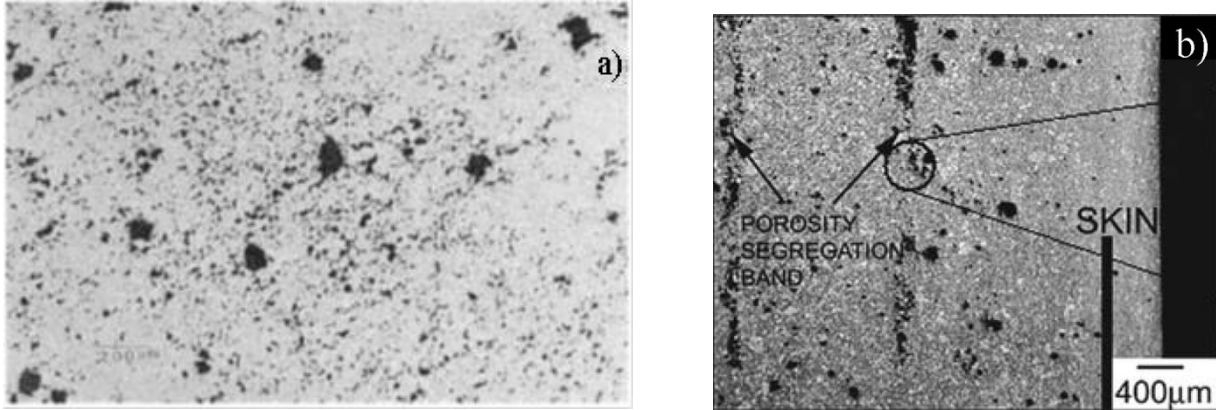


Figure 1.9 – Cross-sectional microstructures of, a) an AM60A sample, ready to be digitally analyzed in order to obtain an estimate of the volumetric porosity, b) an AM50 sample, exhibiting porosity segregation bands

Weiler *et al.* [31] also analyzed the porosity of a group of AM60 samples using x-ray tomography, a more sophisticated approach that allows the generation of a three-dimensional image representation of the sample that can then be analyzed digitally. Their five measurements for the volumetric porosity of their samples were: 0.1%, 0.2%, 0.2%, 0.7%, and 1.3%.

The greater volumetric porosity makes for significant variability in the ductility of the samples, as the voids act as incubator sites for cracks to form. This complicating factor was noted by Dorum *et al.* [37]; they decided to adopt a statistical Weibull distribution for the fracture parameter in their numerical model.

1.5 Current Research

Previous work, as cited above, has investigated the sensitivity of the stress-strain response to changes in stress triaxiality using samples extracted from flat plates; however, a review of the literature has not identified published work addressing the effect of stress triaxiality on thin-walled magnesium die cast components. To address this shortcoming in the literature, the goal of the present work is to evaluate the sensitivity of the stress-strain response and ductility of a

cast magnesium component to changes in stress triaxiality. This research considered a super vacuum die cast magnesium alloy, AM60B, used in automotive structure applications.

To examine the effect of stress triaxiality, uniaxial and notched tensile samples were considered. A near-biaxial stress state (elevated stress triaxiality) was also studied by the use of hemispherical dome tests. Experiments were performed at strain rates of 0.001 s^{-1} and 10 s^{-1} in order to examine the rate sensitivity of this alloy. Finite element models were also developed to investigate the evolution of effective plastic strain as a function of stress triaxiality at various points in the gauge region of the samples.

The balance of this thesis is organized into five chapters. Chapter 2 documents the experimental methods that were adopted, with Chapter 3 reporting the experimental results. Chapter 4 details the finite element methods that were used, with Chapter 5 reporting the finite element results. Finally, the results are discussed, conclusions are presented, and future work/recommendations are made in Chapter 6.

2 EXPERIMENTAL METHOD

The following sections outline the material used in this study, as well as the procedures adopted for the mechanical tests that were carried out and their subsequent analyses. Tensile tests were performed at two strain rates, 0.001 and 10 s^{-1} . All tests were conducted at room temperature.

2.1 Material

The component under investigation in the present work is a super vacuum die cast AM60B “top hat” geometry, as shown in Figure 2.1. Figure 2.1a) shows an isometric view of a typical component, Figure 2.1b) shows the liquid flow pattern of the super vacuum-drawn molten metal, and Figure 2.1c) shows the physical dimensions of the component. This component was also adopted in tests performed by Zhu *et al.* [30] on both the component and coupon level.

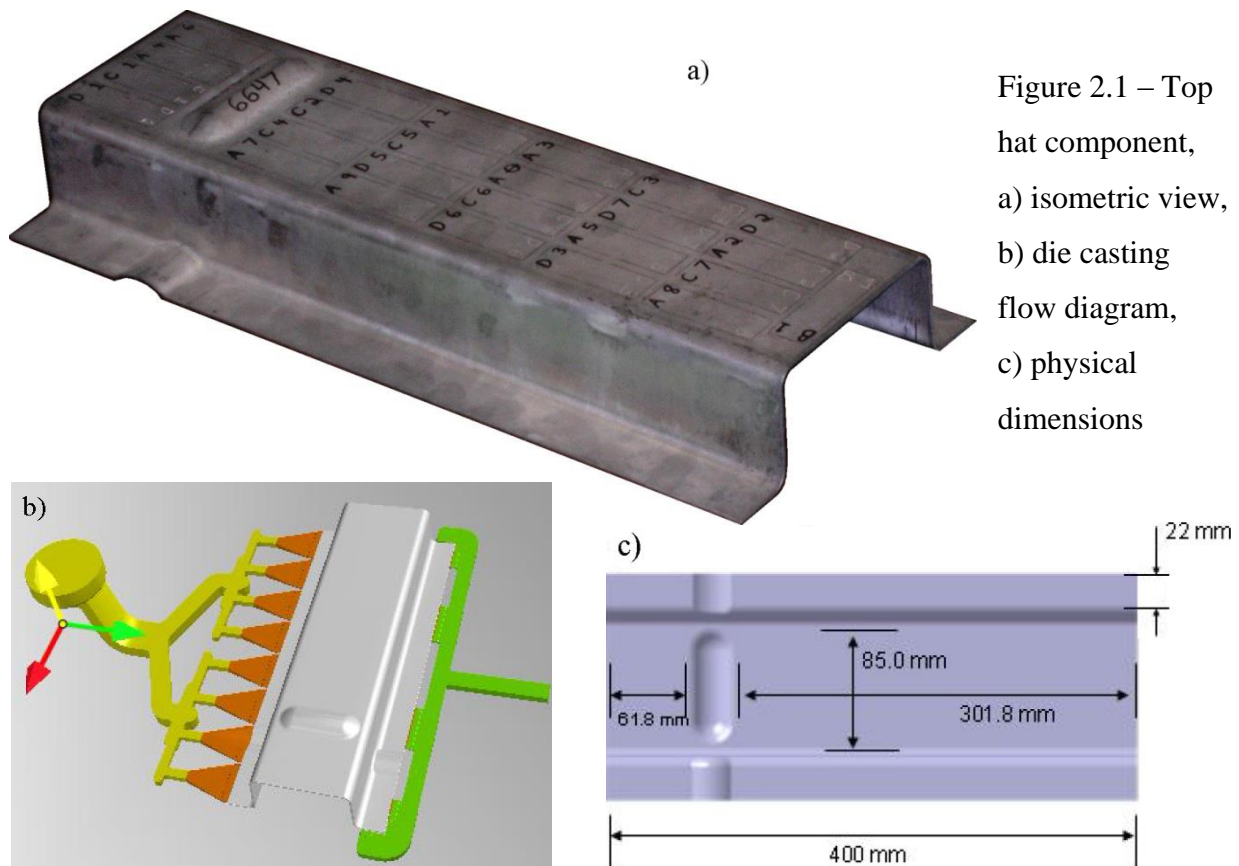


Figure 2.1 – Top hat component, a) isometric view, b) die casting flow diagram, c) physical dimensions

Two lots of castings with different thicknesses were tested over the course of the present research. The specimens tested using the uniaxial tensile test methods (both strain rates) were machined from a set of three top hats that remained at the end of Phase I of the Magnesium Front-End Research and Development (MFERD) tri-country research project. The thickness of the die and component produced at this stage was 2.0 mm. The specimens tested using hemispherical dome test methods were obtained from components that were produced in Phase II of the MFERD project, by the CanmetMATERIALS facility in Hamilton, Ontario, Canada. The die that was used in Phase II produced components with a thickness of 2.8 mm; all other physical dimensions remained the same. A set of Phase II samples was also tested using the uniaxial tensile test methods (but at a strain rate of 0.001 s^{-1} only) in order to be able to better compare the mechanical behaviour of the two batches of material.

2.2 Test Specimen Geometries

Uniaxial tensile specimens were designed in order to test the uniaxial stress state. Two orthogonal specimen orientations were considered to examine potential anisotropy within the as-cast samples. Near-biaxial conditions were also considered using hemispherical dome testing of flat sections cut from the tops of the top hat components. Finally, notched tensile specimen geometries were developed to examine stress states between uniaxial and biaxial conditions.

2.2.1 Tensile Specimens

One uniaxial and two notched tensile specimen geometries were adopted for this work. The uniaxial specimen has a gauge length of 12.5 mm and a gauge width of 3.2 mm, as shown in Figure 2.2. The gauge length for the purposes of nominal strain calculation for the two notched geometries was taken as the notch diameter. The $a/R=0.25$ specimen has a gauge length of 12.8 mm and the $a/R=1$ specimen has a gauge length of 3.2 mm. The flat miniature uniaxial tensile geometry was developed by Smerd *et al.* [38] for high strain rate testing and was shown to provide uniaxial constitutive data with a stress-strain response prior to necking that is in agreement with standard 50 mm ASTM E8 samples [39].

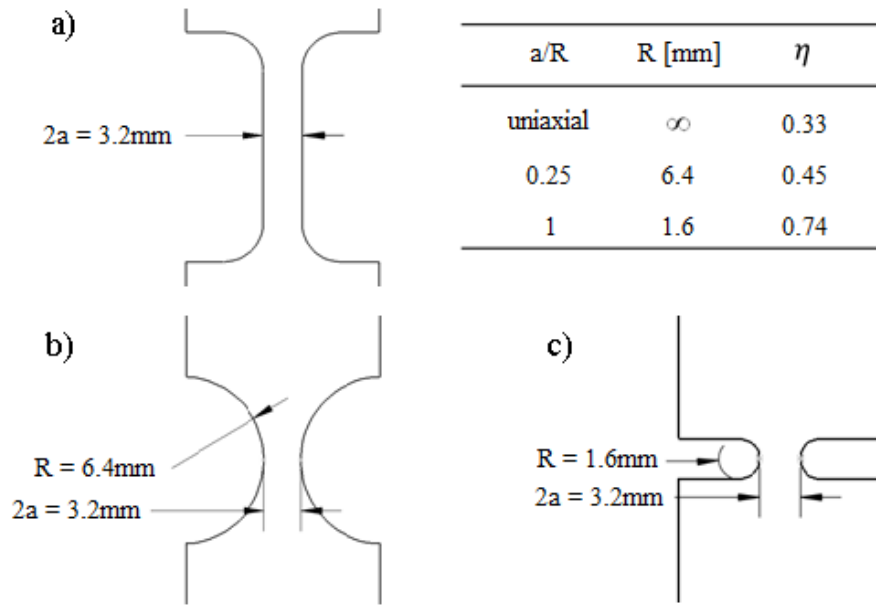


Figure 2.2 – Tensile sample geometries used, a) uniaxial, b) $a/R=0.25$, c) $a/R=1$

This miniature geometry was adopted due to space constraints on the top hat, since uniaxial specimens were tested in two orthogonal directions to evaluate the anisotropy of the casting. The two orthogonal directions are referred to as 0° and 90° , where 0° is defined as the direction that runs along the long axis of the casting (see Figure 2.3). The two notched geometries were tested in a single direction (0°).

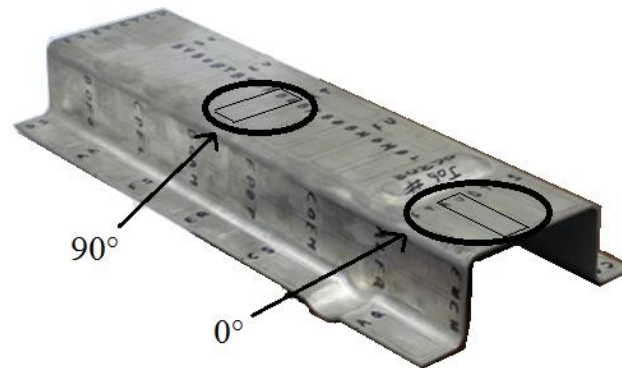


Figure 2.3 – Top hat geometry with sample orientations

The two notched tensile samples were developed based on Bridgman's [40] analysis of initial stress triaxiality at the centre of the specimen, estimated from:

$$\eta = \frac{1}{3} + \ln\left(1 + \frac{a}{2R}\right), \quad (4)$$

where a is one-half of the gauge width and R is the notch radius. It should be emphasized that this equation only estimates the initial stress triaxiality, which will fluctuate once loading commences. Finite element simulations (Chapters 4 and 5) were used to predict the operative stress triaxiality conditions for each specimen geometry. Figure 2.2 shows the sample geometries that were adopted. For simplicity, the specimens are referred to by their a/R ratio in the results, below. Specimens with notch radii of 6.4 mm and 1.6 mm were chosen. This corresponds to a/R ratios of 0.25 and 1, which provides initial stress triaxialities of 0.45 and 0.74, respectively, when using Equation (4).

2.2.2 Biaxial Specimens

A single near-biaxial hemispherical dome sample geometry was adopted for the present work. In Figure 2.4, an *in situ* view of the blank is featured. The thickness of all components used to create specimens for this test was 2.8 mm (they were cast at the CanmetMATERIALS facility in Hamilton, Ontario, Canada).

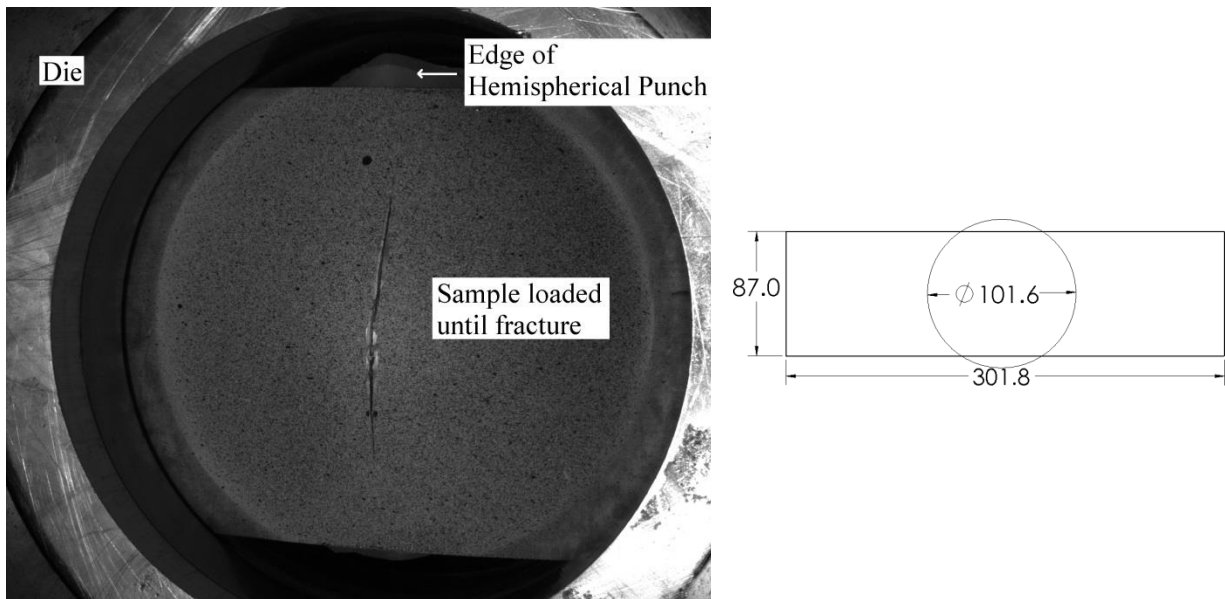


Figure 2.4 – An example of a biaxial hemispherical dome sample strained until fracture, and the blank/punch geometry [all stated dimensions in millimetres]

The width of the sample was stated as 85 mm (recall Figure 2.1), however 87 mm was found to be the maximum width able to be physically cut out of the components without introducing any visible trace of curvature to the edges of the sample due to the fillets. The major strain direction on the blank is parallel to the 0° direction used in the tensile tests; the minor strain direction on the blank is parallel to the 90° direction used in the tensile tests.

2.3 Low Rate Tensile Test Method

Tests were performed at using an Instron model 1331 servo-hydraulic load frame. A nominal strain rate of 0.001 s^{-1} was considered for the uniaxial specimens. Custom grips were employed to ensure concentricity between tests, and also to reduce specimen turnover time; two shoulder bolts were used to secure the specimen in place (see Figure 2.5). Load was measured using a 100 kN load cell. The crosshead speed v used during the tests was defined by:

$$v = \dot{\epsilon} \cdot l_o, \quad (5)$$

where $\dot{\epsilon}$ is the desired strain rate and l_o is the gauge length. Using this equation in an example, the uniaxial tensile specimen has a gauge length of 12.5 mm. Therefore, to achieve a nominal strain rate of 0.001 s^{-1} , the crosshead speed input was 0.0125 mm/s.

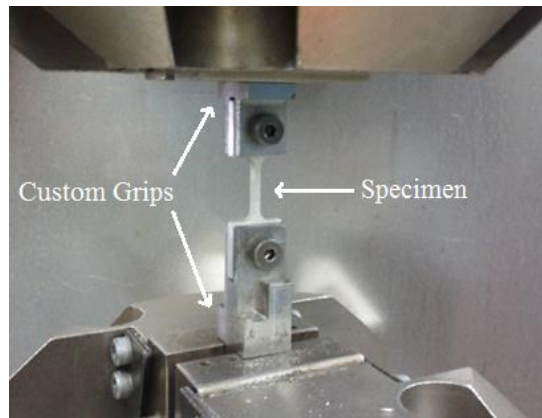


Figure 2.5 – Experimental setup for the quasi-static tests at a strain rate of 0.001 s^{-1}

The load cell analog signal is synchronized with the DIC data capture through the use of a NI USB-6221 data acquisition unit (DAQ). Therefore, for each image captured there is an associated load. The different tests were recorded at slightly different frame rates, designed so

that each test will have approximately 200-300 data points: one frame per second for the uniaxial tests, four frames per second for the $a/R=0.25$ tests, and five frames per second for the $a/R=1$ tests. *In situ* two-dimensional DIC analysis was used for all tests to determine the elongation and surface strains of the specimens. To prepare a speckled surface (which is necessary for DIC analysis), the samples were lightly sandblasted (yielding a silvery-white finish), and then using an aspirator to thin out the spray paint particulates, subsequently speckled with black spray-paint. Sandblasting was chosen in favour of a white base coat of paint as poor adhesion was observed between the base coat and metallic surface resulting in flaking and incorrect DIC measurements [41]. Twin light stands were employed to provide sufficient contrast to the speckle pattern seen by the camera. Images were acquired using a 5.0 megapixel Point Grey Research Grasshopper camera (GRAS-50S5M-C) and Nikon 60 mm lens at frame rates of 1-5 frames per second. The setup of the camera and the lighting is shown in Figure 2.6.

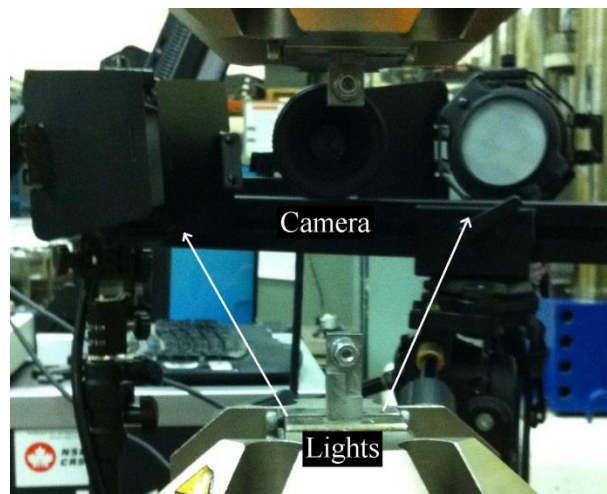


Figure 2.6 – Lights and camera setup for the quasi-static tests at a strain rate of 0.001 s^{-1}

Strain was calculated through the use of a “virtual” extensometer overlaid on the images using the DIC analysis software Vic-2D 2009 [42]. The uniaxial tensile tests were conducted according to ASTM B557 [43] and used a gauge length of 12.5 mm. The notched tensile tests, being of non-standard geometry, yielded what will be referred to as “nominal” strains. These tests used gauge lengths that correspond to their notch diameters (12.8 mm and 3.2 mm for the $a/R=0.25$ and $a/R=1$ sample geometries, respectively). As the deformation proceeds, the virtual extensometer extends as well, so it is possible to calculate an engineering/nominal strain using

$$\varepsilon = \frac{l_1 - l_0}{l_0}, \quad (6)$$

where l_1 is the current gauge length, and l_0 is the original gauge length. Engineering stress, σ_e , can then be calculated using

$$\sigma_e = \frac{F}{A_0}, \quad (7)$$

where A_0 is the original cross-sectional area. The initial thicknesses and widths making up the cross-sectional area were measured using a micrometer or shadowgraph. A shadowgraph was used to obtain an accurate measure of the gauge width for the notched sample geometries, since the notch root is not sufficiently flat for micrometer use.

For the uniaxial tension tests, to convert engineering stress and strain into true stress and strain, the following set of equations is used:

$$\varepsilon_t = \ln(1 + \varepsilon), \quad (8)$$

$$\sigma_t = \sigma_e e^{\varepsilon_t}. \quad (9)$$

These equations were derived under the assumption that volume is conserved, so they are consequently only valid up until the onset of necking. True stress-strain curves are typically required as constitutive input data for non-linear finite element simulations. More specifically, almost all metal plasticity models require an effective plastic strain ($\overline{\varepsilon^p}$) versus true stress curve. In order to convert true strain into $\overline{\varepsilon^p}$, the elastic strain portion,

$$\varepsilon_E = \frac{\sigma_t}{E} \quad (10)$$

must be subtracted from the current strain level

$$\overline{\varepsilon^p} = \varepsilon_t - \varepsilon_E \quad (11)$$

$$\overline{\varepsilon^p} = \varepsilon_t - \frac{\sigma_t}{E}, \quad (12)$$

where the true stress and elastic strain levels reached for the current true strain level are σ_t and ε_E , respectively. Young's modulus, E , is a wholly material dependent parameter, and it would typically be constant for all applied strain levels. However, in practice, the elastic stress-strain response for AM60B was slightly nonlinear up until the point where it began to plastically flow (see Figure 2.7 for an example of an engineering stress-strain response that was observed).

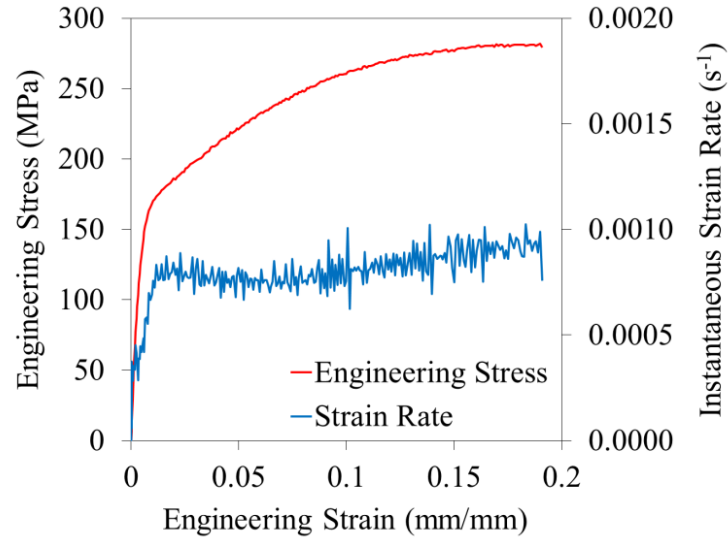


Figure 2.7 – A typical 0.001 s^{-1} test, showing engineering stress, strain, and instantaneous strain rate responses

Due to this slight nonlinearity, in order to be able to subtract a more appropriate amount of strain when calculating $\bar{\varepsilon}^p$, a standard of calculating an “apparent Young’s modulus,” similar to the one used by Bardelcik *et al.* [44], was adopted. The apparent Young’s modulus was taken to be the average of all Young’s moduli increments, $\sigma_{e_i}/\varepsilon_{e_i}$, occurring between engineering stress levels of 30 and 150 MPa. In practice, the apparent Young’s modulus ranged from 23 to 32 GPa, which is lower than the generally accepted Young’s modulus of AM60B, 43 GPa [45].

The strain rate experienced over the course of a test is not constant; there is a ramp-up period at the beginning (see Figure 2.7). This happens to coincide with the elastic deformation, and after which the strain rate is relatively steady shortly after entering the plastic region. The approach adopted herein for reporting the strain rate for a given test was to average all instantaneous strain rate readings recorded past a nominal strain of 2.0%.

For the purposes of estimating the material’s degree of anisotropy (or lack thereof), the r-value was also measured. The r-value, also known as the Lankford coefficient, is defined as the ratio of the level of plastic flow in the width direction to the level of plastic flow in the thickness

direction: $r = \varepsilon_w/\varepsilon_t$. Width, ε_w , and longitudinal, ε_l , strains were obtained from DIC measurements of uniaxial sample tests while the thickness strain ε_t was calculated based on the assumption of incompressible deformation: $\varepsilon_l + \varepsilon_w + \varepsilon_t = 0$. The gauge width used in obtaining ε_w varied between 2.3 and 3.2 mm for all tests conducted. This considerable range was the case for the following two reasons:

- When defining the area of interest it was sometimes difficult to obtain a tight fit to the physical boundaries of the specimen while not introducing edge effects into the resulting contour plots.
- As the gauge width was measured at the location where the failure will occur, large increments in strains experienced just prior to failure occasionally caused the virtual extensometer to lose track of the correct pixel it was meant to be affixed to. Therefore, a measure of the gauge width all the way until failure was not obtainable unless the gauge width was reduced somewhat.

If the r-value is non-unity, then it can be said that the material exhibits anisotropic behaviour. Furthermore, if $0 < r < 1$, then material is drawn in through the thickness direction more readily than it is through the width direction; if $1 < r < \infty$, then material is drawn in through the width direction more readily than it is through the thickness direction.

2.4 High Rate Tensile Test Method

Elevated strain rate experiments (10 s^{-1}) were performed using a custom Hydraulic Intermediate Strain Rate (HISR) apparatus that was developed at the University of Waterloo (see Figure 2.8 for the experimental setup). To achieve a strain rate of 10 s^{-1} , the crosshead speed was 125 mm/s (refer to equation 5). The specimen load was measured by a KISTLER 9341B load cell (with the signal amplified by a KISTLER Type 5010 dual mode amplifier), and the specimen elongation was measured by DIC, in a similar fashion as used for the 0.001 s^{-1} strain rate tests (discussed in the previous section). The main difference concerning the 10 s^{-1} strain rate experimental method is that a high speed HSI FASTCAM SA5 Photron (1300K-M1) camera capturing images at 7000 frames per second was used. The specimens were prepared as outlined in Section 2.3.



Figure 2.8 – Experimental setup for the tests at a strain rate of 10 s^{-1}

Considering the strain history this apparatus is capable of producing, Figure 2.9 shows the engineering stress-strain response along with the strain history of a typical test. As also seen with the 0.001 s^{-1} test apparatus, the strain rate requires a significant proportion of the total test's duration to ramp up to a relatively steady state. This duration however approximately coincides with the elastic region, which will be removed from any subsequent constitutive fitting efforts.

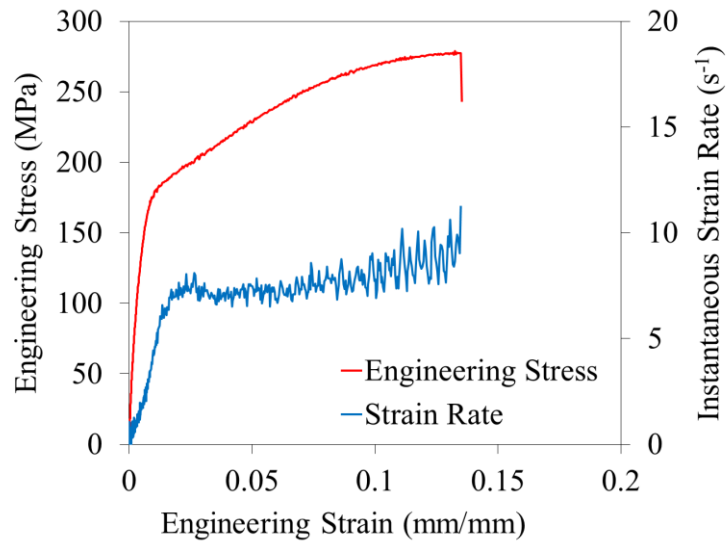


Figure 2.9 – A typical 10 s^{-1} test, showing engineering stress, strain, and strain rate responses

The apparent Young's modulus for the 10 s^{-1} tests was found to range from 30 to 37 GPa, which is similar to the generally accepted Young's modulus of AM60B, 43 GPa [45].

2.5 Biaxial Hemispherical Dome Test Method

Hemispherical dome experiments were also performed to characterize the failure strain under near-biaxial conditions. The apparatus, as shown in Figure 2.10, was an MTS Systems Corporation load unit (model number 866.02) that could support a punch four inches in diameter.

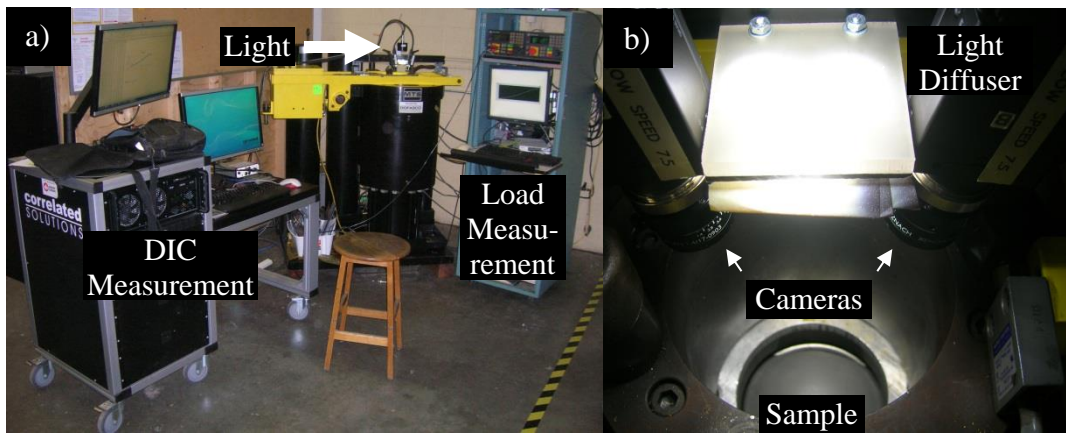


Figure 2.10 – Experimental setup for the biaxial hemispherical dome tests, a) an overall view of the various systems involved, b) a close-up view of the lights and camera arrangement

Lock beads are sometimes used in the die/binder combination in order to prevent the uneven drawing of material up onto the punch [46]. However, due to the inherent brittleness of AM60B, this was not possible to do without causing the specimen to fracture at the lock bead corners. As a compromise, a large binder force (900 kN) was imparted onto the blank and die. Also, the DIC images and simulation were scrutinized for evidence of the blank being drawn up onto the punch; it was deemed to be minimal, at less than 1 mm of draw. The stress state achieved is nominally a biaxial one (see Figure 2.11), however because the specimen geometry used does not span the full die-punch-die gap in one dimension, the lack of a binding force applied in this dimension makes for a slightly uneven application of principal stresses, i.e.

$$\sigma_1 > \sigma_2 > 0. \quad (13)$$

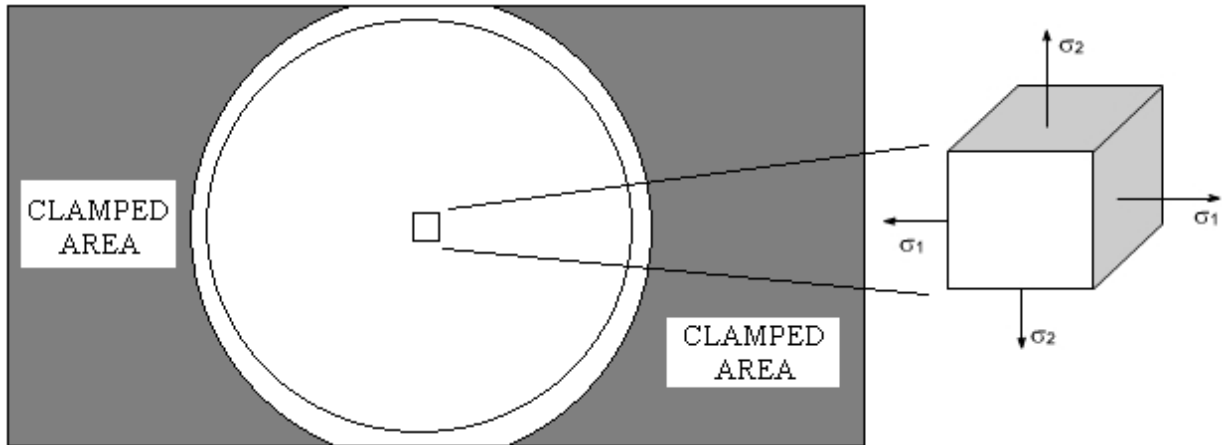


Figure 2.11 – Schematic illustrating the stress state achieved in the hemispherical dome tests

As for pre-test preparation, the speckling procedure followed included spraying a thin white primer base coat, and then allowing a minute for it to partially dry. Then, using an aspirator to thin out the spray paint particulates, spray a black speckle pattern down onto the upward facing blank resting on a flat surface. The preparation of the apparatus included the addition of a lubricant between the punch and the blank. A combination of two circular PTFE sheets with an intermediate layer of petroleum jelly was found to be adequate. It should be noted that this procedure differs from that used in preparation of the tensile samples; a white coat of paint was used instead of the sandblasting procedure. The default decision would have been to continue using the sandblasting procedure, and this was in fact specifically adopted in the testing procedure for ZEK100 biaxial specimens [41]. However, the concern that motivated this break from consistency arose from the fact that there is a small amount of material removed when sandblasting was used on the tensile samples. It also removes it in a slightly non-uniform way, leaving peaks and valleys as the surface texture; this could increase the chance that one of these valleys develops into a premature crack initiation site, as on the side away from the punch is a stress state of biaxial tension (see Section 3.10 for a more detailed discussion). The only drawback to using a base coat of white paint instead of sandblasting was that the sample had to also be tested on the day it was painted. Cracking of the white paint prior to sample failure was observed in prior tests that were done a few days after the initial painting.

A set of LED lights was suspended over the top of the apparatus, to illuminate the cavity and speckle pattern that would protrude upwards upon the initiation of the test. A pair of 5.0 megapixel Point Grey Research Grasshopper cameras (GRAS-50S5M-C) was also suspended at this bird's eye location. 3D DIC was necessary in order to capture the motion occurring in all three dimensions. The samples were placed on the die, ensuring for centre by visual alignment with the four corners of the die. The binder was then brought down and clamped the blank against the die. In concert with the punch actuation, the twin cameras began recording images at a rate of four frames per second. The punch moved at a speed of 0.25 mm/s, which was chosen after the results of test runs showed that the sample could be displaced by roughly 25 mm before fracture, and so 0.25 mm/s would allow for a similar number of time steps as had been used in the tensile tests. The test was halted upon fracture of the sample. In post-processing, major and minor strains were obtained using a point overlaid on the images in the location of maximum strain that is present along the crack formed upon failure; this was accomplished using the DIC analysis software Vic-3D. The use of a minimal diameter circle was compared, which would be more reliable in avoiding any signal noise that may happen to be present at an instantaneous point. However, the point method was favoured as it could be guaranteed that there would be no influence of small gradients surrounding the location of maximum strain and the signal noise concern was never found to be present in this dataset.

As a separate but related note, midway through the set of hemispherical dome experiments, the test apparatus had to be relocated to another laboratory. In the new location, the hydraulic circuit was different, so everything had to be recalibrated. The load cell was also replaced, which necessitated another calibration. These extenuating factors unfortunately had a negative impact on the quality of the resulting data, as described in the presentation of the experimental results.

2.6 Digital Image Correlation

Digital Image Correlation (DIC) is an experimental technique used to track subtle changes in digital images in order to be able to quantify the displacements that occur on the surface of a

sample when it is tested. For the purposes of this work, it was used to measure surface strain histories on two-dimensional and three-dimensional surfaces of samples. For brevity, only the two-dimensional method will be described here. The two-dimensional strain measurements were accomplished by first creating a speckled surface using white and black paint on the specimen to be tested, similar to the example shown in Figure 2.12.

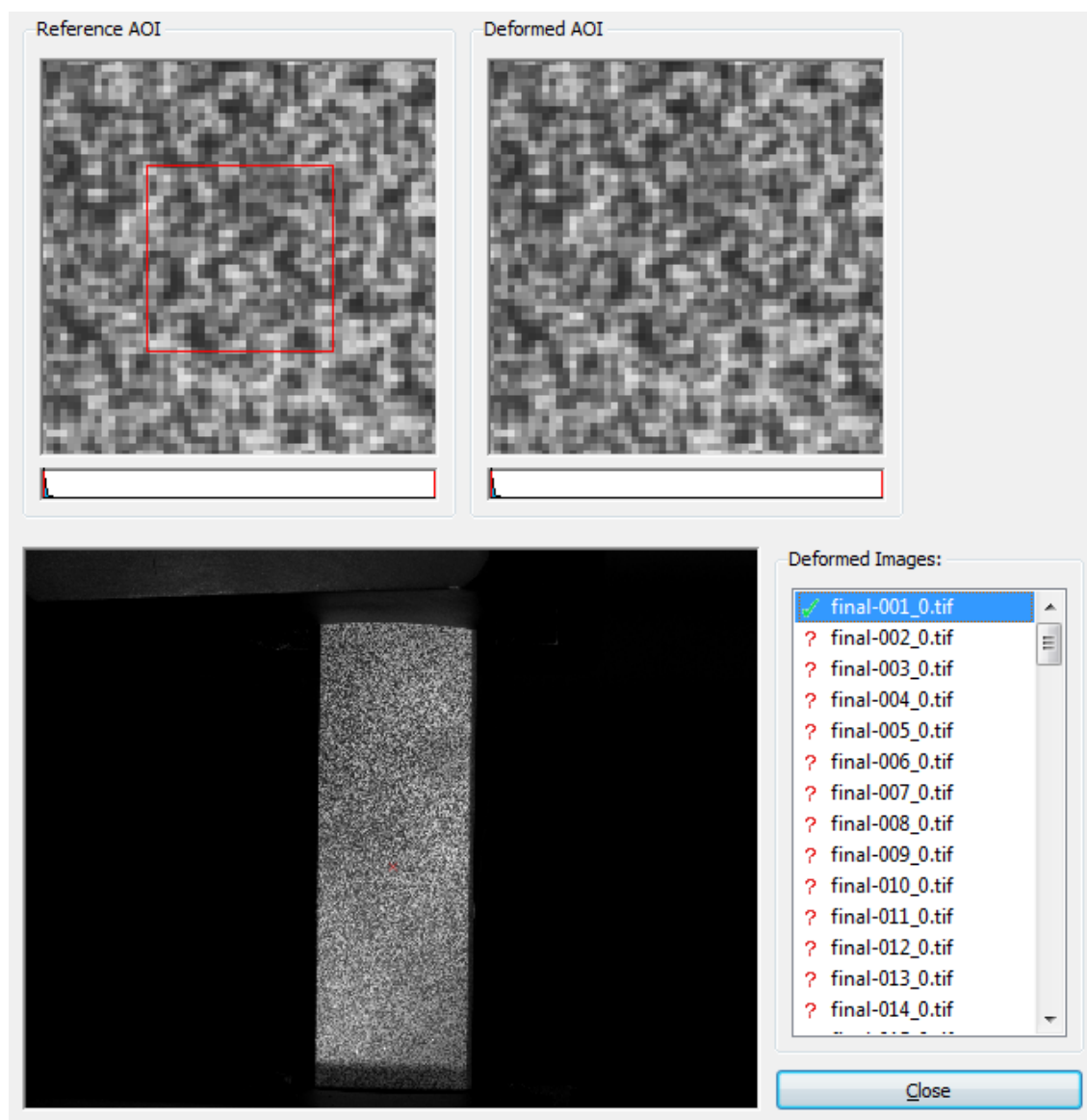


Figure 2.12 – A typical speckle pattern, including digitally zoomed-in comparisons of the undeformed reference area of interest (AOI) to the deformed AOI. Subtle variations in pixel greyscale levels can be seen and are picked up by the image analysis software.

Highly contrasting neighbouring speckles become highly contrasting neighbouring pixels in the image analysis software used in this work, VIC-2D and VIC-3D [42]. These pixels are then easier to track using a search algorithm [47] that compares the undeformed image to an image taken at any given point in the deformation process. This search algorithm tests a proposed displacement vector (u, v) of a single pixel by calculating the value of a mutual cross coefficient, $r(i, j)$:

$$r(i, j) = 1 - \frac{\sum A(i, j)B(i^*, j^*)}{(\sum A(i, j)^2 * \sum B(i^*, j^*)^2)^{1/2}}, \quad (14)$$

where $A(i, j)$ is the greyscale level for the pixel located at (i, j) in the undeformed image and $B(i^*, j^*)$ is the greyscale level for the pixel located at (i^*, j^*) in the deformed image.

If the value for $r(i, j)$ is less than it was for the previously proposed displacement vector (u, v) and it no longer continues to decrease when proceeding one additional cycle in the recursion, then the true displacement vector has been found:

$$\begin{pmatrix} u \\ v \end{pmatrix} = \begin{pmatrix} i^* - i \\ j^* - j \end{pmatrix}. \quad (15)$$

This can then be followed up by determining absolute pixel positions/displacements, as well as pixel-to-pixel strains. An example showing how the search algorithm was able to determine how the original image was deformed is shown in Figure 2.13, denoted by the dashed red polygon.

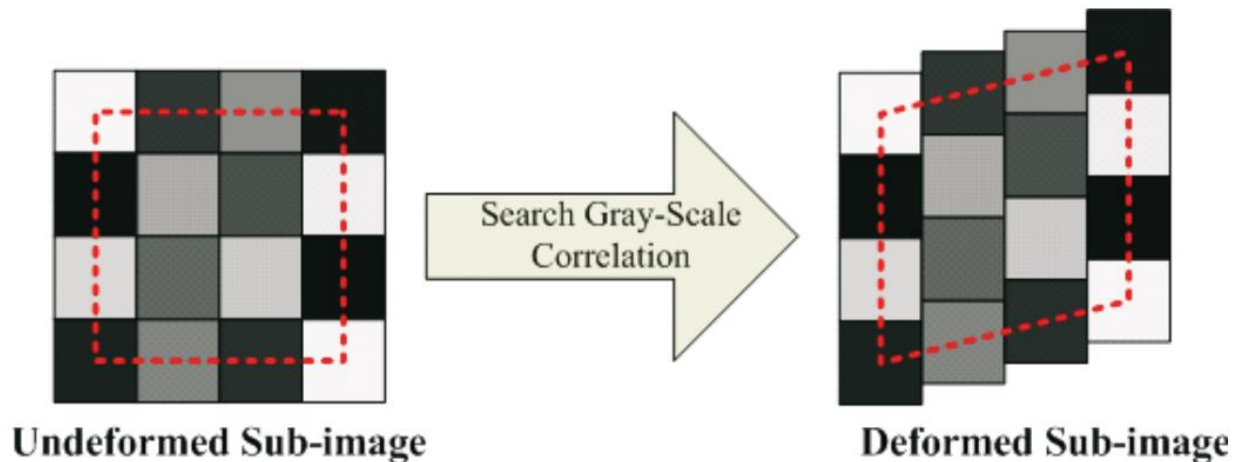


Figure 2.13 – Greyscale correlation between undeformed and deformed sub-images (taken from [48])

Using DIC eliminates the need for bulky extensometers, and it also is able to provide full two-dimensional measured strain fields rather than just strain measurements at discrete locations, as in the case of using extensometers or strain gauges, for example.

For the present work, two test parameters that had to be defined were the subset and step size. The subset parameter controls the size of sub-image that is observed for any displacements occurring as time proceeds. It must be large enough so that there is a distinct pattern contained in the sub-image. The step size parameter defines the spacing between a pair of pixels being analyzed during correlation. It should be small enough to discern subtle differences, but it should be large enough to avoid excessive computational demands [42]. For the 5.0 megapixel images of tests performed at a strain rate of 0.001 s^{-1} , the most optimal subset/step combination that was found was a subset size of 75 and a step size of 11. For the 0.4 megapixel images of tests performed at a strain rate of 10 s^{-1} , the most optimal subset/step combination that was found was a subset size of 21 and a step size of 5. The preceding two optimizations were done by determining the smallest subset and largest step size that would allow the evolving contour plot to be able to obtain a solution for displacements at all points within the AOI, and at all points in time during the deformation process up until failure. It should also be noted that 0.4 megapixels was the maximum resolution obtainable by the high speed camera when capturing 7000 frames per second. Finally, regarding the type of post-processing selected, Hencky principal strain tensors were sought for all tests.

2.7 Test Matrix

The two main parameters of the present work are the sample geometry and the strain rate during the tensile tests. A test matrix including the number of repeat tests that were performed is shown in Table 2.1. The crosshead speed used in all the tests is listed in lieu of the strain rate (recall that for the tensile tests, 0.0125 mm/s corresponds to a strain rate of 0.001 s^{-1} , and 125 mm/s corresponds to a strain rate of 10 s^{-1}). It was chosen to be presented in this way so that the punch speed used in the hemispherical dome tests can also be listed, for comparison purposes.

Crosshead/Punch speed [mm/s]	Sample Thickness [mm]	0° uniaxial	90° uniaxial	a/R=0.25	a/R=1	Hemidome tests
0.0125	2.0; Phase I	16	6	18	16	-
0.0125	2.8; Phase II	6	5	5	6	-
125	2.0; Phase I	4	3	4	4	-
0.25	2.8; Phase II	-	-	-	-	11

Table 2.1 – Test matrix for the main parameters that were tested

A more detailed test matrix including selected characteristics of each sample can be found in Appendix A.

3 EXPERIMENTAL RESULTS

In this chapter, experimental findings from tensile and biaxial hemispherical dome tests are presented. Of particular interest is the effect of stress triaxiality on the strain to failure in this cast material. Also included are investigations into the effects of strain rate and sample location on the mechanical response of the cast component. An examination into whether or not AM60B exhibits an isotropic stress-strain response is also pursued. Finally, follow-up statistical analyses and metallographic investigations are also presented.

3.1 Quantifying the Error Due to the Casting Process

Statistical variance in castings (due to porosity, inclusions, etc.) complicates our understanding of the mechanical performance of cast metals. It is therefore imperative to characterize how much variance is present. Figure 3.1 shows nine repeat tests of the measured engineering stress-strain response for the uniaxial geometry in the 0° orientation. The symbols shown in the figure indicate the median curve of the data. The nine samples were taken from the top of a single top hat component; therefore, any inherent part-to-part variation would not factor into this scatter plot.

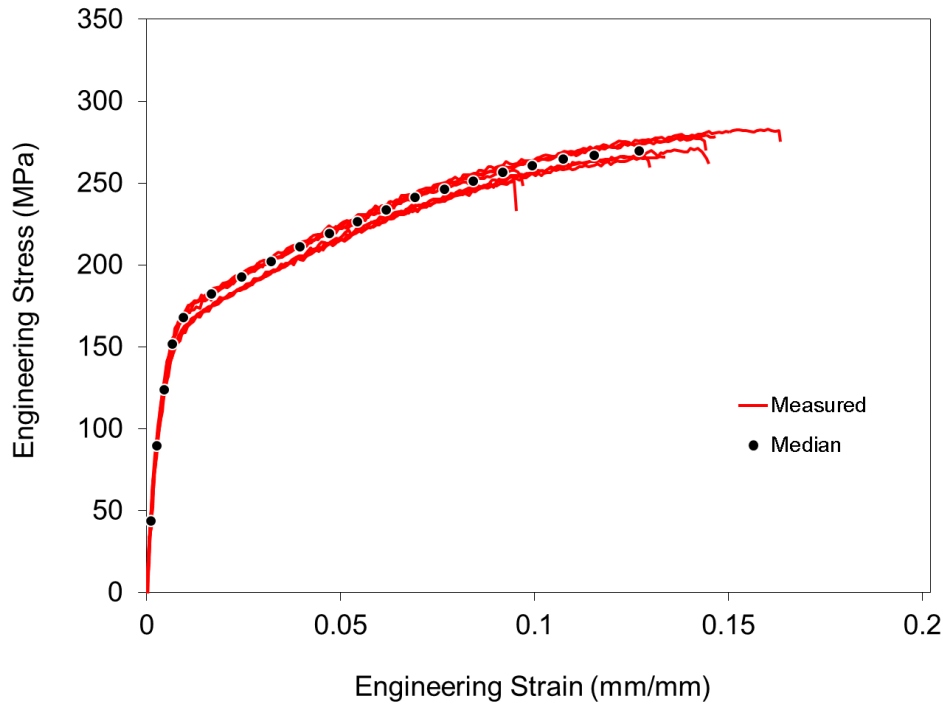


Figure 3.1 – Measured 0° uniaxial tensile test engineering stress-strain results

The measured data shows variability in both stress for a given strain and elongation to failure; however, the hardening trends appear similar. At an engineering strain of 8%, the variability of the measured stress-strain response ranged from 243 to 252 MPa, and exhibited a standard deviation of 3.7 MPa. The variation in the elongation to failure ranged from 9.6% to 19.1% and exhibited a standard deviation of 2.8% strain. This variation in both measured stress-strain response and elongation to failure was also observed by Weiler et al. [31], and may be due to the brittle cleavage-based failure mechanisms measured in die cast magnesium alloys [49]. The variability of the measured stress-strain response was similar for data collected for the two notched geometries. For the $a/R=0.25$ findings elongation to failure ranged from 3.6% to 5.5% strain and exhibited a standard deviation of 0.6% strain. For the $a/R=1$ findings, elongation to failure ranged from 5.7% to 9.4% strain and exhibited a standard deviation of 1.2% strain. For the remainder of the data reported in this paper, unless otherwise noted, only the median stress-strain response of six or more repeat tests will be shown to improve figure clarity. The median curve is the one that exhibited a median stress level at a set strain level. This curve does not necessarily also represent the median final elongation to failure; this will be addressed in a separate failure analysis in the proceeding section.

3.2 Tensile Test Results

Ninety-three tensile tests (the total number of uniaxial and notched samples tested) were carried out, with each one yielding two sets of data: the load signal and the strain evolution. The strain evolution was the more complicated dataset to process, as it came in the form of a set of images and required DIC analysis in order to be able to extract the nominal strain. Figure 3.2 shows a contour plot derived from the DIC image acquired during one of the tests. A virtual extensometer would have been overlaid onto the initial undeformed image in this series; this is how the evolving nominal strain was obtained.

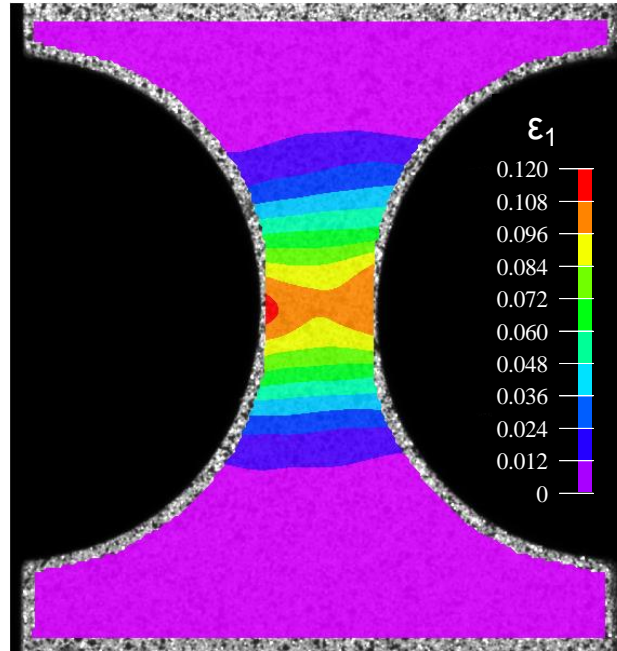


Figure 3.2 – An example Hencky first principal strain contour plot for an $a/R=0.25$ sample, at a nominal strain of 4.0%

Figure 3.3 shows the median engineering stress-nominal strain curves of the uniaxial and notched sample geometries to demonstrate the effects that stress state, orientation, and sample origin have on the stress-strain response of the material. “Sample origin” refers to whether the sample was taken from a 2.0 mm thick component cast during Phase I or a 2.8 mm thick component from Phase II of the MFERD project. Note that part-to-part variation was not considered in the analysis of the data. As there was an insufficient number of samples left over from Phase I of the project, it was necessary to introduce this additional sample origin parameter, in order to be able to perform a wider variety of tests. Most notably, the biaxial hemispherical dome tests would not have been possible if the project was restricted to solely using Phase I material.

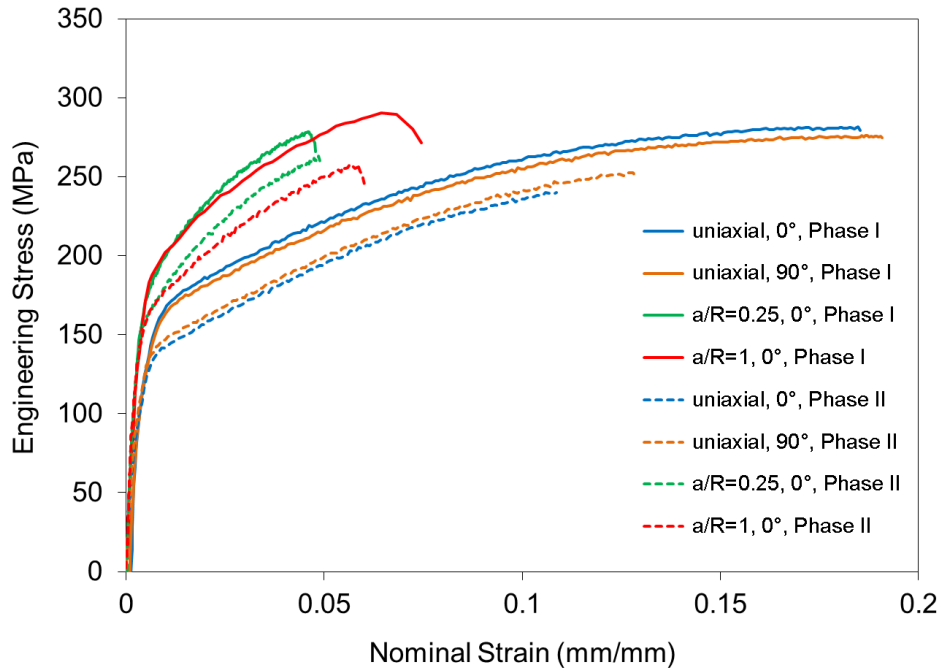


Figure 3.3 – Median engineering stress-nominal strain curves for all stress states, orientations, and material origins under study

These results show that elongation to failure is decreased and the maximum stress is increased as stress triaxiality (notch severity) is increased. This maximum stress effect was also observed by Yan et al. [27]. Regarding Phase I vs. Phase II trends, it is clear that the Phase II casting exhibits lower overall stress and elongation to failure.

Figure 3.3 serves to demonstrate the constitutive response of the actual median (in terms of stress) test specimen for each set of parameter combinations. It would now be helpful to document what levels of variability were observed. Figure 3.4 and Figure 3.5 plot the same eight test parameter combinations as before, but they do so for specific quantities, so that a mean and standard deviation may also be provided. Figure 3.4 plots the engineering stress reached after 2% of nominal strain has been accumulated and Figure 3.5 plots the elongation to failure attained.

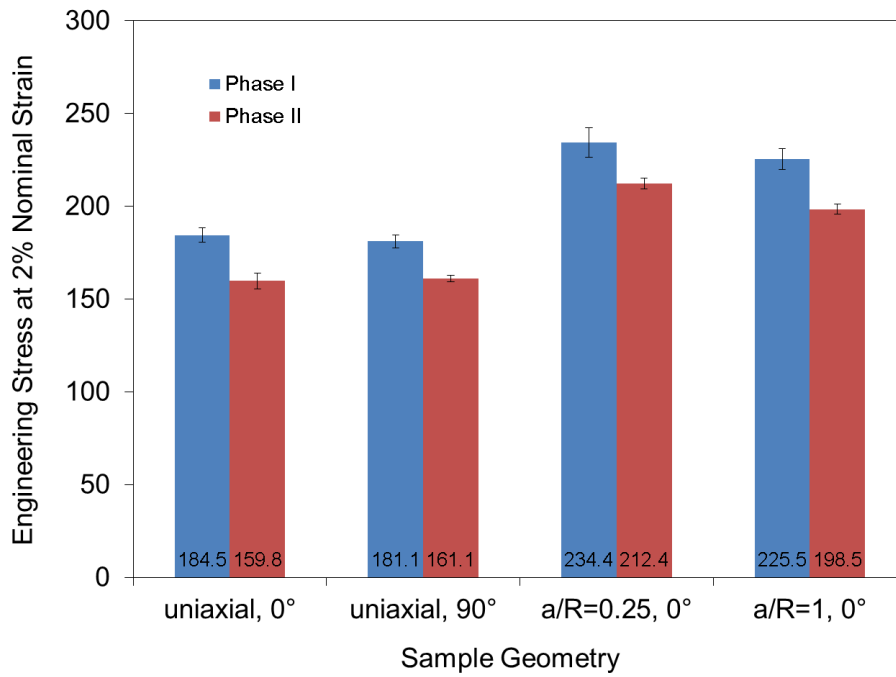


Figure 3.4 – Strength dependence on stress state and sample origin (sample means noted at the base of each column)

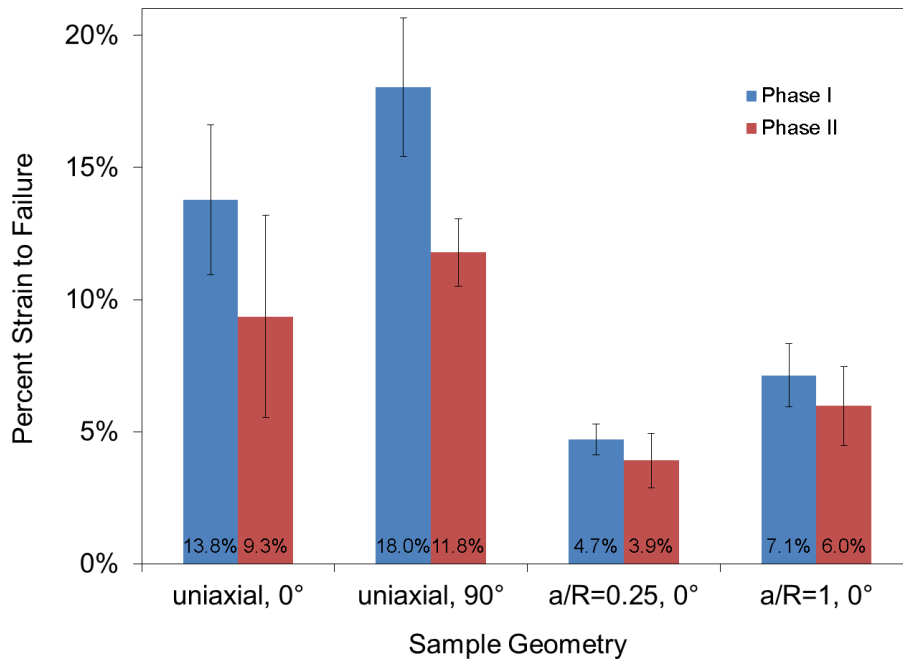


Figure 3.5 – Elongation to failure dependence on stress state and sample origin (sample means noted at the base of each column)

The stress levels of Figure 3.4 naturally exhibit the same trends as observed in Figure 3.3, as well as the fact that there is relatively little scatter, so the focus will be on the ductility trends observed. Referring to Figure 3.5, the ductility decreases greatly when moving from the uniaxial to notched sample geometry. Regarding the different sample origins, it is again apparent that the Phase II material displays inferior ductility and strength. It will be necessary to investigate possible reasons for this considerable disparity; metallographic analyses are performed and documented in section 3.9.

It should be documented that there was an inconsistency adopted throughout this project. When it was discovered, it was not corrected in order to be able to have a larger dataset with fewer parameters involved. The crosshead velocity used for all tests was 0.0125 mm/s and 125 mm/s, even for the notched sample geometries. Given that the a/R=1 sample geometry has a gauge length of 3.2 mm, 0.0032 mm/s and 32 mm/s should have also been the crosshead velocities used. For a/R=0.25, there was just a minor inconsistency, using crosshead velocities of 0.0125 mm/s and 125 mm/s instead of the correct velocities of 0.0128 mm/s and 128 mm/s. To be more accurate, therefore, the actual nominal strain rates that were imparted upon the tensile samples are listed in Table 3.1.

Sample Geometry	Intended nominal strain rate [s^{-1}]		Actual nominal strain rate [s^{-1}]	
	Low Strain Rate	High Strain Rate	Low Strain Rate	High Strain Rate
Uniaxial	0.001	10	0.00077	7.2
a/R=0.25	0.001	10	0.00083	7.6
a/R=1	0.001	10	0.00196	14

Table 3.1 – The actual nominal strain rates imparted upon the three different tensile sample geometries

This turns out to have a minimal impact in the comparisons between 0.001 and 10 s^{-1} data. It would mainly have manifested as a slight maximum stress exaggeration (due to the consistently positive strain rate sensitivity) when comparing the tensile stress states. For

example, the true median $a/R=1$ stress-strain curves at 0.001 and 10 s^{-1} would likely not have had as large of a maximum stress as was reported.

There are some trends in the tensile test results that are very clearly real (for example in Figure 3.5, how the notched geometry samples fail at lower strain than the uniaxial geometry samples). However, there are some differences that are not so clear, such as when the range defined by the standard deviation of one set of data partially overlaps with that of another set. To be able to assess if there is an appreciable difference between some of these sets of data, a quantitative procedure such as the statistical hypothesis test is necessary.

3.3 Hypothesis Tests

When working with multiple test parameters and repeat measurements at each of those sets of parameters, it is important to be able to summarize the most likely result if one additional repeat is performed (the mean) as well as a number representing the spread of where that number is most likely to fall (the standard deviation). However, when proceeding to compare the means and standard deviations of two different combinations of test parameters, it becomes necessary to introduce a hypothesis test. The argument that is satisfactory to convince most people is that if the mean of a Simple Random Sample (SRS) of the first set of parameters, \bar{x}_1 , crosses over in magnitude the mean of a SRS of the second set of parameters, \bar{x}_2 , for no more than one in twenty samples, then it can be said that the population means μ_1 and μ_2 are significantly different [50]. There is a shortcut that was devised by Student [51] to avoid having to perform at least twenty SRS for each distinct set of parameters; it's called the two-sample t-test.

In the previous section, one pair of data that saw their standard deviations overlap was the Phase I vs. Phase II 0° uniaxial pair (the leftmost pair of bars in Figure 3.5). It would therefore be prudent to perform a means comparison test here to judge if it can be declared that Phase I samples of the 0° uniaxial geometry are more ductile than those of Phase II. If the null hypothesis that Phase I 0° uniaxial samples are just as ductile as Phase II 0° uniaxial ones can be shown to not be likely to happen, except for less than or exactly 1 time in 20, then the

alternative hypothesis is accepted, that Phase I 0° uniaxial samples are on the average more ductile:

$$H_0: \mu_1 - \mu_2 = 0 \quad H_1: \mu_1 - \mu_2 > 0$$

Analyzing the data provided (see Table 3.2), the mean and standard deviation of the sample elongations to failure are obtained and summarized in Table 3.3.

Sample	Phase I	Phase II
1	14.7	10.9
2	13.0	9.4
3	16.4	11.2
4	9.7	5.3
5	14.5	4.6
6	12.8	14.7
7	13.4	
8	9.6	
9	14.5	
10	19.1	

Table 3.2 – The elongation to failure of all 0.001 s⁻¹ 0° uniaxial tests (all figures in percent engineering strain)

Group	Sample Origin	N	\bar{x}	S
1	Phase I	10	13.8%	2.8%
2	Phase II	6	9.4%	3.8%

Table 3.3 – A summary of the basic statistics

A pooled variance estimate should be made to simplify the problem. This is reasonable to do if there is a sufficient level of confidence in the population variances being equal. To determine this, the sample variances are subjected to an F-test, using a 5% significance level.

$$H_0: \sigma_1 = \sigma_2 \quad H_1: \sigma_1 \neq \sigma_2$$

$$F = \frac{s_2^2}{s_1^2} = \frac{3.8^2}{2.8^2} = 1.84$$

This value is now compared to the F(5,9) distribution. A table of F-values shows that 1.84 is less than the 0.025 critical value of the F(5,9) distribution, which is F* = 4.48. And because

this was a two-sided test, this means that the results are only significant at a level greater than 5%. Therefore, as this is rather weak evidence, we fail to reject the null hypothesis and for the purposes of this question assume the population variances are equal.

Next, the pooled sample standard deviation is calculated, which will then be used in a t-test:

$$s_p = \sqrt{\frac{(n_1 - 1)s_1^2 + (n_2 - 1)s_2^2}{n_1 + n_2 - 2}} = \sqrt{\frac{(10 - 1)2.8^2 + (6 - 1)3.8^2}{10 + 6 - 2}} = 3.2\%$$

The pooled two-sample t statistic is then

$$t = \frac{\bar{x}_1 - \bar{x}_2}{s_p \sqrt{\frac{1}{n_1} + \frac{1}{n_2}}} = \frac{13.8 - 9.4}{3.2 \sqrt{\frac{1}{10} + \frac{1}{6}}} = 2.6$$

A table of t-values shows that 2.6 is greater in magnitude than the 0.05 critical value of the t(14) distribution, which is $t^* = 1.761$. Using a t-distribution calculator, the actual p-value is approximately 0.0082. So the data provides strong evidence that the null hypothesis may be rejected, and Phase I 0° uniaxial samples are on the average more ductile than Phase II 0° uniaxial ones ($t = 2.7$, $df = 14$, $P = 0.82\%$). This is even more convincing if one considers that this was the more conservative of the testable uniaxial sample cases. As seen in Figure 3.5, the standard deviation of the 90° uniaxial bars do not overlap; a follow-up means comparison test using this data would yield a P-value that is even lower than 0.82%.

The preceding analysis can be applied to the comparison of all the other sets of parameter combinations to find whether the differences between the means are statistically significant. Table 3.4 and Table 3.5 show summaries of the findings.

	Phase I; 0° uniaxial	Phase I; 90° uniaxial	Phase I; 0° a/R=0.25	Phase I; 0° a/R=1	Phase II; 0° uniaxial	Phase II; 90° uniaxial	Phase II; 0° a/R=0.25	Phase II; 0° a/R=1
Phase I; 0° uniaxial		Y	Y	Y	Y			
Phase I; 90° uniaxial			Y	Y		Y		
Phase I; 0° a/R=0.25				Y			Y	
Phase I; 0° a/R=1								Y
Phase II; 0° uniaxial						?	Y	Y
Phase II; 90° uniaxial							Y	Y
Phase II; 0° a/R=0.25								Y
Phase II; 0° a/R=1								


Y = yes
 ? = inconclusive
 = intriguing finding

Table 3.4 – Significant difference summary matrix: Engineering stress at 2% nominal strain

	Phase I; 0° uniaxial	Phase I; 90° uniaxial	Phase I; 0° a/R=0.25	Phase I; 0° a/R=1	Phase II; 0° uniaxial	Phase II; 90° uniaxial	Phase II; 0° a/R=0.25	Phase II; 0° a/R=1
Phase I; 0° uniaxial		Y	Y	Y	Y			
Phase I; 90° uniaxial			Y	Y		Y		
Phase I; 0° a/R=0.25				Y			Y	
Phase I; 0° a/R=1								?
Phase II; 0° uniaxial						?	Y	Y
Phase II; 90° uniaxial							Y	Y
Phase II; 0° a/R=0.25								Y
Phase II; 0° a/R=1								


Y = yes
 ? = inconclusive
 = intriguing finding

Table 3.5 – Significant difference summary matrix: Elongation to failure

A majority of the comparisons show that there is a statistically significant difference, which means that all of the trend observations made in section 3.2 hold up to scrutiny. It also means that a sufficient number of samples were tested, as decided upon in the experimental design phase of the project.

Half of the highlighted “intriguing findings” in the preceding two tables have to do with the effect of orientation, which turned out to be the least conclusive effect. A different approach will have to be taken in order to assess the effect orientation has on the constitutive response.

The other half of the findings have to do with comparing elongations to failure between Phase I and Phase II samples. There were large enough sets of data collected to show that there is a significant difference for all sample geometries except for $a/R=1$. If additional tests were procured, the sample origin discrepancy in elongation to failure would become a statistically significant one for the $a/R=1$ case as well.

3.4 Anisotropy Evaluation

The transverse anisotropy of the material was investigated by calculating the r-value of the Phase I uniaxial samples using the method outlined in Chapter 2. Figure 3.6 shows the evolution of the r-value up to the ultimate tensile stress for each repeat test to illustrate the inherent spread in the measured data. The dashed and dotted lines represent the average r-value for each orientation for simpler comparison. There are ten tests that were done in the 0° direction, and six tests done in the 90° direction.

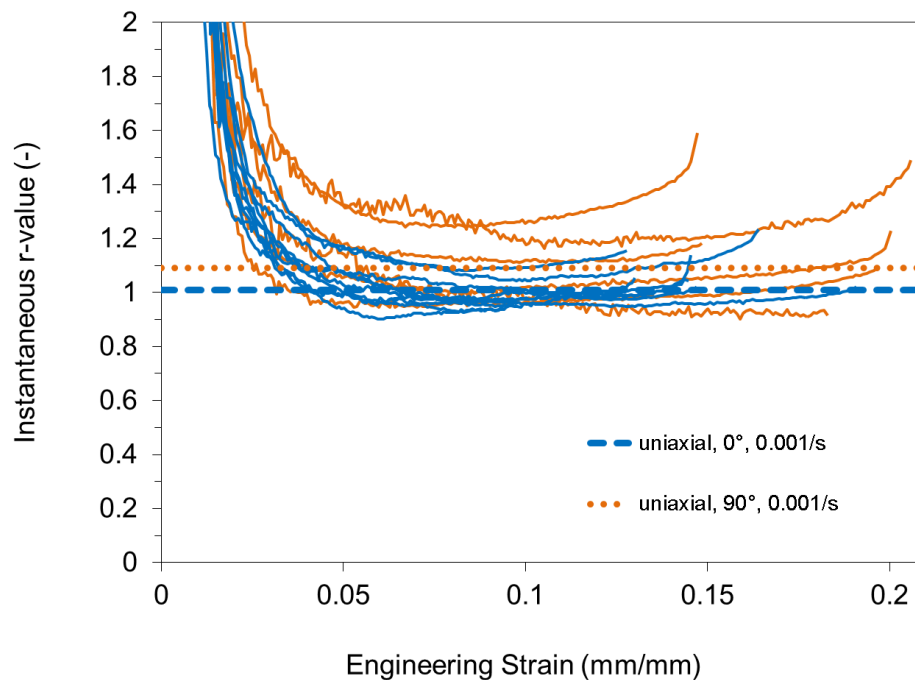


Figure 3.6 – r-value curves of all Phase I uniaxial repeat tests

The in-plane anisotropy can be assessed by comparing average r-values from the 0° and 90° samples, which were 1.0 and 1.1, respectively. These levels lie within their respective scatter bands which overlap, suggesting a relatively mild degree of in-plane anisotropy. The fact that both average r-values are greater than unity indicates that material flows plastically in-plane slightly more readily than it does in the thickness direction for samples in both orientations. However, the r-values are close to unity, again suggesting a mild level of anisotropy.

3.5 Considère Analysis

Based on the uniaxial stress-strain response it appears that there is minimal necking and post-uniform softening. Considère [52] studied the constitutive behaviour of materials and determined that the onset of necking will commence when:

$$\frac{d\sigma_T}{d\varepsilon_T} = \sigma_T, \quad (16)$$

where σ_T and ε_T denote the true stress and true strain, respectively. The true stress-strain curves were smoothed by second order polynomial fits to minimize the noise generated when applying Considère's criterion. To determine the optimal type of fit, higher order polynomial fits were attempted. However, the models oscillated slightly above and below their respective raw curves to the point where it was decided to have a slightly inferior r-squared value (99.6% instead of 99.9%) in favour of avoiding the artificial oscillations. A comparison of the polynomial fitting effect on the stress-strain response for three Phase I 0° uniaxial samples (one exhibiting minimum elongation to failure, one exhibiting median elongation to failure, and one exhibiting maximum elongation to failure) is shown in Figure 3.7. In Figure 3.8, the Considère analysis is carried out on the three aforementioned 0° uniaxial samples.

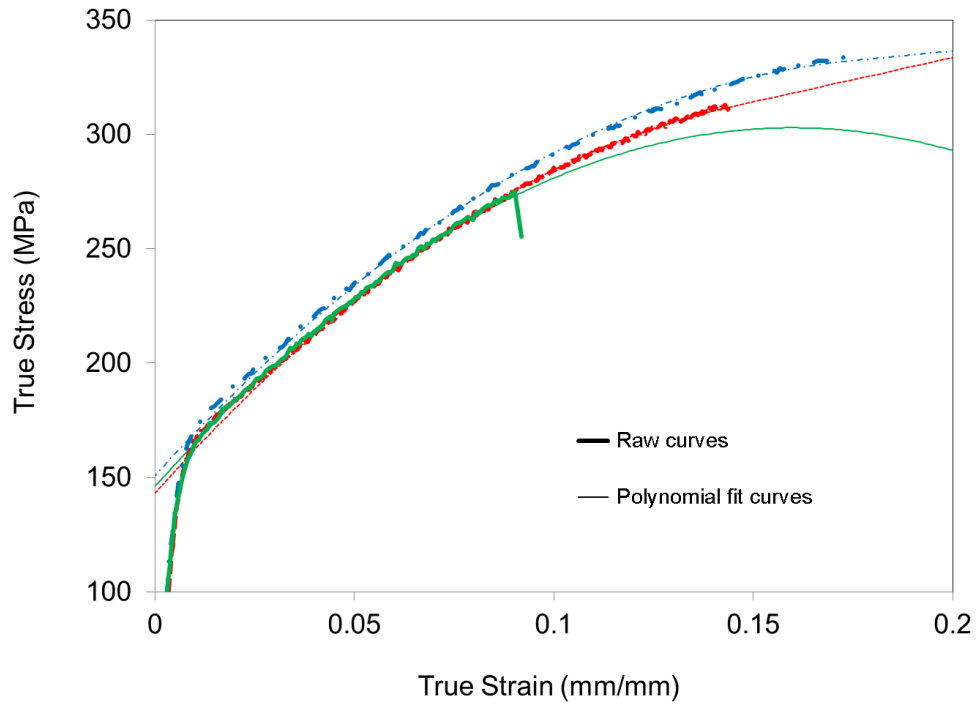


Figure 3.7 – The polynomial fits adopted for the Considère analysis

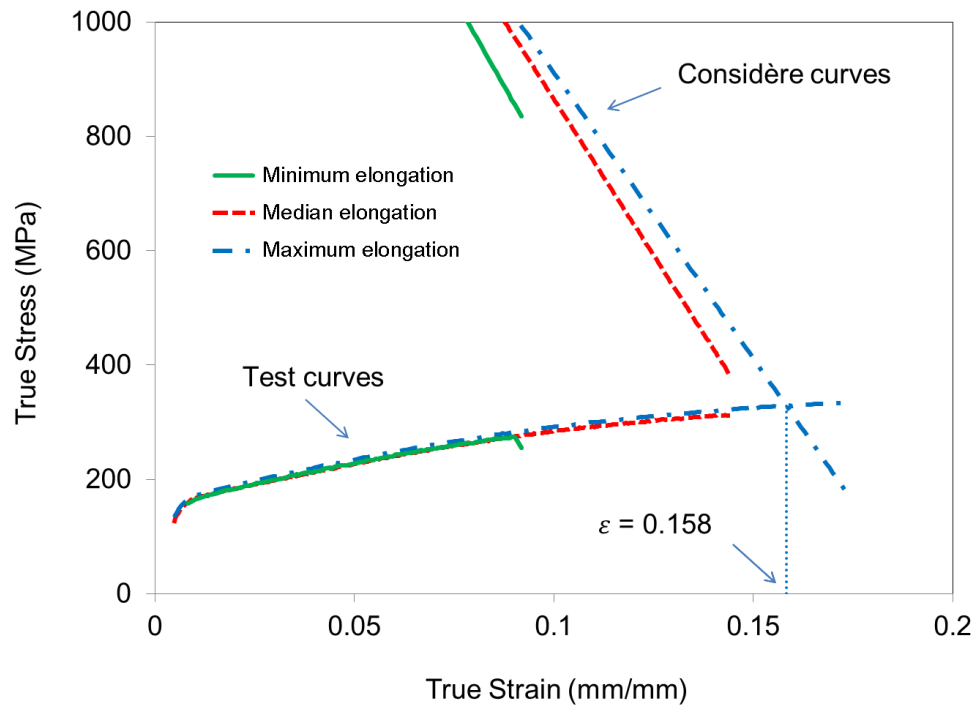


Figure 3.8 – Applying the Considère approach to selected Phase I 0° uniaxial tests

For most of the tests, represented by the median case, the curves do not intersect; therefore, the Considère point is not reached and the onset of necking is not expected which suggests that fracture occurs prior to significant necking. Performing the same analysis on the test that showed the larger elongation to failure, however, it is found that there is a Considère point at a true strain of 0.158. However, there are no visibly appreciable signs of necking from this point until failure.

3.6 Effect of Strain Rate

An opportunity arose to investigate the effect that elevated tensile strain rate has on AM60B magnesium. A small number of tests were performed at 10 s^{-1} (three tests for ‘uniaxial, 90° ’ and a single test for the other three geometries; see Appendix A for more details), so unfortunately, a reliable estimate of the spread in data is unavailable. Instead, a more qualitative assessment of the inherent trends is provided herein. Figure 3.9 shows median stress-strain data for the four previously described conditions, then adding data for those conditions at the strain rate of 10 s^{-1} .

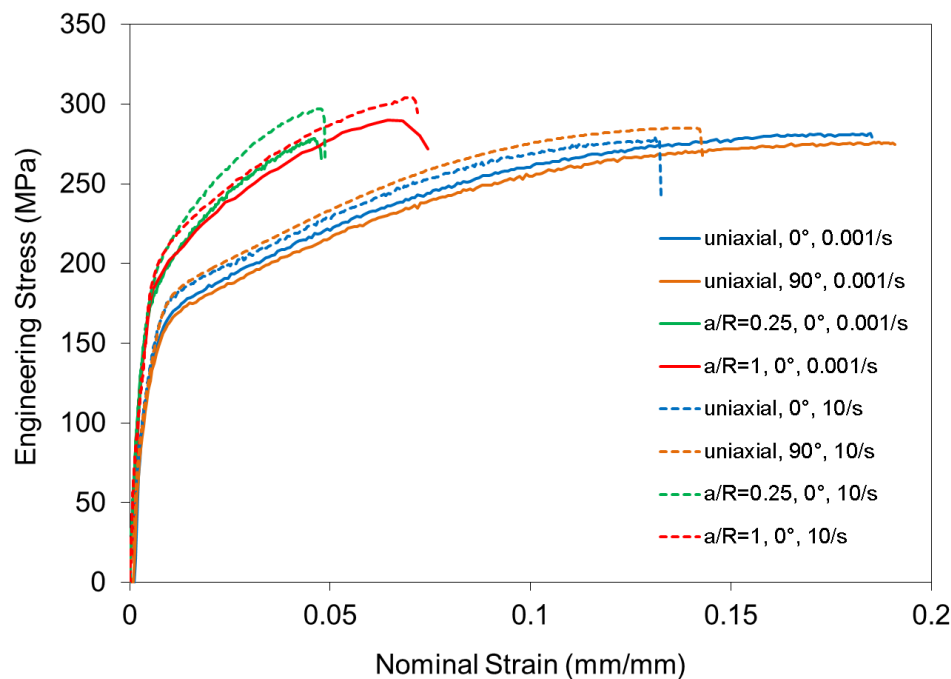


Figure 3.9 – Median engineering stress-nominal strain results for all geometries, orientations, and strain rates under study

There are three main trends to be observed. First, there is on average 4-8% positive strain rate sensitivity for all of the different geometries and orientations tested. Second, there appears to be a strength differential with respect to orientation that changes with strain rate when comparing the two uniaxial conditions; however, this differential may be within the error band of the observed data. More tests at a strain rate of 10 s^{-1} would be required to determine the statistical significance of this stress differential. Third, for the $a/R=0.25$ notched sample geometry, the work hardening rate is shown to increase as strain rate is increased.

3.7 Effect of Sampling Location within the Cast Component

It would be ideal if identical mechanical properties are displayed at all locations on a cast component. However, this may not be the case here. Recalling the way in which the die is fed with molten metal (recall Figure 2.1b), it could be hypothesized that in the absence of finely tuned heating cartridges adjacent to the entire surface area of the component, differing cooling gradients may be present. Specifically, the molten metal injected first and therefore coming to rest near the output channel will be further from the molten metal bath it originated from. This may make for a quicker cooling time, differing microstructure, and strength, for example. Conversely, molten metal injected last and therefore coming to rest near the input channel may undergo a slower solidification process.

A limited number of the total population of samples was taken from locations other than the top of the phase I components. The following figures (Figure 3.10, Figure 3.11, and Figure 3.12) assume that no significant variance in mechanical properties between components exists. This is done to be able to include a larger total number of samples, and therefore to visually add assurance that any variation seemingly due to location may be greater than the standard amount of variation inherent in the casting process. The location is denoted in the legends in a shorthand manner, with “I” meaning the input side and “O” meaning the output side. The five discretized locations are also colour-coded, adopting the following convention:

- Red = Top
- Blue = Output Side
- Green = Input Side
- Orange = Output Flange
- Purple = Input Flange

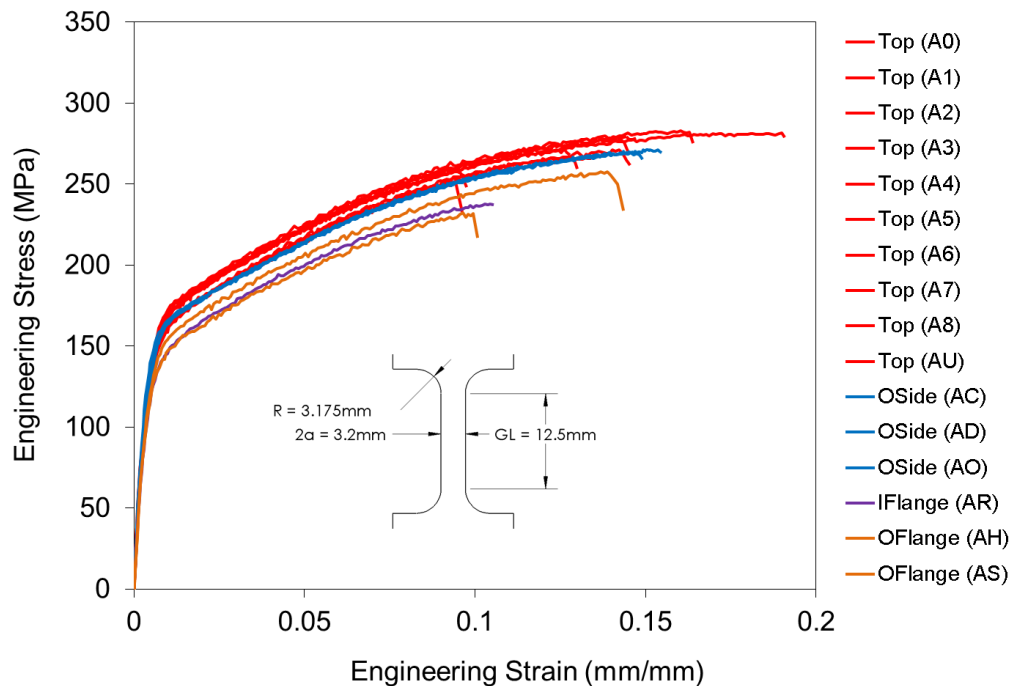


Figure 3.10 – Selected 0° uniaxial tensile results, at a nominal strain rate of 0.001 s⁻¹

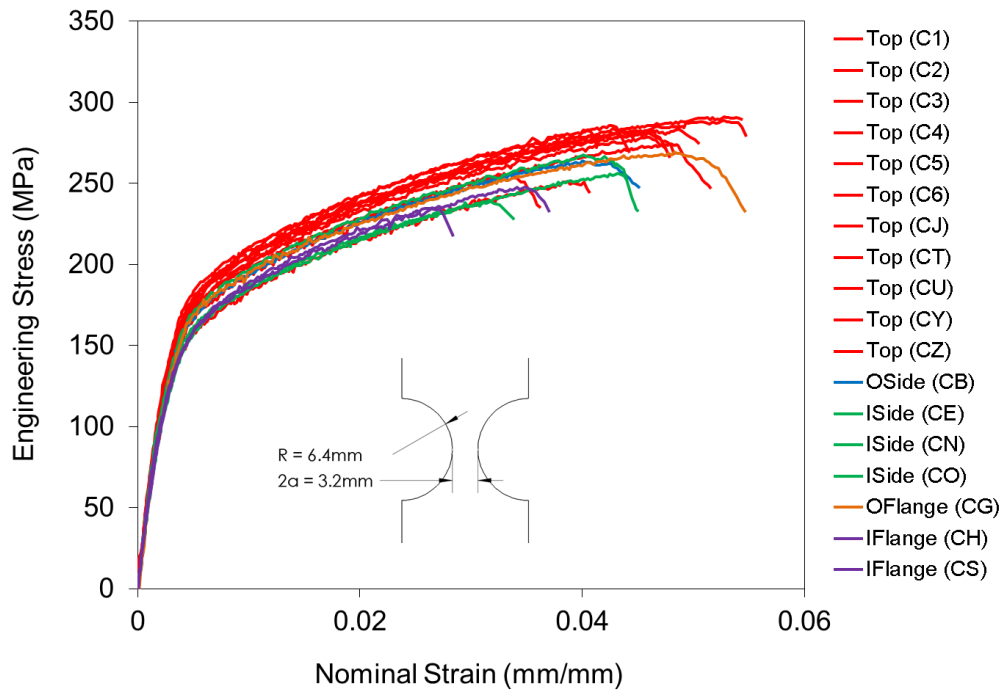


Figure 3.11 – Selected 0° $a/R = 0.25$ tensile results, at a nominal strain rate of 0.001 s^{-1}

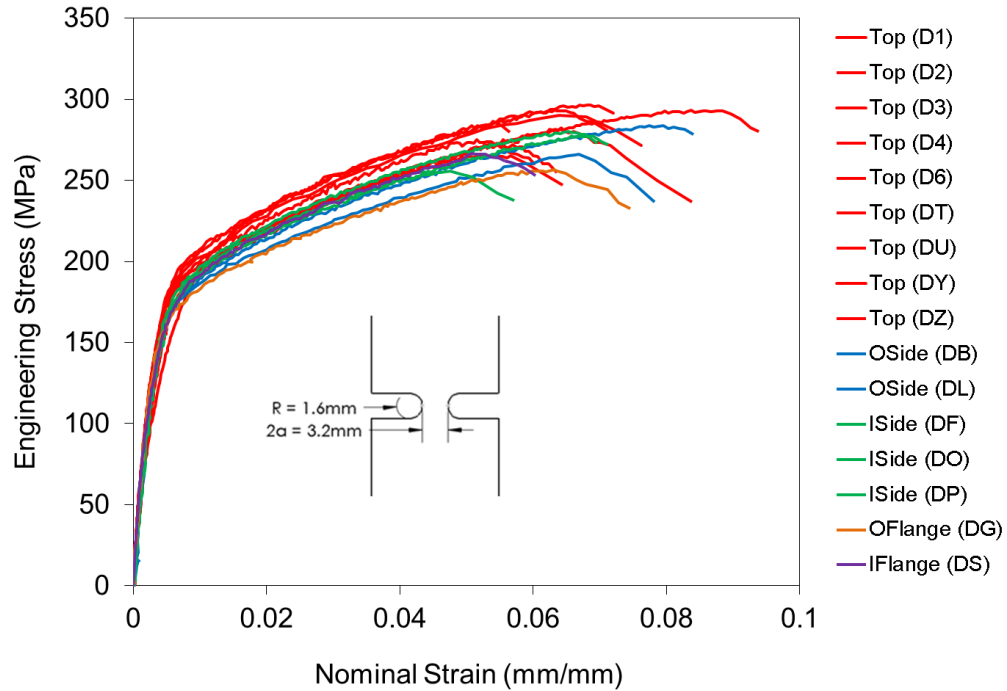
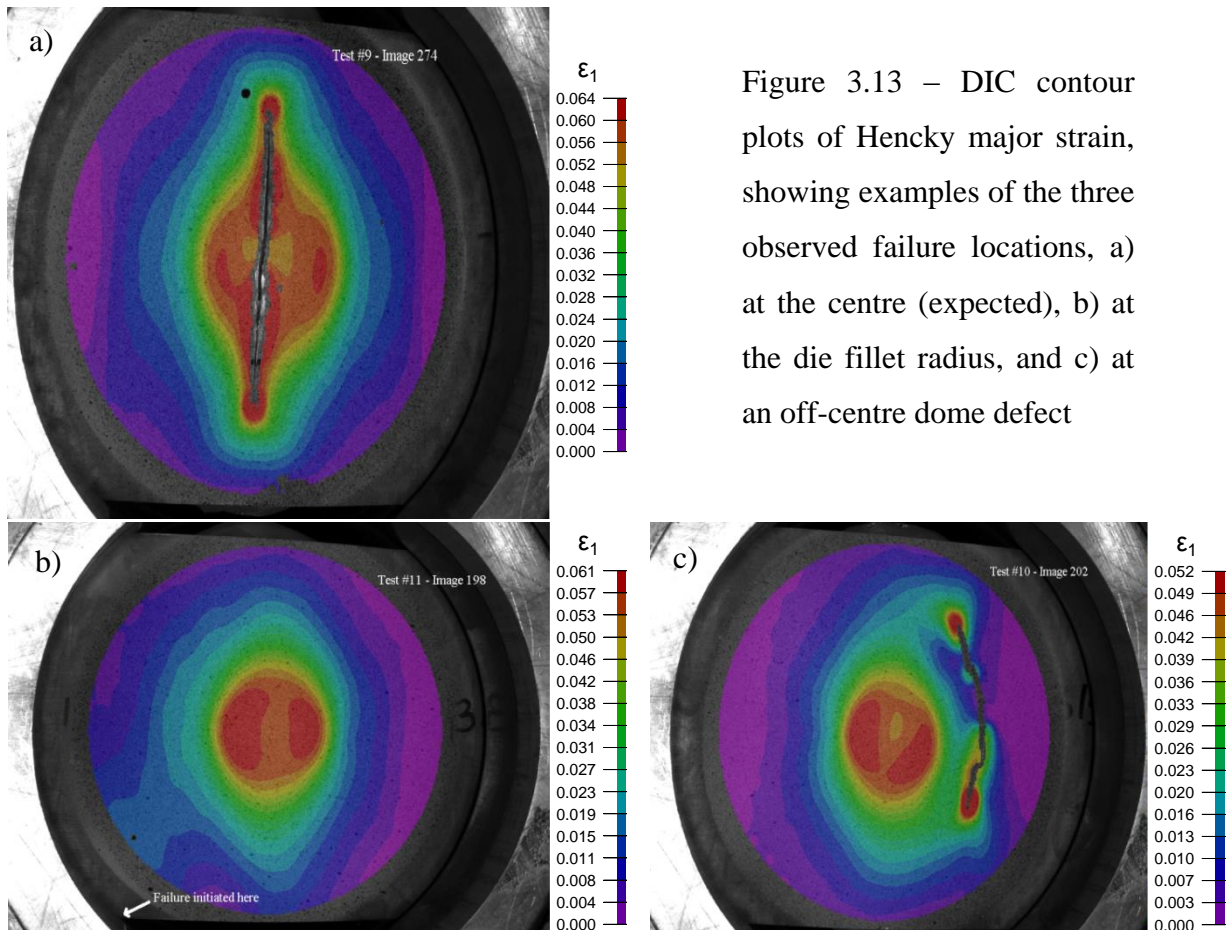


Figure 3.12 – Selected 0° $a/R = 1$ tensile results, at a nominal strain rate of 0.001 s^{-1}

There are certain trends that are observed from the stress-strain data shown in the preceding three figures. For one, the stress-strain data of samples taken from the top location on the component always demonstrates the highest yield stresses. This is most evident in Figure 3.10, where the range of yield stresses of the individual top samples is least, and therefore the most striking. On the other end of the spectrum, samples taken from the two flange locations demonstrate the lowest yield stresses. Samples taken from the two side locations appear to fall somewhere in between. Another trend that is observed is that samples taken from the two flange locations appear to fail sooner, exhibiting lower elongation to failure on average. Finally, the results suggest that there is no significant discrepancy in mechanical performance between output and input locations.

3.8 Biaxial Hemispherical Dome Test Results

There were a total of eleven biaxial hemispherical dome tests performed. Of this total, only two deformed and failed in the manner that was expected, i.e. developing a crack that spans the 87.0 mm minor direction, and initiating from the centre of the punch location (see Figure 3.13a). There were two other failure locations encountered that were termed “die fillet radius” and “off-centre dome defect” (Figure 3.13b and Figure 3.13c, respectively). Four of the eleven tests had to be halted prematurely, as tearing at the die fillet radius was occurring. Also, another five of the eleven tests exhibited failure at a location away from the centre, which led to the hypothesis that a defect in the dome region (away from the centre) must have been present; when it experienced tensile loads the defect opened up and propagated a catastrophic fracture.



To begin to analyze the results, the load signal is coupled with the displacement signal to show how the force increases as the punch moves through and eventually fractures the sample (see Figure 3.14).

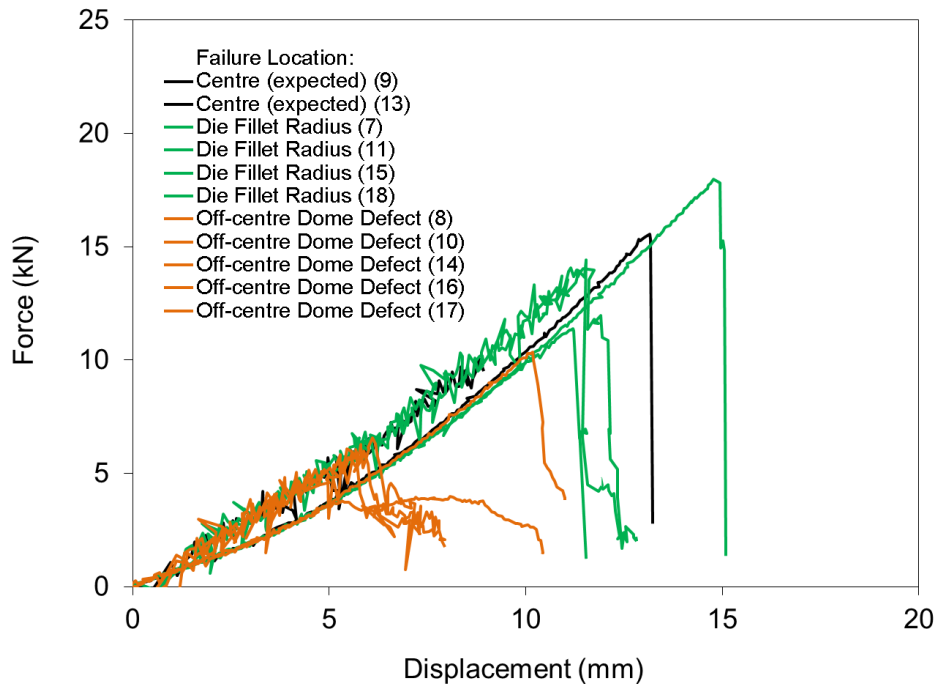


Figure 3.14 – Force-displacement results of the biaxial hemispherical dome tests

A bimodal distribution of the load curves is observed, with the tests performed in the second laboratory location presenting higher loads early on in the deformation process. The new load cell also had a comparatively noisier signal due to a calibration issue, which is evident in the upper set of curves.

Following the procedure described in section 2.5, the next step in obtaining the results is to use the DIC software to establish an AOI and track the evolution of major and minor strain with time. This time record is then used in determining how far the punch has displaced. Four plots displaying these types of values are shown in Figure 3.15.

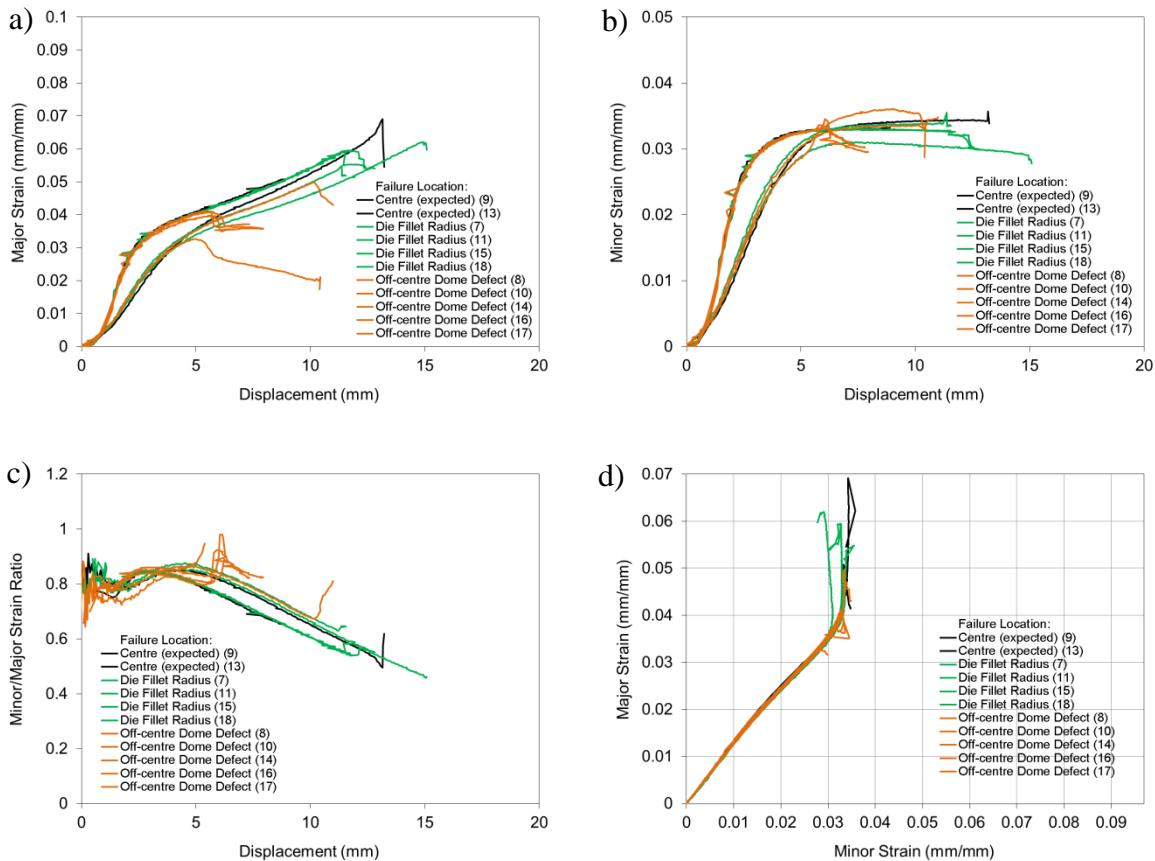


Figure 3.15 – Major and minor strain plots obtained from the biaxial hemispherical dome tests, a) major strain vs. displacement, b) minor strain vs. displacement, c) minor/major strain ratio vs. displacement, d) major strain vs. minor strain

A bimodal distribution of the major and minor strains is seen, and is wholly attributed to the change in experimental setup. The major and minor strains both accumulate with dome displacement at a consistent rate, with minor strain accruing at a rate of roughly 80% that of major strain, as seen in Figure 3.15c. This is also evident by the nearly straight line with a slope of approximately 5/4 in Figure 3.15d, up until a minor strain of about 0.03. The major strain then continues to be accumulated, as seen in Figure 3.15a, albeit at a reduced rate. However, the minor strain saturates, as seen in Figure 3.15b and c. The bimodal behaviour attributable to the change in calibration due to test apparatus relocation is also visible in all four figures. Post-uniform elongation is generally minimal, which agrees with the tensile test findings. There is post-uniform elongation seen for the off-centre dome defect propagated

failures, but this is because at the ultimate major strain level, the load is still low enough so that the crack will not be able to immediately propagate through the entire width of the sample. The crack instead slowly grew as the displacement of the punch continued. As the off-centre dome defect trials were not a primary interest of this study, some trials were halted before the crack could span the entire width of the sample.

3.9 Metallographic Findings

The porosity of cast samples can have a major impact on its mechanical properties. As was suggested earlier, this may be the primary reason for the disparity in strength and ductility between samples from Phase I and Phase II. In this work, samples were prepared for viewing under an optical microscope, to digitally segregate voids from the matrix material and to obtain an area porosity figure which can then be approximated as the bulk volumetric porosity.

This process began by adopting a grinding and polishing schedule. The grinding portion of the schedule used 400 to 1600 grit sandpaper along with water as lubricant. The polishing portion used 1 μm diamond paste and ethanol as lubricant [53]. This part of the sample preparation proved to be the most artful, because occasionally moisture residues remained after aspirating the ethanol and magnesium particles from the surface. If this was the case, corrosion and/or iridescence of ethanol residues was found on the polished surface under the microscope, so the polishing step had to be repeated.

The next step involved digital image analysis using ImagePro Plus 7.0. A qualitative optimization study involving what the threshold greyscale level should be to separate voids from matrix material was performed. The standard adopted was a grey level of 145 out of 255 (1-145 means the pixel in question is part of a void and 146-255 means it is part of the matrix). Setting this threshold level in ImagePro yields an indexed image such as that seen in Figure 3.16.

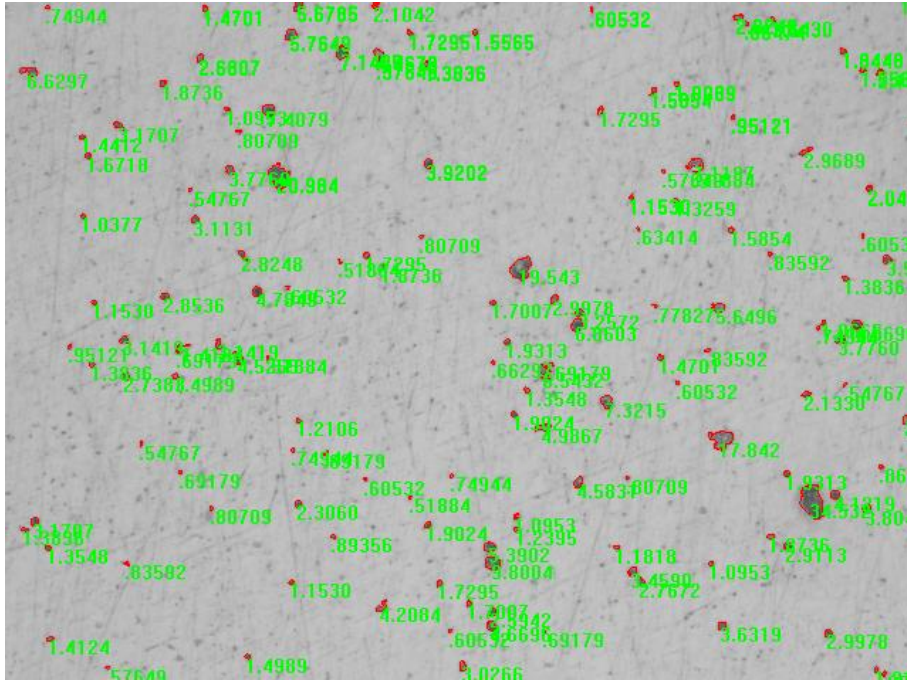


Figure 3.16 – Using pixel greyscale levels to determine void boundaries (in red)

It is then possible to extract data containing the surface areas of all identified voids. The sum of all void areas divided by the total area defined by the AOI is then the surface porosity. This procedure was applied to the comparison of porosity in samples from Phase I and Phase II. A set of micrographs visually comparing the two samples is shown in Figure 3.17.

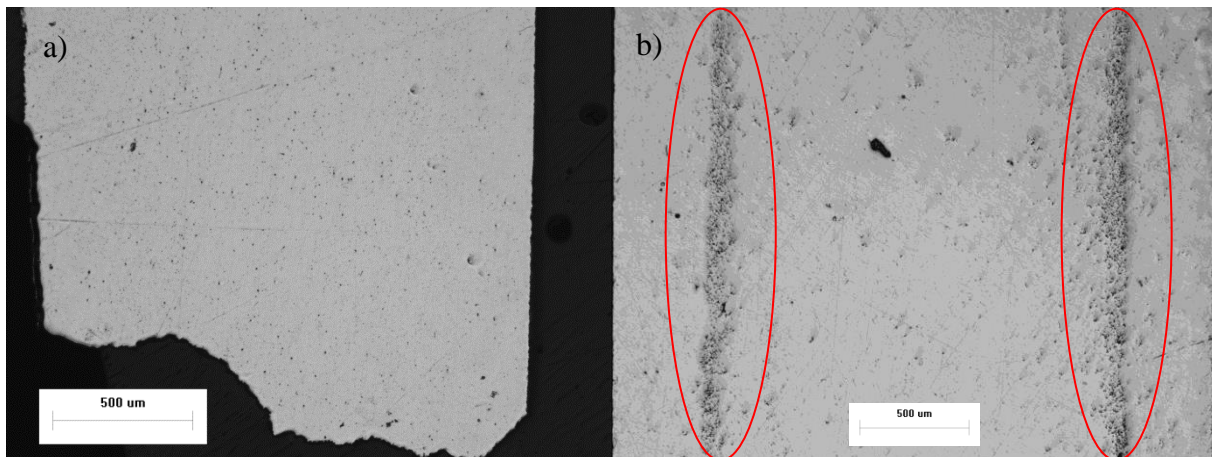


Figure 3.17 – Example optical micrograph set displaying the length-thickness plane of a) a failed Phase I sample (M=8x), b) an untested Phase II sample (M=6.25x)

It is found that Phase I samples are very uniform in their void distribution, with this single failed sample (see Figure 3.17a) exhibiting an overall porosity estimate of 1.4%; it is presumed that an as-received sample would show slightly lower porosity. This level of porosity falls within the range reported by Weiler *et al.* [31]. By contrast, Phase II samples were found to contain zones of segregated porosity (circled in Figure 3.17b) about 100 μm thick that run in the length and width directions and are located approximately 400 μm from each free surface of the casting. The presence of porosity bands was also observed by Chadha *et al.* [35], although the bands observed in the current work were more distinct, as they run along the entire length of the sample and exhibit a consistent thickness. Another notable difference is the Chadha *et al.* porosity bands appeared at a variety of distances from the free surface (recall Figure 1.9b). The overall volumetric porosity estimate for the Phase II samples was 6.4%. The presence of the segregated porosity bands in Phase II samples are concluded to contribute to the lessening of material performance. For example, in the paper published by Sannes *et al.* [36], there was a 45% decrease in elongation to failure noted for samples containing segregated porosity bands. Performing a quick comparison to samples in this study, 0° and 90° uniaxial tensile samples showed a 33% and 34% decrease in elongation to failure, respectively.

For the sake of completeness, it should be noted that micrographs representing samples tested at the other stress states were also obtained. There was no appreciable difference in the levels of porosity observed, so the micrographs are not included in the present analysis. As a follow-up investigation to the location dependence study carried out in Section 3.7, a sample was studied from the output flange location on the component. However, a post-test polished surface (the same conditions as the sample shown in Figure 3.17a) indicated a porosity level that was within range of other Phase I results (0.8%).

Scanning Electron Microscopy (SEM) was carried out on a select few post-test samples to investigate what failure modes were involved. Orientation effect was omitted in this analysis; all samples presented were extracted from the 0° orientation. To begin, low-magnification fractographs of samples from Phase I and II are presented in Figure 3.18 and Figure 3.19, respectively.

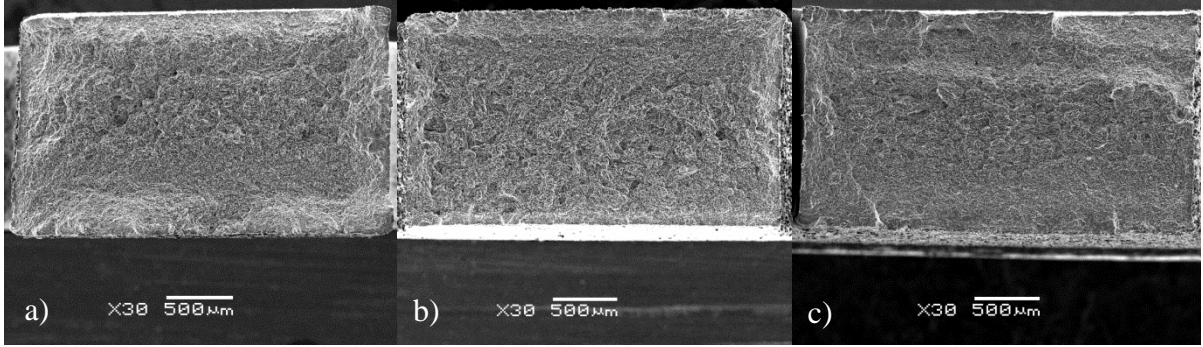


Figure 3.18 – Example Phase I SEM fractographs displaying the width-thickness plane, a) uniaxial, b) $a/R=0.25$, c) $a/R=1$

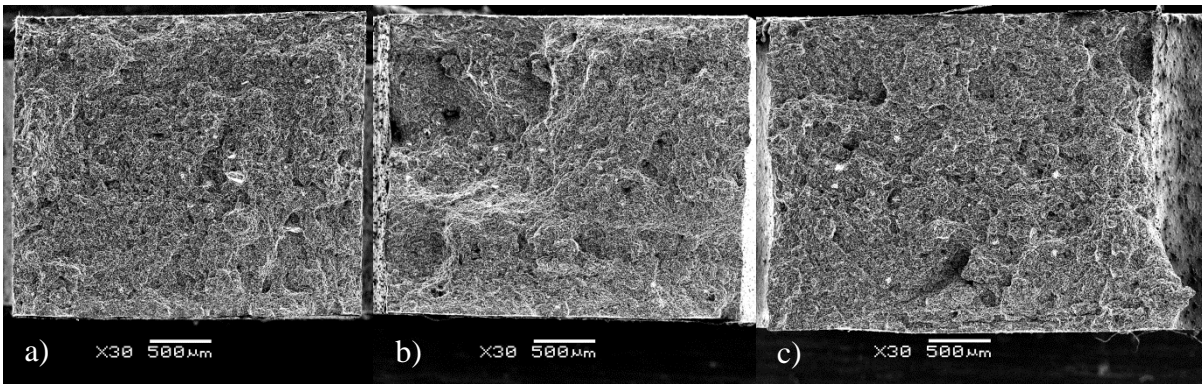


Figure 3.19 – Example Phase II SEM fractographs displaying the width-thickness plane, a) uniaxial, b) $a/R=0.25$, c) $a/R=1$

Figure 3.18a appears to exhibit a “cup-cone” morphology, with slight shear lips, characteristic of ductile fractures. The shear lips are less prominent in the $a/R=0.25$ fractograph (Figure 3.18b), and disappear completely in the $a/R=1$ fractograph (Figure 3.18c). This may be evidence of a quasi-ductile to quasi-brittle failure mode transition as the degree of constraint increases. This trend is in agreement with the work done by Yan *et al.* [27], although the constraint levels studied in the present work didn’t cover as large of a range, meaning any observable transition would be less distinct.

The Phase II samples (Figure 3.19) also exhibit a rough fracture surface, but without evidence of shear lips. One feature worth noting is found on the bottom-right side of Figure 3.19c; there a protruding “cone” is found, which may simply be the result of a large grain forcing the crack

propagation up out of the plane of the fracture surface. However, it may also be a sign that some necking was accrued before the final fracture.

Another trend to point out about the preceding two figures is the effect of the greater levels of porosity present in the Phase II samples. For instance, comparing the phase I sample in Figure 3.18b with the Phase II sample in Figure 3.19b, it is apparent that the phase I sample failed in a uniform manner, likely by coalescence of multiple microcrack nucleation sites into the propagating failure crack. The phase II sample, however, shows a significant crater on the top-left quadrant of its fracture surface. A possible explanation for this is that the porosity segregation bands caused partial matrix delamination at the location approximately 400 μm from the free surface (the top in this image) and failed prematurely.

To get additional information about how the samples fail, high-magnification micrographs were obtained and studied (see Figure 3.20).

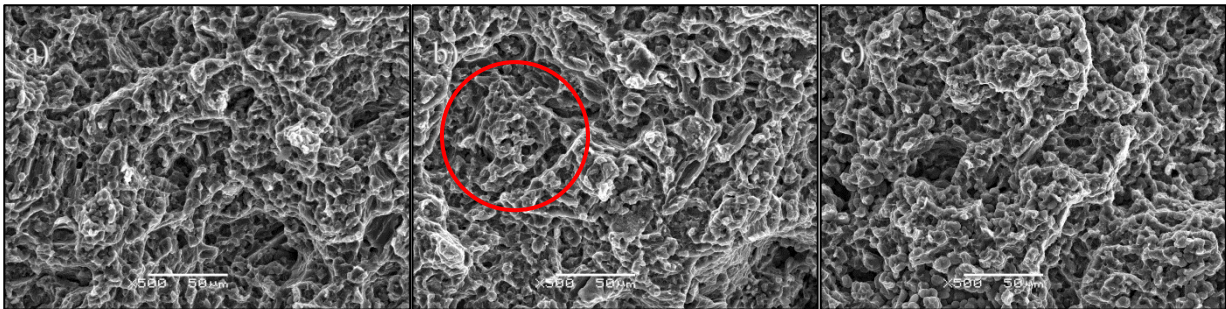


Figure 3.20 – Random representative Phase II 0° oriented SEM micrographs (M=500x) taken near the centre of each fracture surface, a) uniaxial, b) $a/R=0.25$, c) $a/R=1$

The jagged morphology suggests that these samples failed by intergranular fracture. Also visible are features (one example circled in Figure 3.20b) that may be protruding grains. The alloy additions of AM60B (mainly the 5.5% aluminum) would tend to aggregate within the grain boundary volume, degrading the adherence of neighbouring grains and promoting brittle tearing. There are also some features that appear to be dimples (for example on top of the grain circled in Figure 3.20b), which would suggest that ductile failure mechanisms are also at work. Similar observations were made after studying Phase I high magnification SEM micrographs.

The preceding findings taken together suggest that AM60B samples fail following a hybridization of ductile and brittle failure mechanisms, with the Phase I samples being closer to the ductile side of the spectrum and the Phase II samples closer to the brittle side of the spectrum.

3.10 Sandblasting Investigation

As the project progressed, there was mounting uncertainty regarding the effect that sandblasting the samples prior to testing had on the mechanical properties. This section will investigate to what extent sandblasting roughened the surfaces of the samples, as well as what magnitude of thickness was removed. The magnitude of thickness removed would never be truly consistent, as the sandblasting was done by hand; there will always be slight variations in the amount of time spent lingering over each individual sample. The standard adopted for the sandblasting procedure was to use fine grit sand, a pressure of 60 psi, and to linger for 3 seconds over each sample.

Five subsamples of five separate Phase II components that were roughly twice the size of a tensile sample were obtained. Each of these subsamples was cut in half, keeping track of which half belonged to which component. One of the pair of halves was left as is, acting as the control sample. The other halves were subjected to the sandblasting procedure. A sample pair of micrographs is presented in Figure 3.21. Referring to the figure, the sand was meant to spray the left face, located on the length-width plane of the sample. However, as the spray was moved from side to side (in the width direction), similar to a spray-painting motion, it is evident that it roughens and removes some material from both sides of the sample (on the length-thickness plane) as well (see Figure 3.21b).

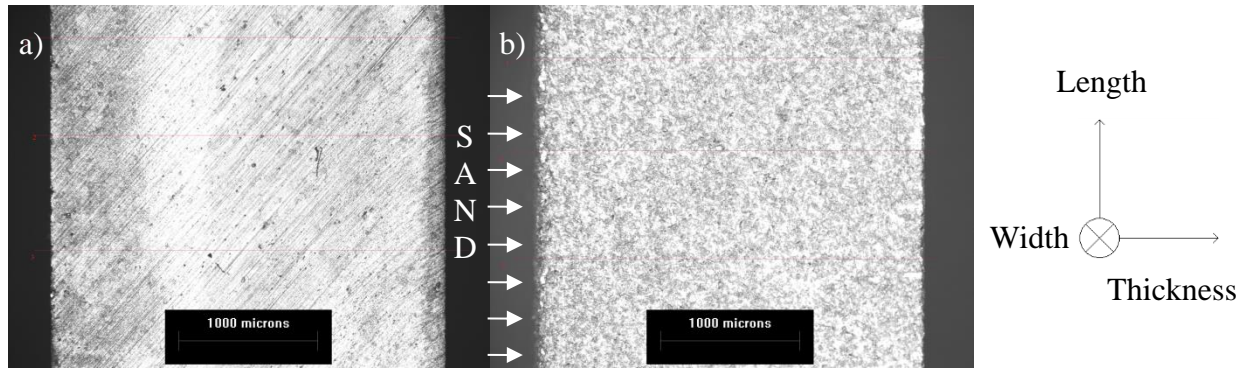


Figure 3.21 – Optical micrographs ($M=5\times$) of the nominally 2.8 mm thick unpolished length-thickness planes, a) pre-sandblasting, b) post-sandblasting

Observing the samples under the optical microscope, the surface of the sandblasted sample is noticeably rougher. This will affect the sample's ductility, with two competing factors involved. The benefit is that the high energy impact of each grain of sand introduces a localized compressive plastic strain onto the surface, which, when tested in tension will allow the gauge area to accrue additional strain prior to failure as it now begins from this net compressive pre-strained state. The detriment arises as there are topographical peaks and valleys created when sandblasting, and at the base of each valley there would be an inflated stress concentration factor leading to potential crack formation. The thicknesses were digitally measured using still images. At least three thickness determinations were made for each sample, changing the location each time. The differences in the averages between the pre-sandblasting and post-sandblasting samples extracted from the same component were themselves averaged. The conclusion was that 0.032 ± 0.019 mm of material was removed, or a $1.1\pm 0.66\%$ reduction in thickness. Although this sounds like a small amount, the outer skin is an important part of the material, being a cast component. During casting, the initially high cooling rates present as the solidifying metal loses heat into the surrounding die would have led to a finer average grain size and therefore increased local strength due to the Hall-Petch relationship [54].

4 NUMERICAL MODEL

In this chapter, the development of the three tensile and the biaxial hemispherical dome finite element models is documented. A mesh convergence study is performed to determine the element size adopted. Details of the steps taken in developing the linear piecewise plasticity material model are also included.

4.1 General Approach

A finite element model was developed to predict quantities that cannot be directly measured in the lab, such as stress triaxiality. The simulations were run on a single precision version of LS-DYNA, from a personal computer. Explicit time step integration was used to handle the contact treatment in the hemispherical dome test simulation. Then, to retain consistency, it was also used in the uniaxial and notched tensile test simulations.

4.2 Tensile Model

A mesh convergence study (in section 4.3) shows that a nominal element size of 0.1 mm is the most optimal in generating the true stress-strain response of AM60B. Figure 4.1 shows the meshes that were developed for use in the 2.0 mm thick models, where the inset views are used to show in greater detail the mesh resolution along the gauge regions. Figure 4.1a shows the uniaxial tension geometry, Figure 4.1b shows the $a/R=0.25$ notched tension geometry, and Figure 4.1c shows the $a/R=1$ notched geometry. The number of elements used and their respective computational times are listed in Table 4.1.

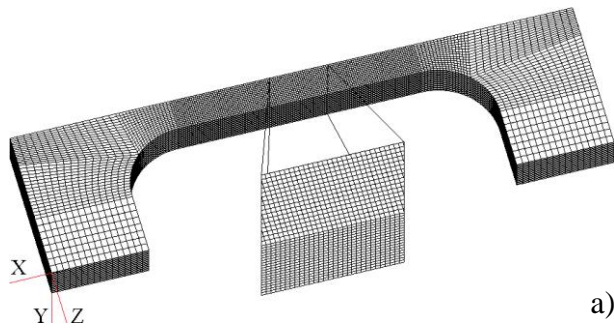
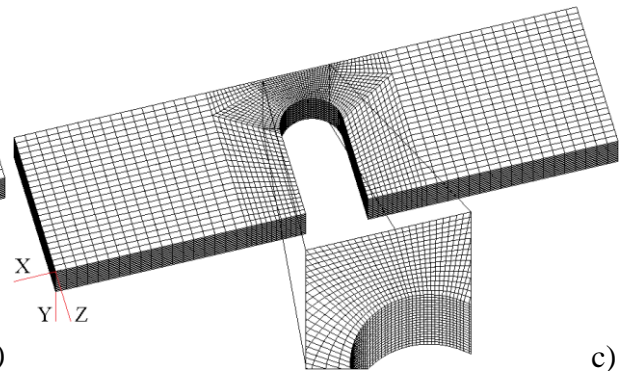
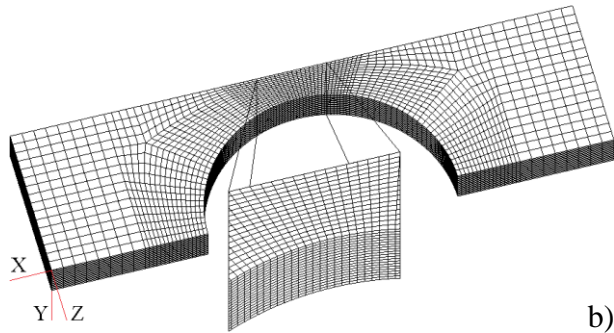


Figure 4.1 – Finite element meshes used, a) uniaxial tension, b) $a/R=0.25$ notched tension, c) $a/R=1$ notched tension



Sample Geometry	Number of Elements	Computational Time [hh:mm:ss]
Uniaxial	75,840	28:07:13
$a/R=0.25$	31,360	2:27:57
$a/R=1$	44,800	2:58:06

Table 4.1 – Number of elements and solution time for each sample geometry

Eight-noded single point integrated brick elements were chosen for use, with hourglass deformation suppressed using a stiffness-based hourglass control. To simplify the model, it was assumed that the material behaved isotropically.

The true stress-effective plastic strain relation found from the Phase I 0° uniaxial tests was used as the constitutive model for all four sample geometries under study. A linear piecewise plasticity material model with isotropic hardening that obeys the von Mises yield criterion was employed. A smooth polynomial fit of the true stress-effective plastic strain response up until the ultimate tensile stress was obtained from a single measured result curve exhibiting 15.5% elongation to failure. A piecewise combination of two polynomial fits best represented the

actual constitutive response. A fourth order polynomial fit was used for the initial elastic-plastic transition ($0 < \overline{\varepsilon}^p < 0.012$) and a second order polynomial fit was used up until the 15.5% elongation to failure level ($0.012 < \overline{\varepsilon}^p < 0.139$). All first differences of stress and strain increments were positive, and it was determined that there are no inflections present in the fourth order portion of the fit.

In order to have a complete constitutive relation to insert into a material model, it is necessary to include an estimation of the plastic behaviour up until a reasonably large $\overline{\varepsilon}^p$ level (250% was the standard that was adopted). This is necessary to allow strain that accumulates faster in certain local areas of the simulation's mesh to still have associated stress levels that have been defined. An extrapolation of an experimental plastic flow curve is therefore warranted.

One simple way to extrapolate a flow curve is to use the Hollomon [55] power law,

$$\sigma = K \varepsilon_p^n, \quad (17)$$

where K and n are empirical constants determined from known true stress-strain data before necking. Another method of determining the optimal extrapolation is to use a relation that includes a parameter controlling the shape of the curve. The relation should allow the extrapolated data to vary from a power law form up to a linear relation form, which are the lower and upper bounds of the post-necking behaviour. A relation developed by Ling [56] incorporates this:

$$\sigma = \sigma_u \left[w(1 + \varepsilon - \varepsilon_u) + (1 - w) \left(\frac{\varepsilon^{\varepsilon_u}}{\varepsilon_u^{\varepsilon_u}} \right) \right], \quad (18)$$

where σ_u and ε_u are the ultimate tensile true stress and strain of a given constitutive relation and w is a weight constant ($0 \leq w \leq 1$). Considering the two extremes, $w = 0$ yields the pure power law extrapolation, whereas $w = 1$ yields the pure linear extrapolation. The two extremes, as well as a compromise between the two, at $w = 0.5$, were tested using the uniaxial tension simulation, the engineering stress-strain results of which are shown in Figure 4.2.

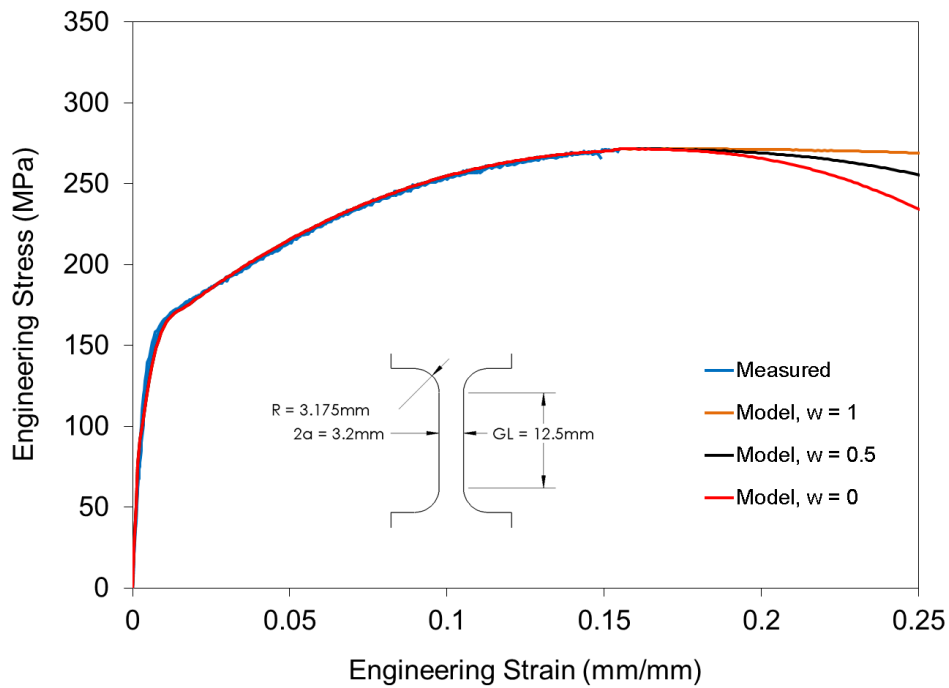


Figure 4.2 – Selected uniaxial tension results compared with proposed model curves demonstrating the sensitivity of the Ling parameter

The candidate curves begin to diverge from each other once an engineering strain of approximately 20% has been reached. Now, since there exists no post-necking engineering stress-strain behaviour from the experimental data in Chapter 3, the middle ground $w = 0.5$ was adopted as the weight constant to use for all models.

A smoothly ramping-up velocity load curve was applied to the plane of nodes located at one end of the specimen. By consequence, the plane of nodes opposite to the velocity load curve plane was fully constrained. Also, a half-symmetry model sectioned on the length-thickness plane (XY, referring back to Figure 4.1) was adopted to reduce the computational time with appropriate boundary conditions applied to the symmetry face. The peak velocity was set at 125 mm/s, which corresponds to a strain rate of 10 s^{-1} . This time scaling was done because there was no strain rate dependency included in this material model, and so a greater velocity will reduce computational time.

In post-processing, the evolution of $\overline{\varepsilon^p}$ and stress triaxiality was obtained by averaging the evolution curves of two or four elements (depending on what number was symmetrical) in the direct vicinity of the desired location: either the centre or the notch root. Nominal strain was calculated by tracking the length dimension extension between two centre-straddling nodes located on one of the two free surface faces. The extension was not measured at centre-thickness in order to be comparable to the nominal strains recorded during the experiments using DIC. The gauge length was the same as that used in the experiments: 12.5 mm for the uniaxial geometry, 12.8 mm for the $a/R=0.25$ notched geometry, and 3.2 mm for the $a/R=1$ notched geometry.

4.3 Mesh Convergence Study

The mesh convergence study was based wholly on the uniaxial tension tests. The optimal element size found was then used in the other three simulations as well: $a/R=0.25$ tension, $a/R=1$ tension, and biaxial hemispherical dome. For greater simplicity, only hexagonal elements were examined (with dimensions that were as close to cubic as was geometrically possible for the other three simulations). Four element sizes were proposed: 0.5 mm, 0.3 mm, 0.2 mm, and 0.1 mm. Now, the optimal element size was decided upon by tracking what $\overline{\varepsilon^p}$ levels were reached at the geometric centre of each proposed element size's model (see Figure 4.3).

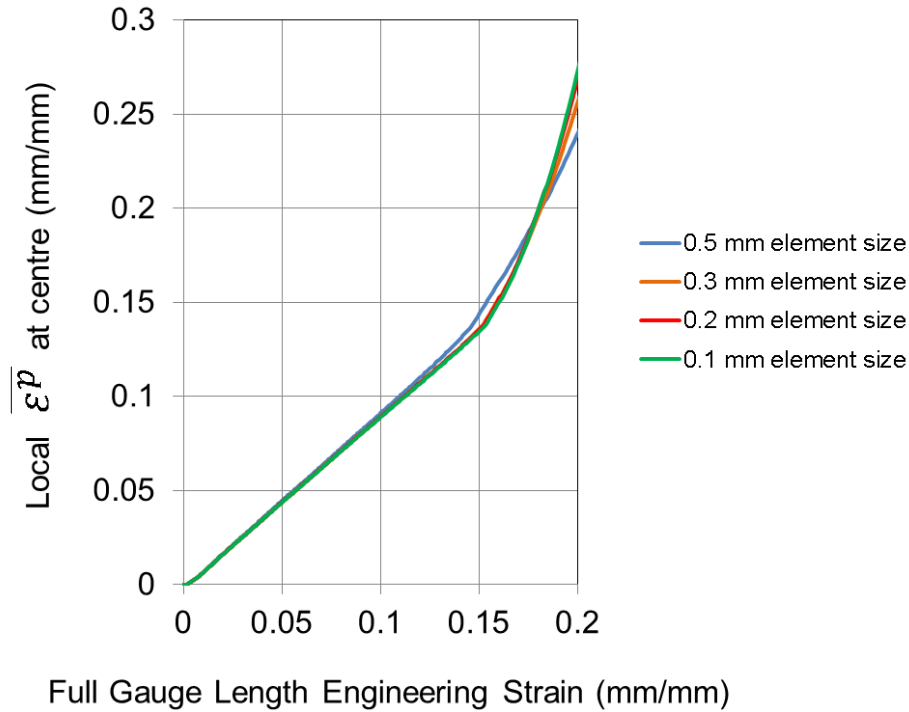


Figure 4.3 – Using the maximum $\overline{\epsilon^P}$ reached at the centre of the specimen as the optimization standard for the uniaxial tension mesh convergence study

The above curves diverge indefinitely after the specimen begins to neck at around 17% full gauge length engineering strain. From the uniaxial tension experiments, the maximum full gauge length engineering strain observed was 19.1%. It would therefore be reasonable to expect that an optimized mesh would yield a reasonably converged local $\overline{\epsilon^P}$ at centre after accruing this amount of full gauge length strain. Figure 4.4 plots what the level of $\overline{\epsilon^P}$ found at the centre would be for the four investigated element sizes. It also includes the amount of computational time that was required to produce each simulation.

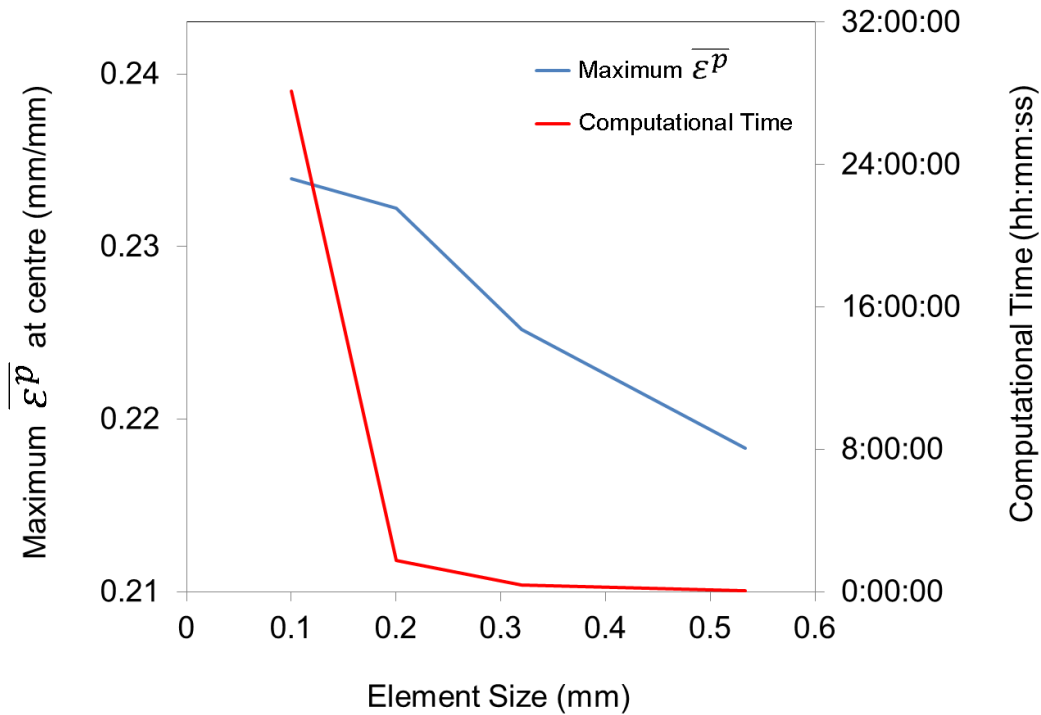


Figure 4.4 – Converging towards the true $\bar{\epsilon}^p$ level found at the geometric centre of the maximum elongation to failure experimental test, along with the computational time that was required in order to obtain it

Examining the preceding figure in an incremental fashion, there is a 3.2% increase in the $\bar{\epsilon}^p$ at centre when refining the element size from 0.5 mm to 0.3 mm. For the 0.3 mm to 0.2 mm increment, there is another 3.1% increase. However, when refining the element size from 0.2 mm to 0.1 mm, there is only a 0.7% increase in $\bar{\epsilon}^p$ at the centre. Based on this, an element size of 0.1 mm or 0.2 mm would be reasonable to choose, as the 0.7% difference indicates the value is adequately converged. When bringing in the consideration for computational time, an additional 26 hours of computational time would be required to glean this additional 0.7% of $\bar{\epsilon}^p$ convergence. It was decided that although it is indeed a significant incremental cost in computational time, the 0.1 mm element size standard was chosen.

4.4 Biaxial Hemispherical Dome Test Model

The biaxial hemispherical dome test is a fundamentally different test than that seen with the mini-dogbone tensile tests. One way this is true is that this test makes use of much larger

samples. To be confident that the same gradient discretizations may be studied in terms of stress triaxiality and $\overline{\varepsilon}^p$ evolution, it is important to maintain the same element size, at least in the vicinity of the of expected failure. This requirement led to the usage of transition elements for the mesh of the blank. Referring to Figure 4.5, at the centre of the samples there was a 1x1x2.8 mm volume of 0.1 mm size cubic elements. Moving away from the centre, in order to reduce the number of elements, transition elements (on the x-y plane only) were used. The mesh size needed to be moderately fine at the midway length. This is because overly coarse elements were not folding over the lip on the die smoothly enough, creating zones of artificially elevated stress. Using transition elements allowed the blank to be made up of 86,240 solid elements, instead of the 12,667,200 that would have been necessary if using the 0.1 mm element size throughout the blank.

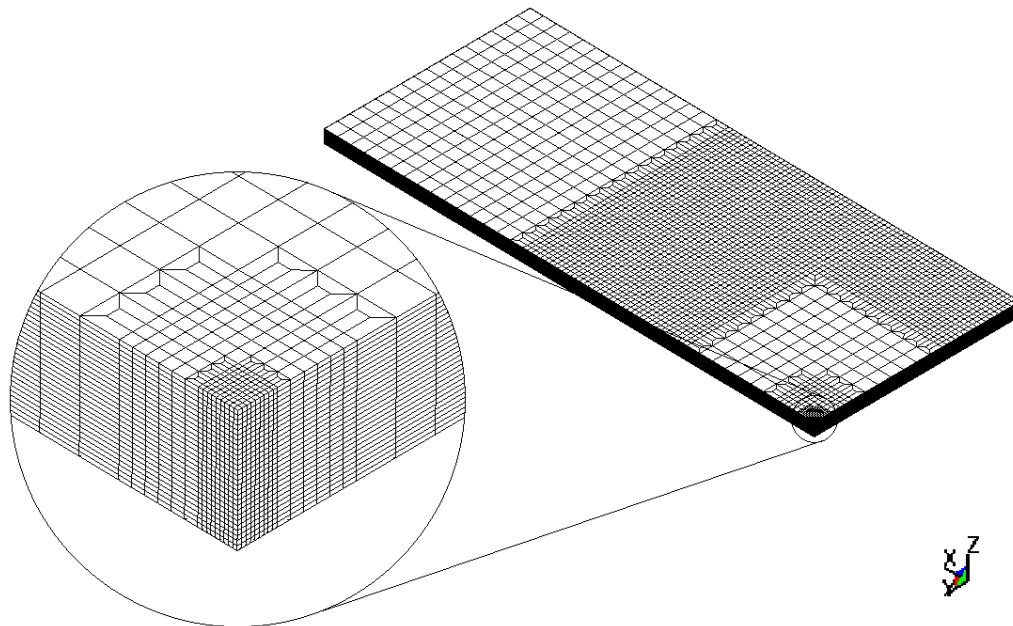


Figure 4.5 – A detailed view of the mesh of the blank, which included transition elements on the x-y plane

The tooling (die, binder, and punch) was modelled using a rigid material model assumption which is computationally less expensive. The thickness of the AM60B blank was 2.8 mm, and the material model definition included the following generally accepted mechanical properties: Density = 1.8 g/cc, Young's Modulus = 45 GPa, and Poisson's Ratio = 0.35 [57]. Quarter

symmetry conditions were enforced in order to reduce computational cost. Regarding the contact definition between the punch and the blank, the static and dynamic friction coefficients were both chosen to be 0.06. This figure was an estimate that lies in the range of the static friction coefficients of lubricated magnesium (0.08) and lubricated PTFE film (0.04) [58]. The closing of the binder over the die was done using a force profile that translated the binder and closed itself against the blank and die with minimized impact. The force that introduced minimal vibrational modes into the blank upon impact was found to be 800 N. Now with contact established, a steeply ramping clamping force profile was executed, with a final magnitude of 125 kN (or 500 kN for an entire blank without quarter symmetry). The punch was then accelerated using a smooth sinusoidal function up until the desired speed of 0.25 mm/s.

There was no time or mass scaling adopted in this simulation. As a result, the computational time was 8:12:08:44 [d:hh:mm:ss]. The number of elements used is listed in Table 4.2.

Part	Number of Elements
Punch	125,274
Binder	782
Die	1,242
Blank	86,240
Total	213,538

Table 4.2 – Number of elements used in the biaxial hemispherical dome test model, as seen in Figure 4.6

The mesh resolution of the punch (see Figure 4.6) could have been coarser, but it would have necessitated the use of transition elements. This was not deemed compulsory, since the computational penalty was small.

In post-processing, the evolution of $\overline{\varepsilon^p}$ and stress triaxiality was obtained by averaging the evolution curves of four free surface elements that were located at the geometric centre of the

blank. Major and minor strains were obtained by plotting logarithmic strain histories of the node at the geometric centre of the model.

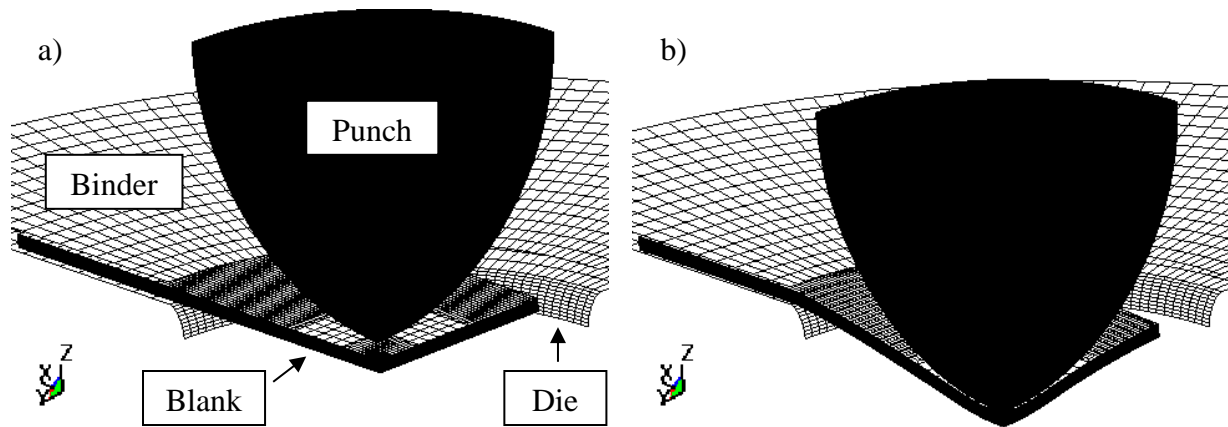


Figure 4.6 – The four parts and their relative arrangements in the biaxial hemispherical dome test model, a) undeformed state, b) deformed state (15 mm displacement)

Due to the Phase II tests displaying porosity issues as documented in the previous chapter, a constitutive model predicting the response of the various Phase II sample geometries was not sought after, choosing instead to validate the simulations using solely Phase I results. In the upcoming results, if the sample origin is not specified, the Phase I experimental results were used.

5 NUMERICAL RESULTS

In this chapter, predictions using the uniaxial and notched tensile and biaxial finite element models are presented. This is followed up by an investigation into how $\overline{\varepsilon}^p$ is predicted to evolve for the various stress states that are produced.

5.1 Numerical Tensile Model Results

The numerically predicted stress-strain curves (symbols) are shown in Figure 5.1 along with their measured counterparts (solid lines). The simulations were halted at nominal strains of 19%, 5%, and 8%, for the uniaxial, a/R=0.25, and a/R=1 sample geometries, respectively, as these were the maximum measured elongations to failure.

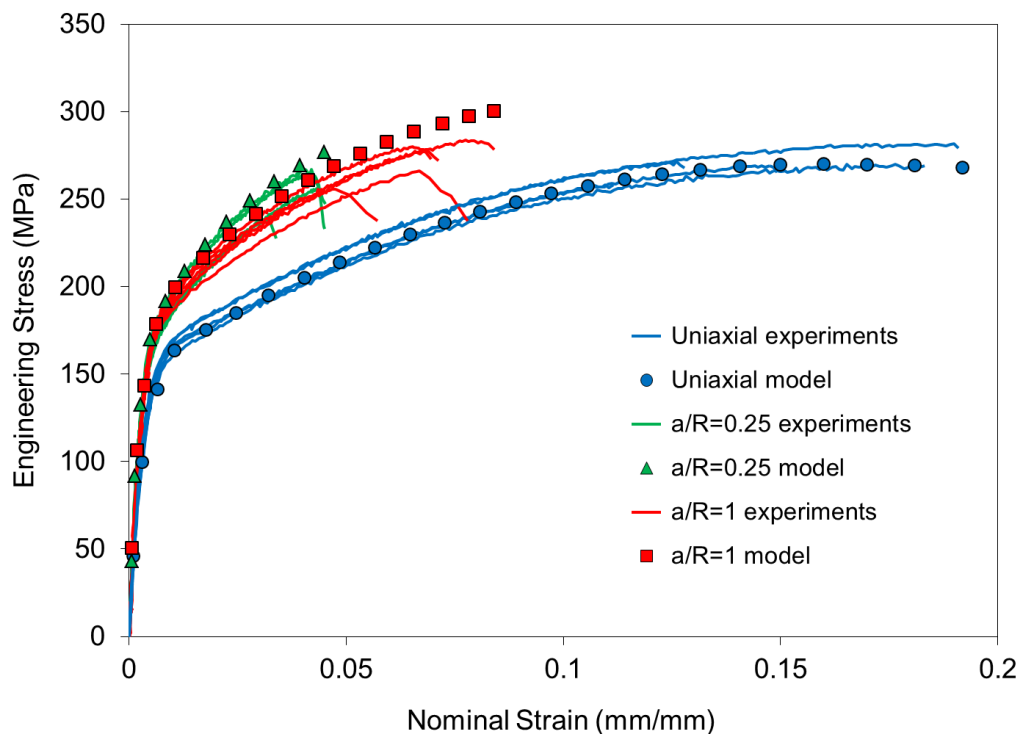


Figure 5.1 – Comparing model predicted engineering stress-nominal strain response to measured results

The predictions are in good agreement with the measured data, particularly for the uniaxial geometry. For the notched cases, the model slightly over predicts the stress levels beyond the yield point; this may be due to an overestimation of flow stress. This trend was also noted by Chen et al. in their comparison of the accuracy of a material model that included damage parameters to one that did not [29]. Overall, the model is seen to capture the effect of notch geometry on engineering stress-nominal strain response reasonably well.

Figure 5.2 examines the first principal logarithmic strain fringes for both the measured results (left half) and the model predicted results (right half). A notched $a/R=0.25$ sample is shown at a nominal strain of 4.0%.

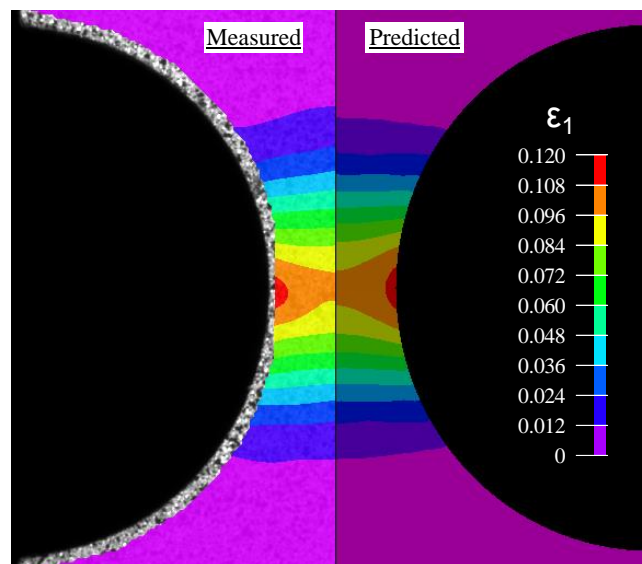


Figure 5.2 – Comparison of measured results (left) to model predicted results (right) for an $a/R=0.25$ sample, at a nominal strain of 4.0%

The maximum strain is found at the edge of the sample, the “notch root,” and not at the centre of the gauge area, the region of highest stress triaxiality. Good correspondence is observed between the predicted and measured strain which, along with the reasonable engineering stress-nominal strain predictions, provides support for the model validation.

The accuracy of the notched sample geometry models may also be assessed by tracking the expansion of the gauge length and plotting it against the contraction of the gauge width, as the sample deforms. The experimental data used is obtained from a single test that showed a median elongation to failure. Figure 5.3 shows the results of this analysis for the $a/R=0.25$ sample geometry, and Figure 5.4 shows the results for the $a/R=1$ sample geometry.

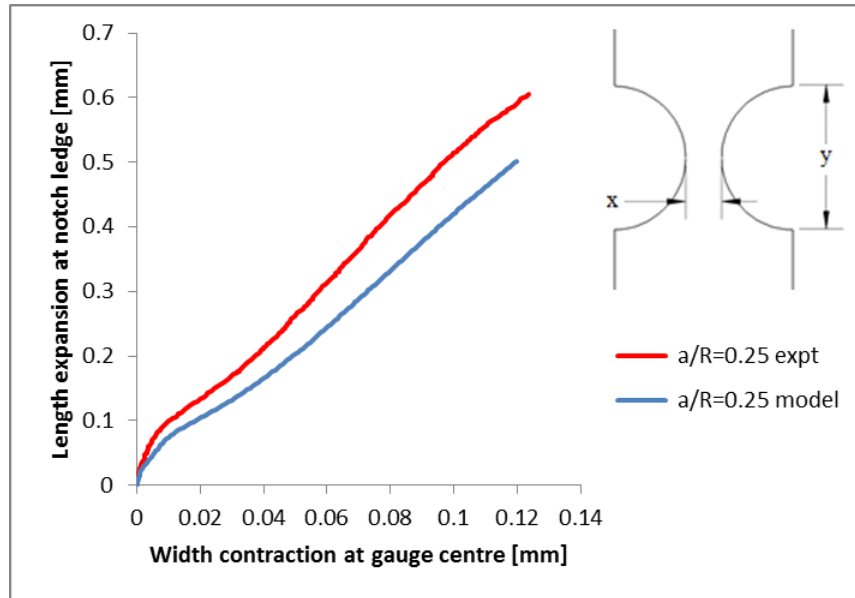


Figure 5.3 – Gauge length expansion versus width contraction for the $a/R=0.25$ geometry

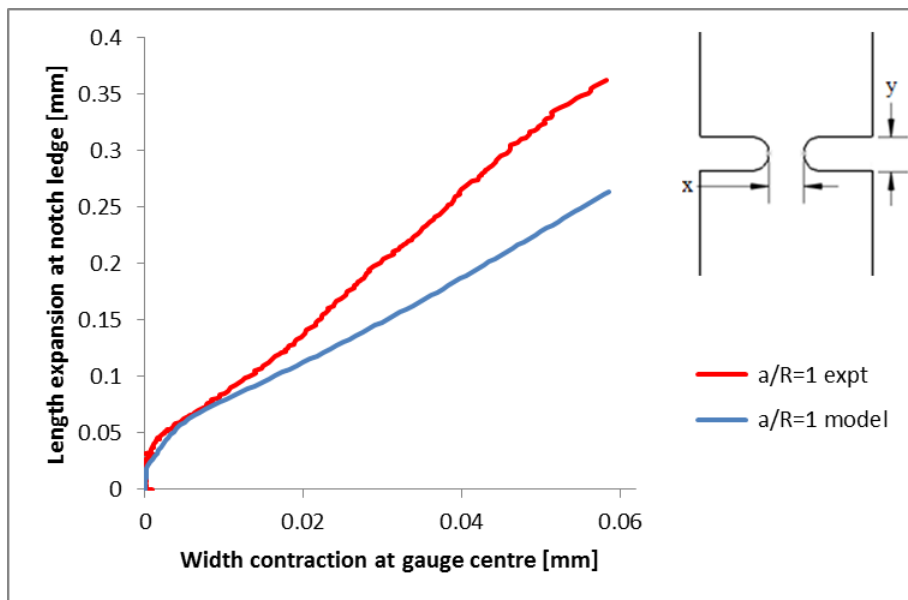


Figure 5.4 – Gauge length expansion versus width contraction for the $a/R=1$ geometry

The $a/R=0.25$ results suggest that the length expansion and width contraction evolve similarly for both experiment and model. The agreement between model and experiments is not as good for the $a/R=1$ results, with the model overpredicting the contraction for a given level of extension.

5.2 Numerical Biaxial Hemispherical Dome Model Results

The numerically predicted behaviour of the near biaxial hemispherical dome test is presented with the experimental results in Figure 5.5.

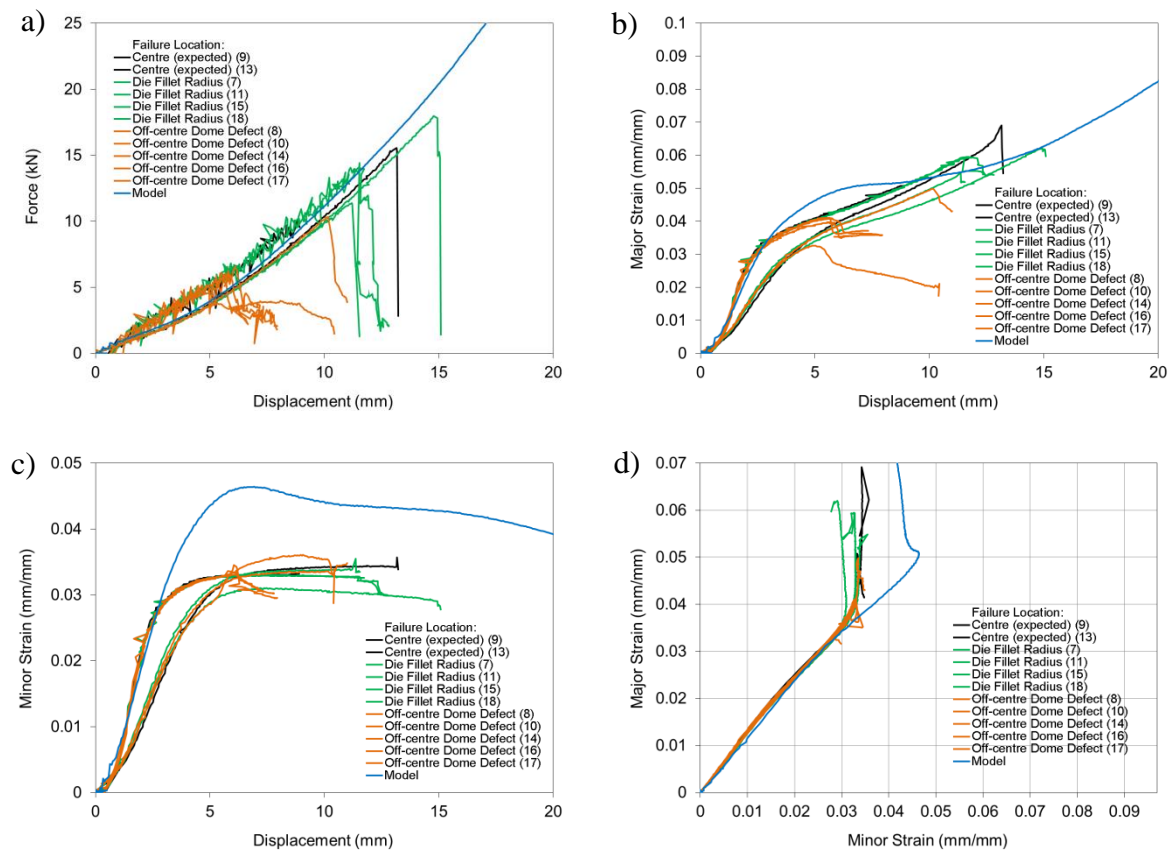


Figure 5.5 – Comparing model predictions to measured biaxial hemispherical dome data, a) force vs. displacement, b) major strain vs. displacement, c) minor strain vs. displacement, d) major strain vs. minor strain

The model shows good agreement with the measured force-displacement profile, as seen in Figure 5.5a. Regarding Figure 5.5b, the model shows an unexpected increase in major strain

peaking at around the 6 mm displacement mark. It also appears to agree more closely with the second batch of measurements, providing a near exact prediction up until a displacement of 3.0 mm. The minor strain predictions, as seen in Figure 5.5c and d, agree initially with one of the groups of experimental data. However, the minor strain increases monotonically beyond the point at which the minor strain rate approaches zero (measured curves flatten). This error may be due to differences between the assumed friction coefficient and that operative in the experiments.

Figure 5.6 serves to examine the first principal logarithmic strain contours for both the predicted (top-right quadrant) and measured results. The sample shown is one of the two that failed at the centre. These images correspond to a punch displacement of 12.4 mm; failure initiated after 13.2 mm displacement. This comparison shows reasonable agreement, particularly in the major direction which demonstrates that the model is behaving adequately.

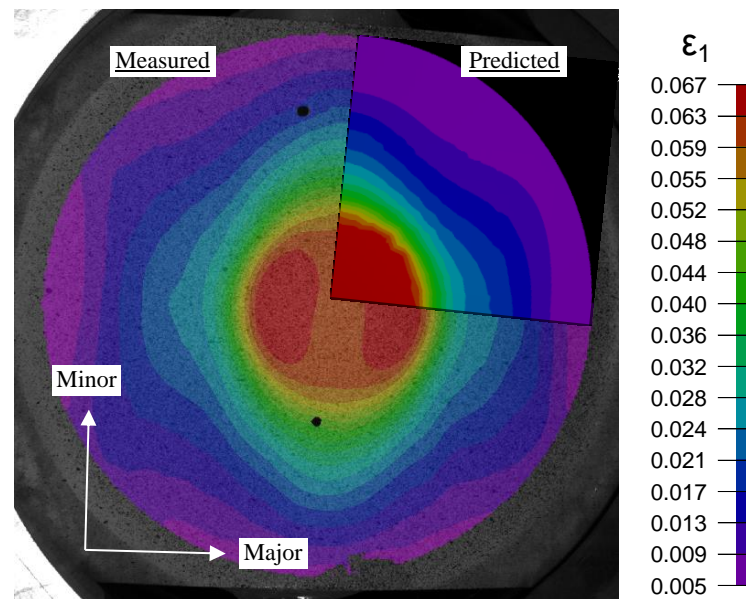


Figure 5.6 – Comparison of predicted first principal strain contours (top-right quadrant) to measured results for a biaxial hemispherical dome test sample just prior to failure

A significant amount of strain (and stress in the model) was always seen to build up at the location where the edge of the sample meets the die fillet radius. For example, Figure 5.7

shows the von Mises stress contours that are predicted to exist after the punch has displaced the blank by 13.9 mm.

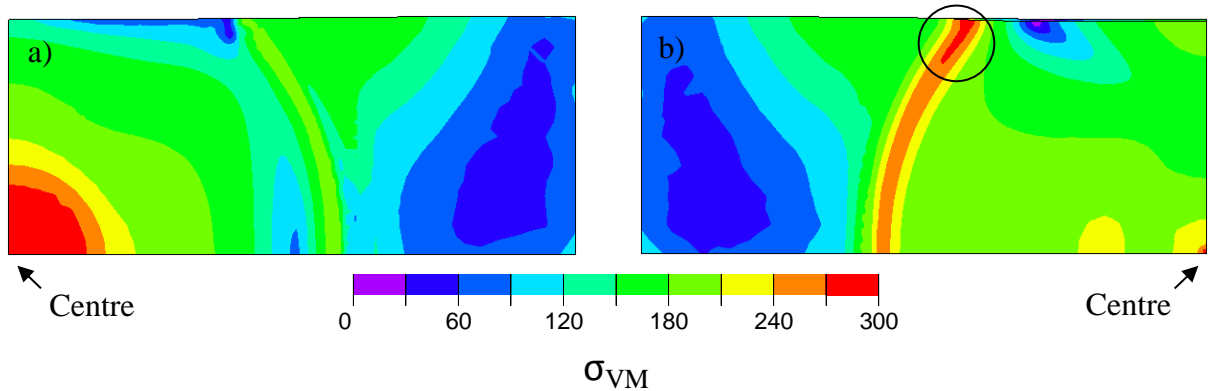


Figure 5.7 – Von Mises stress contour plots of the biaxial hemispherical dome test, after the punch has displaced the blank by 13.9 mm, a) top/DIC camera facing surface view, b) bottom/punch contacting surface view

Strain concentration occurs (circled in Figure 5.7b) at the location where the edge of the sample meets the die fillet radius. In fact, at 13.9 mm punch displacement, the stress levels at these locations become slightly greater than that of the centre, as shown in Figure 5.8.

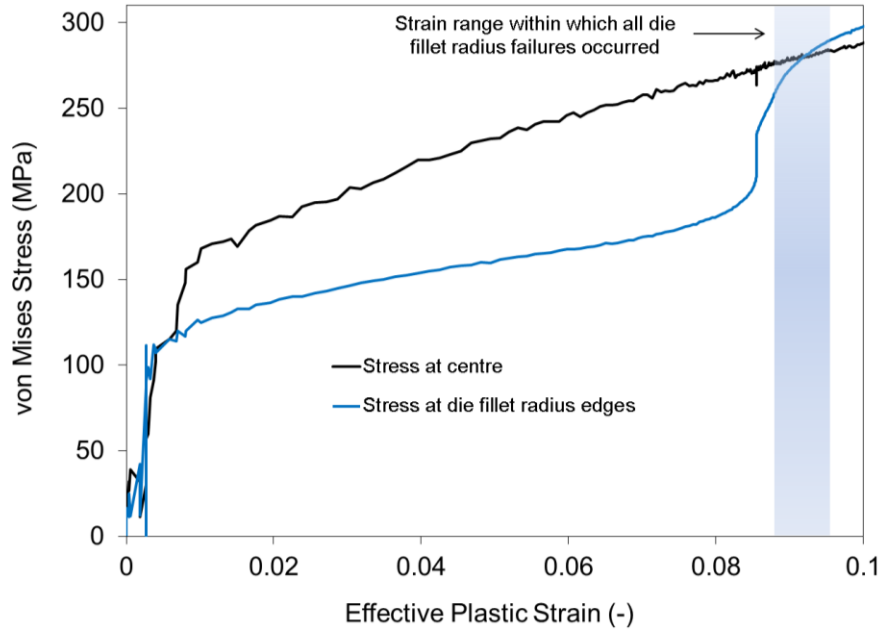


Figure 5.8 – Von Mises stress history at two distinct points on the specimen: the centre and the edge where the sample comes into contact with the die fillet radius

The maximum width of material extractable from the casting was too narrow to perform a purely biaxial test with the tooling on-hand. Therefore, the test created stress intensification sites that may have caused four of the eleven tested samples to prematurely fail at the die fillet radius instead of at the centre.

DIC is only able to measure surface strains, so now that there is confidence in the finite element models, exploration of the evolution of mechanical properties inside the specimens may commence.

5.3 Stress Triaxiality and Failure Strain Trends

To study the trends in measured failure strain and stress triaxiality as predicted by the finite element models, a plot showing the evolution of $\overline{\varepsilon^p}$ as a function of stress triaxiality is created (see Figure 5.9). For the tensile models, the evolution is plotted both at the centre of the sample and at the “notch root,” which is taken as the root of the neck (being located at centre-thickness). Each symbol represents the $\overline{\varepsilon^p}$ reached before failure of an individual experimental

test. The experiments denoted by the circles, squares, and diamonds made use of the 2.0 mm thick tensile models and the experiments denoted by the crosses made use of the 2.8 mm thick biaxial model. The magnitude of variation is quantified statistically by the use of a solid black trend line, passing through the mean $\bar{\epsilon}^p$ at failure of each dataset. In addition, the spread of the data is represented by two black dashed lines that represent one standard deviation above and below the mean. As the data shows, there is considerable variation in $\bar{\epsilon}^p$ and stress triaxiality at failure due to the variations in the measured elongation to failure.

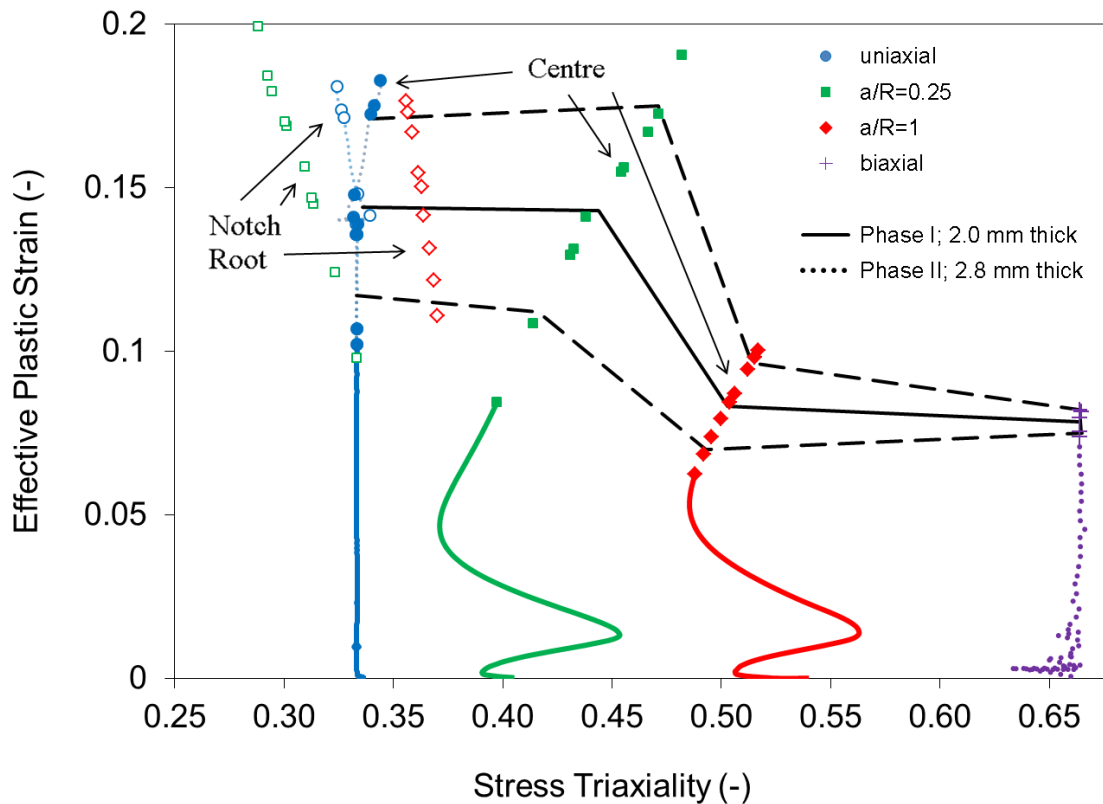


Figure 5.9 – $\bar{\epsilon}^p$ histories at the centre and notch root on the specimen for the four geometries under study

The failure conditions in the model and experiment were correlated based upon the equivalent strain at the location of failure in the experiments. The failure initiation point in each individual test was found to always be at the notch root instead of the centre. The measured major and minor strains accrued at the failure initiation point just prior to fracture were extracted from the

DIC data. These strains were then used to calculate the equivalent strain at failure, ε_{eq} , using the equation

$$\varepsilon_{eq} = \frac{2\sqrt{3}}{3} \cdot \sqrt{\varepsilon_1\varepsilon_2 + \varepsilon_1^2 + \varepsilon_2^2}. \quad (19)$$

The average and standard deviation of the measured equivalent strain at failure is listed in Table 5.1 for each specimen geometry. The simulation time when the equivalent strain of the model at the failure initiation point equals that reached in each individual test is noted as that test's failure time. The corresponding predicted $\overline{\varepsilon^p}$ and stress triaxiality levels reached at the geometric centre and notch root of each sample at failure are then extracted from the models (also listed in Table 5.1).

The uniaxial simulation displays similar $\overline{\varepsilon^p}$ evolution at both the centre and the notch root of the specimen until a $\overline{\varepsilon^p}$ of 14.3% is reached. It is at this point that localization begins in the simulation resulting in the onset of necking and an increase in stress triaxiality at the centre of the specimen. This behaviour contrasts that of the two notched tensile geometries for which stress triaxiality is greater at the centre than at the notch root for the entire deformation process. The stress triaxiality for all tensile geometries at the notch root location remains close to 0.33 (uniaxial) since this is a free surface. As for the evolution of $\overline{\varepsilon^p}$, the two notched tensile geometries showed similar trends, but at differing levels. If it is assumed that samples fail at the centre, then the effective plastic strains at failure show a decreasing trend with stress triaxiality. If failure initiates at the notch surface, it is due to a high strain concentration present there. If this is the case, the failure strain corresponding to the high stress triaxiality levels was not reached, thus the trend lines with respect to stress triaxiality plotted in Figure 5.9 are likely lower bounds. The predicted stress triaxiality and $\overline{\varepsilon^p}$ at failure corresponding to the average effective strain at failure are summarized in Table 5.1.

Sample Geometry	Average Measured Equivalent Strain at Failure	Crack Location	Stress Triaxiality at Failure	$\overline{\varepsilon^p}$ at Failure
Uniaxial	17.3±4.0%	Centre	0.34	14.4±2.7%
		Notch Root	0.33	14.3±2.6%
a/R=0.25	16.4±3.0%	Centre	0.44	14.3±3.2%
		Notch Root	0.31	15.7±3.0%
a/R=1	13.5±2.2%	Centre	0.50	8.3±1.3%
		Notch Root	0.36	14.7±2.3%

Table 5.1 – Average equivalent strain, stress triaxiality, and $\overline{\varepsilon^p}$ at failure for each of the three tensile geometries

6 DISCUSSION, CONCLUSIONS, AND FUTURE WORK

6.1 Discussion

The sample geometry chosen for this material may not have been optimized. Additional refinements, such as increasing the gauge width, may promote failure at the centre of the geometry. The crack initiation location should also be visually captured during each test; high speed imagery may be incorporated to fulfill this objective in the future.

Analysis of the DIC images of the notch specimens clearly showed the initial crack formed at the notch surface. A series of pictures is shown in Figure 6.1 for an $a/R=0.25$ notched sample recorded at four frames per second. In the first frame (“Before”), there is no visible crack. In the second frame (“During”), a crack, as demarcated by an arrow, initiates at the left edge of the sample. Note that because sandblasting was used here instead of a base coat of white paint in the speckling process, it is reassuring that it is in fact the sample that has formed the crack. In the third and final frame (“After”), the crack has propagated through the entire width of the sample, and fracture has been achieved.

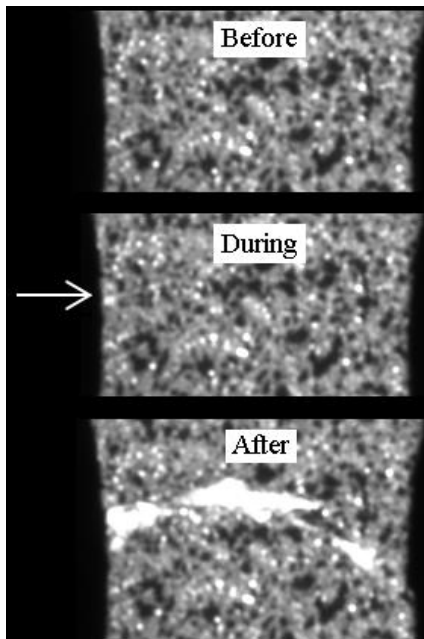


Figure 6.1 – DIC image showing crack initiation beginning from the left notch root on an $a/R=0.25$ sample (elongation to failure = 4.2%)

The failure sequence was captured for only a minority of the total number of tests due to frame rate limitations. However, there was at least one sequence similar to Figure 6.1 witnessed for each of the tensile sample geometries tested. In addition, analysis of the DIC data showed that the maximum strain always occurred at the notch root. Therefore, it is likely that failure initiates at the notch root for all tests. Failure location is important to assess, since the stress triaxiality levels created would vary considerably (recall Figure 5.9).

6.2 Conclusions

The constitutive behaviour of super vacuum die cast AM60B was shown to be sensitive to changes in stress triaxiality. As the initial stress triaxiality increased, the maximum stress increased and the overall ductility decreased.

The constitutive behaviour of 0° samples as compared to 90° ones suggests that there is little to no in-plane anisotropy present in the AM60B castings examined in the current work. The measured r-values ranged from 1.0 to 1.1, which indicates that a mild degree of transverse anisotropy is present.

All samples tested show minimal necking, evidenced by the lack of softening and sudden failure once the ultimate stress is reached. This was explored by Considère's approach, which showed that most uniaxial samples did not achieve sufficient elongation to begin the necking process.

Mild but positive strain rate sensitivity was found in AM60B: at an elevated strain rate of 10 s^{-1} , the maximum stress was 4-8% greater than at 0.001 s^{-1} . Also, for the notched tensile samples, the work hardening rate was shown to increase at the elevated strain rate.

The measured and predicted strain fringe plots, as well as the crack location at failure, suggest that failure of the three tensile geometries under study begins at the notch root. They also accrue on average 14-16% effective plastic strain before failing.

The levels of porosity found in the cast components were large and negatively affected the material's performance. This is particularly clear when transitioning from the Phase I to Phase II datasets and seeing a marked decrease in ductility. This decrease is attributed to differences in porosity: 1.4% porosity was measured in a Phase I sample whereas the Phase II samples showed banded regions of very high porosity.

6.3 Future Work

Cast AM60B appears to reach its ultimate tensile stress, then promptly fail, exhibiting little or no necking. In future work, a more precise analysis regarding the extent of necking may be carried out by using optical techniques to determine true failure strains based on area reduction.

The number of test parameters examinable was limited by the relative unavailability of low porosity castings. Validation of the Phase I findings and then new tests at a wider variety of strain rates and stress states (shear, compressive) would be recommended once new lots of material are available. Also, since the component under investigation is a casting, there is some inherent microstructural variation to consider. One way this affects the present results is the precision at which each geometry's stress triaxiality and $\overline{\epsilon^p}$ at failure may be reported. For example, referring back to Figure 5.9 and considering the $a/R=0.25$ geometry, final stress triaxiality was found to lie within a range of 0.40-0.48 and $\overline{\epsilon^p}$ to failure within a range of 8.4-19.0%. Further testing should be planned to assess the local and part-to-part variation of the casting.

The numerical model requires additional assessment, as it was determined, for example, that the $a/R=1$ simulation predicts lower levels of length elongation at a given level of width contraction. This should begin to be addressed by adapting the failure points for use in obtaining fitting parameters in damage-based material models, to be able to predict when failure occurs in gauge regions of a wider assortment of geometries/stress states. The model should also incorporate rate dependence.

REFERENCES

- 1 Luo, A., "Magnesium: Current and Potential Automotive Applications". *JOM*, 54:42-48, 2002.
- 2 McDonough, W.F., "Earthquake Thermodynamics and Phase Transformations in the Earth's Interior," Academic Press, Waltham, MA, 2000.
- 3 No author, "Commodity Prices." Available: <http://www.alibaba.com> [accessed January 13, 2014].
- 4 Altan, T., "Hot stamping boron-alloyed steels for automotive parts". *Stamping Journal*, 40-41, 2006.
- 5 Patel, H.A., Rashidi, N., Chen, D.L., Bhole, S.D. et al., "Cyclic deformation behavior of a super-vacuum die cast magnesium alloy". *Materials Science and Engineering A*, 546:72-81, 2012.
- 6 Magnesium-Elektron, Datasheet 475: AM60B Specifications, 2006.
- 7 Bhattacharya, B. and Niewczas, M., "Work-Hardening Behaviour of Mg Single Crystals Oriented for Basal Slip". *Philosophical Magazine*, 91:2227-2247, 2011.
- 8 Callister, W.D., "Materials Science and Engineering: An Introduction," John Wiley & Sons, Inc., New York, NY, 2007.
- 9 Akhtar, A. and Teghtsoonian, E., "Solid Solution Strengthening of Magnesium Single Crystals II - The Effect of Solute on the Ease of Prismatic Slip". *Acta Metallurgica*, 17:1351-1356, 1969.
- 10 Mordike, B.L. and Lukac, P., "Physical Metallurgy," Chapter 3 in *Magnesium Technology: Metallurgy, Design Data, Applications*, Springer, Berlin, Germany, 2006.
- 11 Avedesian, M.M. and Baker, H. (Eds.), "Magnesium and Magnesium Alloys," ASM International, Materials Park, OH, 1999.
- 12 Soboyejo, W., "Mechanical Properties of Engineered Materials," Marcel Dekker, Inc., New York, NY, 2003.
- 13 Dieter, G.E., "Mechanical Metallurgy," McGraw-Hill, Toronto, ON, 1961.

- 14 Mason, W.P., McSkimin, H.J., and Shockley, W., "Ultrasonic Observation of Twinning in Tin". *Physical Review*, 73:1213, 1948.
- 15 Roberts, C.S., "Magnesium and Its Alloys: The Deformation of Magnesium," John Wiley & Sons, Inc., New York, NY, 1960.
- 16 Wang, Y.N. and Huang, J.C., "The Role of Twinning and Untwinning in Yielding Behavior in Hot-Extruded Mg-Al-Zn Alloy". *Acta Materialia*, 55:897-905, 2007.
- 17 Gehrman, R., Frommert, M.M., and Gottstein, G., "Texture Effects on Plastic Deformation of Magnesium". *Materials Science and Engineering A*, 395:338-349, 2005.
- 18 Barnett, M.R., "Twinning and the ductility of magnesium alloys. Part I: "Tension" twins". *Materials Science and Engineering A*, 464:1-7, 2007.
- 19 Zeng, R.C., Han, E.H., Ke, W., and Dietzel, W., "Influence of Microstructure on Tensile Properties and Fatigue Crack Growth in Extruded Magnesium Alloy AM60". *International Journal of Fatigue*, 32:411-419, 2010.
- 20 University of Dayton Research Institute, "High Rate Tension and Compression Testing of AM30 Double Hat Extrusion and Vacuum Die Cast AM60B Magnesium," Technical Report UDR-TR-2009-63, Dayton, OH, May 2009.
- 21 Bouchard, P.O., Bourgeon, L., Fayolle, S., and Mocellin K., "An enhanced Lemaitre model formulation for materials processing damage computation". *International Journal of Forming Processes*, 4:299-315, 2011.
- 22 Haufe, A., Feucht, M., Neukamm, F., and DuBois, P., "Recent Enhancements to the GISSMO Failure Model in LS-DYNA," European LS-DYNA Conference, 2011.
- 23 Dunand, M. and Mohr, D., "Hybrid experimental-numerical analysis of basic ductile fracture experiments for sheet metals". *International Journal of Solids and Structures*, 47:1130-1143, 2010, doi:10.1016/j.ijsolstr.2009.12.011.
- 24 Johnson, G.R. and Cook, W.H., "Fracture Characteristics of Three Metals Subjected to Various Strains, Strain Rate, Temperatures and Pressures". *Eng. Fract. Mech.*, 21:31-48, 1985.
- 25 Hancock, J.W. and Mackenzie, A.C., "On the Mechanisms of Ductile Failure in High-Strength Steels Subjected to Multi-Axial Stress-States". *Journal of the Mechanics and*

- Physics of Solids*, 24:147-169, 1976.
- 26 Luo, M., "Ductile Fracture Characterization of an Aluminum Alloy Sheet using Numerical Simulations and Tests," Student Term Project Report, Impact and Crashworthiness Lab, Massachusetts Institute of Technology, 2008.
- 27 Yan, C., Ma, W., Burg, V., and Chen, M.W., "Experimental and Numerical Investigation on Ductile-Brittle Fracture Transition in a Magnesium Alloy". *J. Mater. Sci.*, 42:7702-7707, 2007.
- 28 Gu, G.Y., Lin, S.T., Meng, Y., Xia, Y. et al., "Influence of Strain Rate and Stress State on the Mechanical Behavior of Die-Casting AM60 Magnesium Alloy," IMECE2011 Technical Paper 65196, 2011.
- 29 Chen, X., Wu, S.R., Wagner, D.A., and Hu, W., "Study of Die Cast Magnesium Components for Crash Safety". *International Journal of Crashworthiness*, 7:429-440, 2002.
- 30 Zhu, F., Chou, C., Yang, K.H., Chen, X. et al., "Calibrating Material Parameters to Model the Thin-Walled Components Made of Die Cast AM60B Magnesium Alloy". *International Journal of Crashworthiness*, 17:540-552, 2012.
- 31 Weiler, J.P., Wood, J.T., Klassen, R.J., Maire, E. et al., "Relationship between Internal Porosity and Fracture Strength of Die-Cast Magnesium AM60B Alloy". *Materials Science and Engineering*, A(395):315-322, 2005.
- 32 Dahle, A.K., Sannes, S., St. John, D.H., and Westengen, H., "Formation of defect bands in high pressure die cast magnesium alloys". *Journal of Light Metals*, 99-103, 2001.
- 33 Thomas, B.G., "Metals Processing," Chapter 14 in *Structure, Processing, and Properties of Engineering Materials*, Addison Wesley, Boston, MA, 2000.
- 34 Balasundaram, A. and Gokhale, A.M., "Quantitative characterization of spatial arrangement of shrinkage and gas (air) pores in cast magnesium alloys". *Materials Characterization*, 46:419-426, 2001.
- 35 Chadha, G., Allison, J.E., and Jones, J.W., "The Role of Microstructure on Ductility of Die-Cast AM50 and AM60 Magnesium Alloys". *Metallurgical and Materials Transactions A*, 38A:286-297, 2007.
- 36 Sannes, S., Gjestland, H., Westengen, H., Laukli, H. et al., "Die Casting of Magnesium

- Alloys - The Importance of Controlling Die Filling and Solidification," Proceedings SAE 2003, SAE Paper No. 2003-01-0183, Detroit, MI, 2003.
- 37 Dorum, C., Hopperstad, O.S., Berstad, T., and Dispinar, D., "Numerical Modelling of Magnesium Die-Castings using Stochastic Fracture Parameters". *Engineering Fracture Mechanics*, 76:2232-2248, 2009.
- 38 Smerd, R., Winkler, S., Salisbury, C., Worswick, M. et al., "High Strain Rate Tensile Testing of Automotive Aluminum Alloy Sheet". *International Journal of Impact Engineering*, 32:541-560, 2005.
- 39 ASTM International, "Annual Book of ASTM Standards: Metals - Mechanical Testing, Elevated and Low Temperature Tests, Metallography," West Conshohocken, PA, 2003.
- 40 Bridgman, P.W., "Studies in Large Plastic Flow and Fracture," Harvard University Press, Cambridge, MA, 1964.
- 41 Boba, Mariusz. Warm Forming and Formability of Magnesium Alloys, MAsc. Thesis, Waterloo, ON: University of Waterloo; 2014.
- 42 *Vic-2D/Vic-3D*, [computer program]. Columbia, SC: Correlated Solutions, Inc.; 2009.
- 43 ASTM B557-14, Standard Test Methods for Tension Testing Wrought and Cast Aluminum- and Magnesium-Alloy Products, ASTM International, West Conshohocken, PA, 2014.
- 44 Bardelcik, A., Worswick, M.J., Winkler, S., and Wells, M.A., "A Strain Rate Sensitive Constitutive Model for Quenched Boron Steel with Tailored Properties". *International Journal of Impact Engineering*, 50:49-62, 2012.
- 45 Khan, S.A., Bhuiyan, M.S., Miyashita, Y., Mutoh, Y. et al., "Corrosion Fatigue Behavior of Die-Cast and Shot-Blasted AM60 Magnesium Alloy". *Materials Science and Engineering A*, 528:1961–1966, 2011.
- 46 Hijazi, A., Yardi, N., and Madhavan, V., "Determination of Forming Limit Curves using 3D Digital Image Correlation and In-Situ Observation," Proceedings SAMPE 2004, Long Beach, CA, 2004.
- 47 Hung, P.C. and Voloshin, A.S., "In-plane Strain Measurement by Digital Image Correlation". *J. of the Braz. Soc. of Mech. Sci. & Eng.*, 25:215-221, 2003.
- 48 Tung, S.H. and Sui, C.H., "Application of Digital-Image-Correlation Techniques in

- Analysing Cracked Cylindrical Pipes". *Sadhana*, 35:557-567, 2010.
- 49 Yong, H. and Li, R., "Effects of Silicon on Mechanical Properties of AM60 Magnesium Alloy," *China Foundry*, 9:244-247, 2012.
- 50 Moore, D.S. and McCabe, G.P., "Introduction to the Practice of Statistics," W.H. Freeman and Company, New York, NY, 2006.
- 51 Student, "The Probable Error of a Mean". *Biometrika*, 6:1-25, 1908.
- 52 Considère, A.G., "Mémoire sur l'emploi du fer et de l'acier dans les constructions". *Annales des Ponts et Chaussées*, 6:574-775, 1885.
- 53 Penner, P., MAsc Student, Centre for Advanced Materials Joining, University of Waterloo. Personal communication/E-mail. Waterloo, ON. May 28, 2013.
- 54 Dobrzanski, L.A., Maniara, R., and Sokolowski, J.H., "The Effect of Cooling Rate on Microstructure and Mechanical Properties of AC AlSi9Cu Alloy". *Archives of Materials Science and Engineering*, 28:105-112, 2007.
- 55 Hollomon, J.H., "Tensile Deformation". *Trans. AIME*, 162:268-290, 1945.
- 56 Ling, Y., "Uniaxial True Stress-Strain after Necking". *AMP Journal of Technology*, 5:37-48, 1996.
- 57 Bauccio, M.L., "ASM Engineered Materials Reference Book," ASM International, 1994.
- 58 Marshall, J.S. and Li, S., "Adhesive Particle Flow: A Discrete-Element Approach," Cambridge University Press, 2014.

APPENDIX A: SAMPLE CHARACTERISTICS

Top Hat ID	Sample ID	Location	Initial Gauge Width [mm]	Initial Gauge Thickness [mm]	Date Tested	Strain Rate [s ⁻¹]	
						Nominal	Actual
1	AC	Output Side	3.228	2.016	1/3/2013	0.001	0.00078
1	AD	Output Side	3.223	1.929	1/7/2013	0.001	0.00073
1	AH	Output Flange	3.165	1.725	6/13/2013	0.001	0.00080
1	AG	Input Flange	3.20	1.98	9/24/2012	10	7.0
1	AJ	Top	3.19	1.96	10/22/2012	10	7.7
2	AO	Output Side	3.195	1.908	1/3/2013	0.001	0.00075
2	AR	Input Flange	3.243	1.988	1/7/2013	0.001	0.00076
2	AS	Output Flange	3.192	1.717	6/13/2013	0.001	0.00077
2	AU	Top	3.183	1.976	1/7/2013	0.001	0.00072
2	AM	Input Side	3.2	2	9/12/2012	10	6.7
2	AN	Output Side	3.2	2	9/12/2012	10	7.0
3	A0	Top	3.208	1.943	6/11/2013	0.001	0.00080
3	A1	Top	3.215	1.946	6/11/2013	0.001	0.00078
3	A2	Top	3.217	1.930	6/11/2013	0.001	0.00080
3	A3	Top	3.280	1.938	6/11/2013	0.001	0.00077
3	A4	Top	3.196	1.957	6/13/2013	0.001	0.00079
3	A5	Top	3.276	1.942	6/13/2013	0.001	0.00076
3	A6	Top	3.207	1.956	6/13/2013	0.001	0.00078
3	A7	Top	3.213	1.953	6/13/2013	0.001	0.00078
3	A8	Top	3.211	1.944	6/13/2013	0.001	0.00079
3151-N/A	AA'	Top	3.206	2.812	2/28/2014	0.001	0.00072
3151-28	AB'	Top	3.209	2.782	2/28/2014	0.001	0.00072
3151-28	AC'	Top	3.207	2.773	2/28/2014	0.001	0.00073
3151-33	AD'	Top	3.208	2.801	2/28/2014	0.001	0.00074
3151-34	AE'	Top	3.206	2.811	2/28/2014	0.001	0.00074
3151-35	AF'	Top	3.208	2.79	2/28/2014	0.001	0.00075

Top Hat ID	Sample ID	Location	Initial Gauge Width [mm]	Initial Gauge Thickness [mm]	Date Tested	Strain Rate [s ⁻¹]	
						Nominal	Actual
1	BK	Top	3.222	2.039	1/3/2013	0.001	0.00079
1	BC	Top	3.2	2	9/7/2012	10	7.1
1	BD	Top	3.19	1.99	9/17/2012	10	7.4
1	BG	Top	3.20	1.95	10/22/2012	10	7.4
2	BL	Top	3.196	1.978	1/3/2013	0.001	0.00082
2	BM	Top	3.216	1.957	1/3/2013	0.001	0.00082
2	BN	Top	3.204	1.969	1/9/2013	0.001	0.00083
2	BO	Top	3.176	1.961	1/9/2013	0.001	0.00079
2	BP	Top	3.185	1.966	1/9/2013	0.001	0.00082
3151-N/A	BB'	Top	3.208	2.799	3/3/2014	0.001	0.00073
3151-N/A	BC'	Top	3.208	2.826	3/3/2014	0.001	0.00073
3151-23	BD'	Top	3.205	2.812	3/3/2014	0.001	0.00074
3151-23	BE'	Top	3.208	2.778	3/3/2014	0.001	0.00074
3151-23	BF'	Top	3.209	2.832	3/3/2014	0.001	0.00074

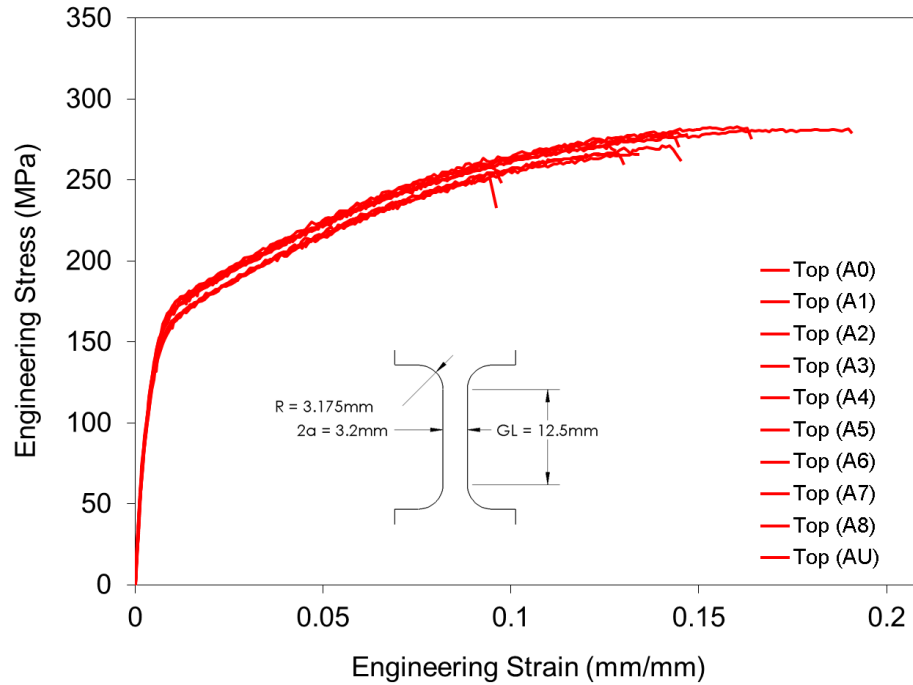
Top Hat ID	Sample ID	Location	Initial Gauge Width [mm]	Initial Gauge Thickness [mm]	Date Tested	Strain Rate [s ⁻¹]	
						Nominal	Actual
1	CB	Output Side	3.21	1.956	1/9/2013	0.001	0.00086
1	CE	Input Side	3.28	2.033	1/9/2013	0.001	0.00084
1	CG	Output Flange	3.28	1.781	1/9/2013	0.001	0.00088
1	CH	Input Flange	3.20	1.984	6/12/2013	0.001	0.00087
1	CJ	Top	3.22	1.991	6/12/2013	0.001	0.00088
1	CA	Output Side	3.30	2.016	11/12/2012	10	9.7
1	CC	Input Side	3.2	1.99	9/24/2012	10	6.9
1	CI	Top	3.2	1.95	9/24/2012	10	7.6
2	CN	Input Side	3.28	2.022	1/4/2013	0.001	0.00083
2	CO	Input Side	3.23	2.024	6/12/2013	0.001	0.00089
2	CS	Input Flange	3.17	1.986	6/12/2013	0.001	0.00088
2	CT	Top	3.28	2.011	1/4/2013	0.001	0.00088
2	CU	Top	3.21	1.977	6/12/2013	0.001	0.00086
2	CQ	Output Flange	3.2	1.78	9/24/2012	10	6.4
2	CY	Top	3.18	1.94	3/3/2014	0.001	0.00081
2	CZ	Top	3.22	1.94	3/3/2014	0.001	0.00083
3	C1	Top	3.25	1.965	6/11/2013	0.001	0.00089
3	C2	Top	3.20	1.942	6/11/2013	0.001	0.00089
3	C3	Top	3.18	1.938	6/11/2013	0.001	0.00082
3	C4	Top	3.21	1.947	6/11/2013	0.001	0.00088
3	C5	Top	3.22	1.938	6/11/2013	0.001	0.00088
3	C6	Top	3.18	1.942	6/11/2013	0.001	0.00086
3151-23	CA'	Top	3.16	2.793	2/28/2014	0.001	0.00072
3151-33	CC'	Top	3.19	2.81	2/27/2014	0.001	0.00064
3151-33	CD'	Top	3.2	2.797	2/28/2014	0.001	0.00079
3151-34	CE'	Top	3.21	2.804	2/28/2014	0.001	0.00080
3151-35	CF'	Top	3.21	2.796	2/28/2014	0.001	0.00063

Top Hat ID	Sample ID	Location	Initial Gauge Width [mm]	Initial Gauge Thickness [mm]	Date Tested	Strain Rate [s^{-1}]	
						Nominal	Actual
1	DB	Output Side	3.30	1.940	1/4/2013	0.001	0.0022
1	DF	Input Side	3.23	2.020	6/12/2013	0.001	0.0022
1	DG	Output Flange	3.31	1.709	1/4/2013	0.001	0.0024
1	DA	Output Side	3.28	1.974	11/12/2012	10	9
1	DD	Input Side	3.2	2.05	10/22/2012	10	16
1	DH	Input Flange	3.2	2.02	10/22/2012	10	15
1	DI	Top	3.2	2.01	10/5/2012	10	16
2	DL	Output Side	3.25	1.924	1/9/2013	0.001	0.0021
2	DO	Input Side	3.26	2.049	1/9/2013	0.001	0.0021
2	DP	Input Side	3.26	2.012	1/4/2013	0.001	0.0019
2	DS	Input Flange	3.24	1.996	6/12/2013	0.001	0.0021
2	DT	Top	3.29	2.006	1/9/2013	0.001	0.0022
2	DU	Top	3.23	1.947	6/12/2013	0.001	0.0022
2	DY	Top	3.20	1.967	3/3/2014	0.001	0.0020
2	DZ	Top	3.30	1.960	3/3/2014	0.001	0.0021
3	D1	Top	3.27	1.970	6/10/2013	0.001	0.0021
3	D2	Top	3.24	1.941	6/11/2013	0.001	0.0019
3	D3	Top	3.24	1.944	6/11/2013	0.001	0.0020
3	D4	Top	3.23	1.940	6/12/2013	0.001	0.0020
3	D6	Top	3.23	1.954	6/12/2013	0.001	0.0021
3151-28	DA'	Top	3.25	2.799	2/28/2014	0.001	0.0013
3151-33	DB'	Top	3.24	2.813	2/28/2014	0.001	0.0014
3151-34	DC'	Top	3.23	2.811	2/28/2014	0.001	0.0019
3151-34	DD'	Top	3.24	2.819	2/28/2014	0.001	0.0016
3151-35	DE'	Top	3.25	2.815	2/28/2014	0.001	0.0016
3151-53	DF'	Top	3.24	2.803	2/28/2014	0.001	0.0016

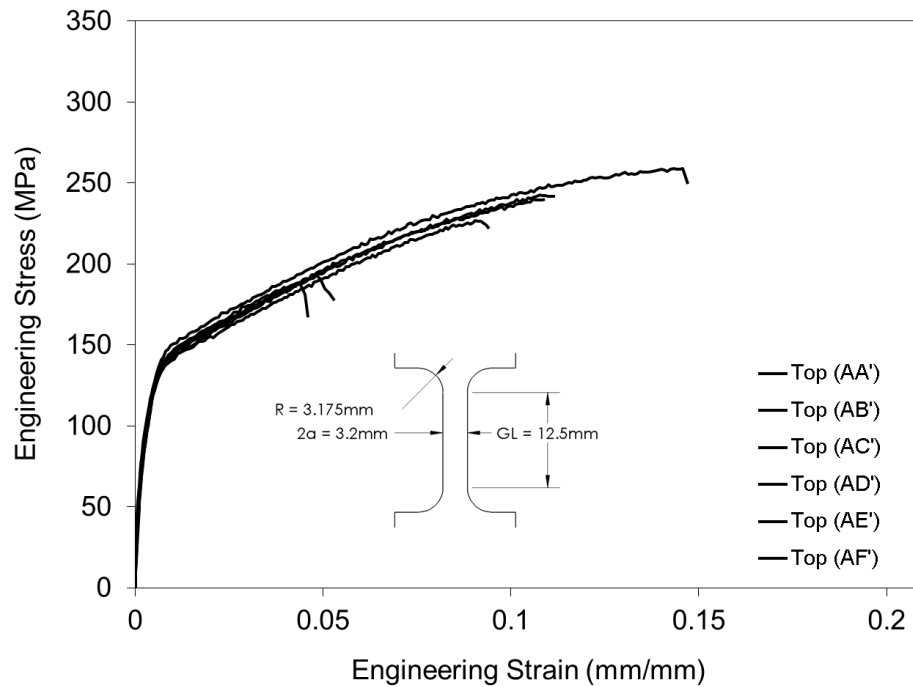
CanmetMATERIALS ID	Sample ID	Initial Length [mm]	Initial Width [mm]	Date Tested	Failure Initiation Location
3151-52	7	208	87	11/7/2013	top-right edge
3151-41	8	208	87	11/7/2013	mid-left surface crack
3151-27	9	208	87	11/15/2013	centre
3151-31	10	208	87	11/15/2013	mid-right surface crack
3151-60	11	208	87	11/15/2013	bottom-left edge
3151-N/A	13	208	86.5	5/27/2014	centre
3151-23	14	208	86.5	5/27/2014	mid-left surface crack
3151-33	15	208	86.5	5/27/2014	top-right edge
3151-35	16	208	86.5	5/27/2014	mid-right surface crack
3151-53	17	208	86.5	5/27/2014	mid-right surface crack
3151-54	18	208	86.5	5/27/2014	top-right edge

APPENDIX B: STRESS-STRAIN CURVES

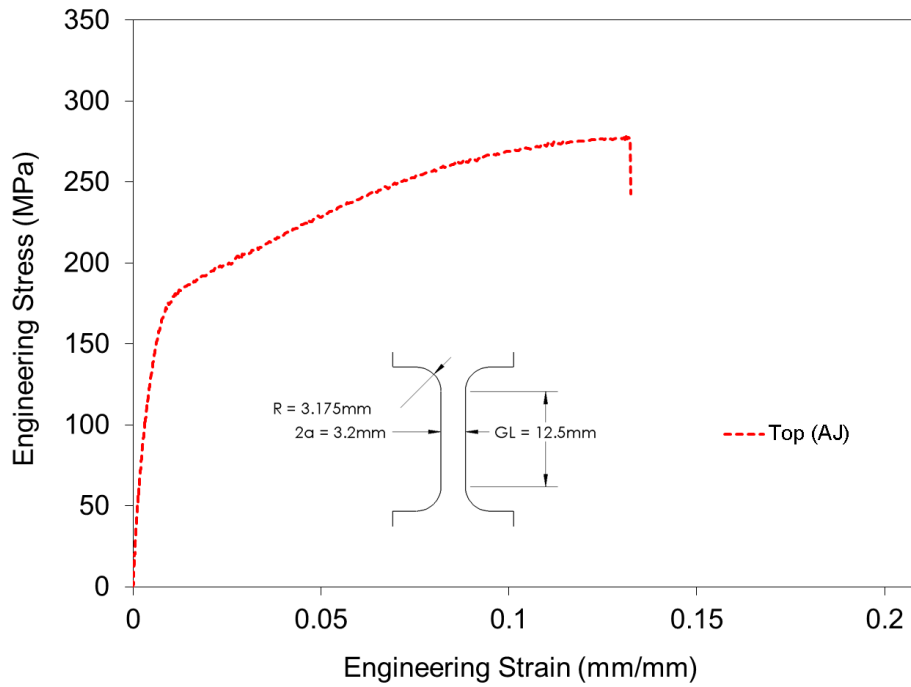
0° uniaxial, Phase I, top location, 0.001 s⁻¹



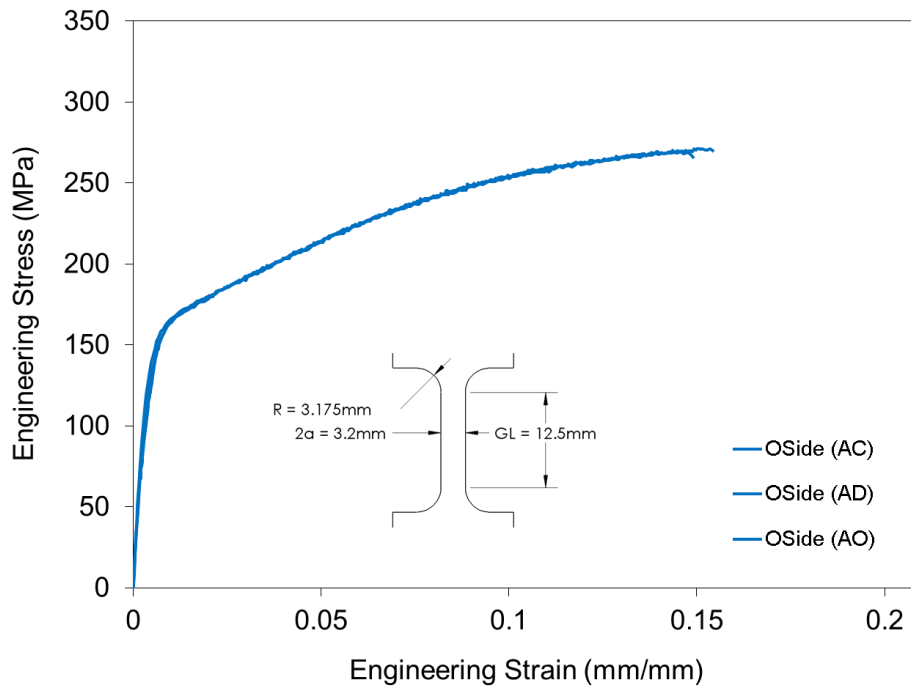
0° uniaxial, Phase II, top location, 0.001 s⁻¹

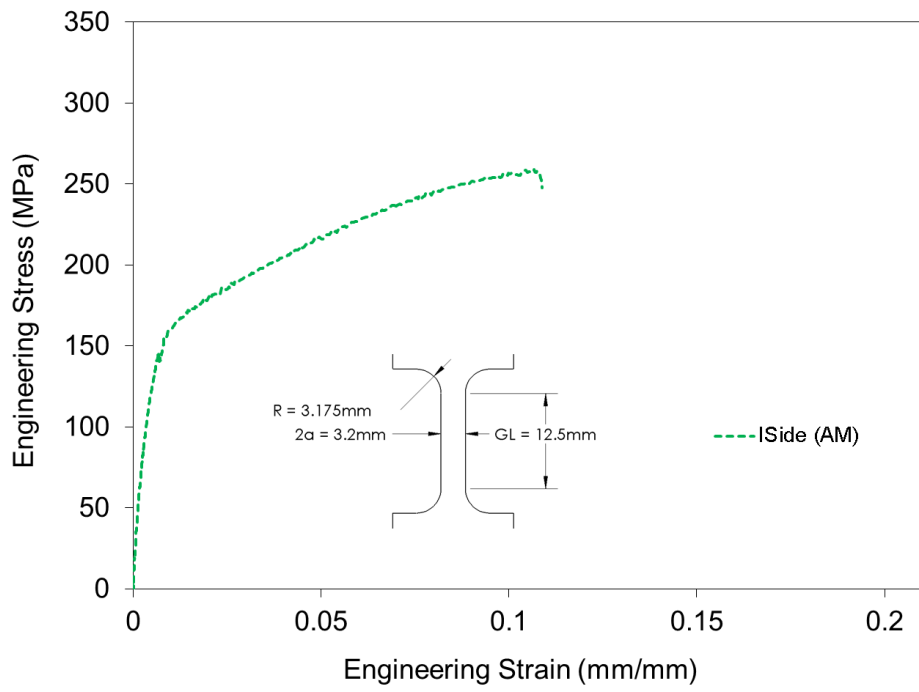
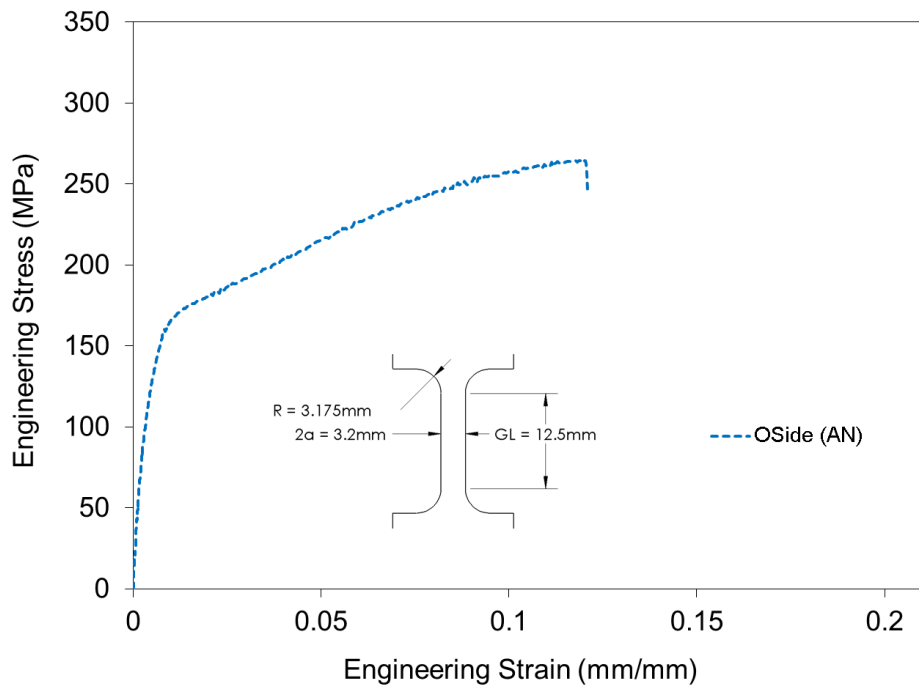


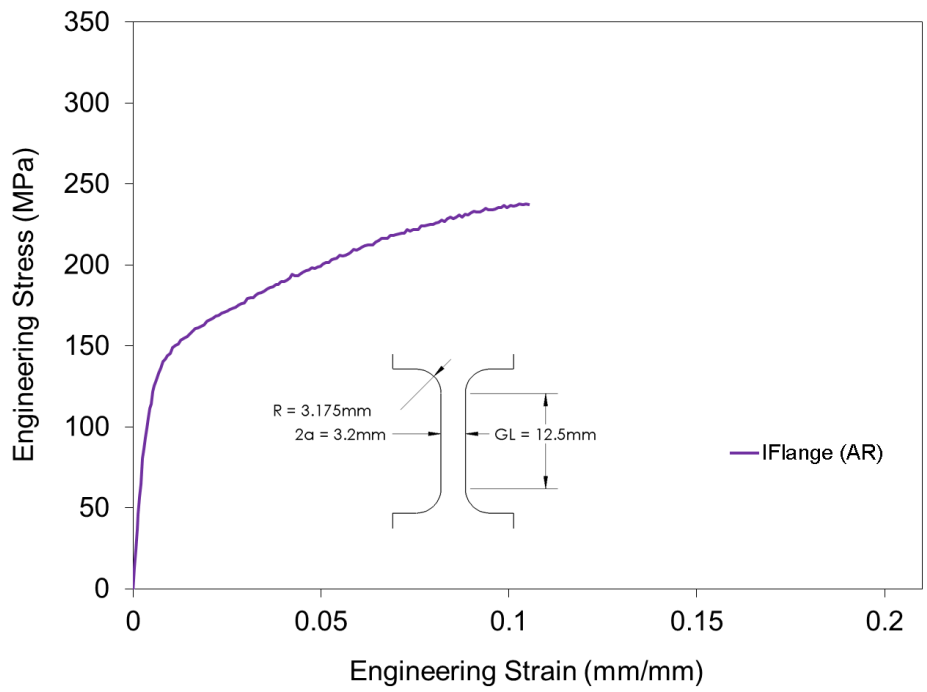
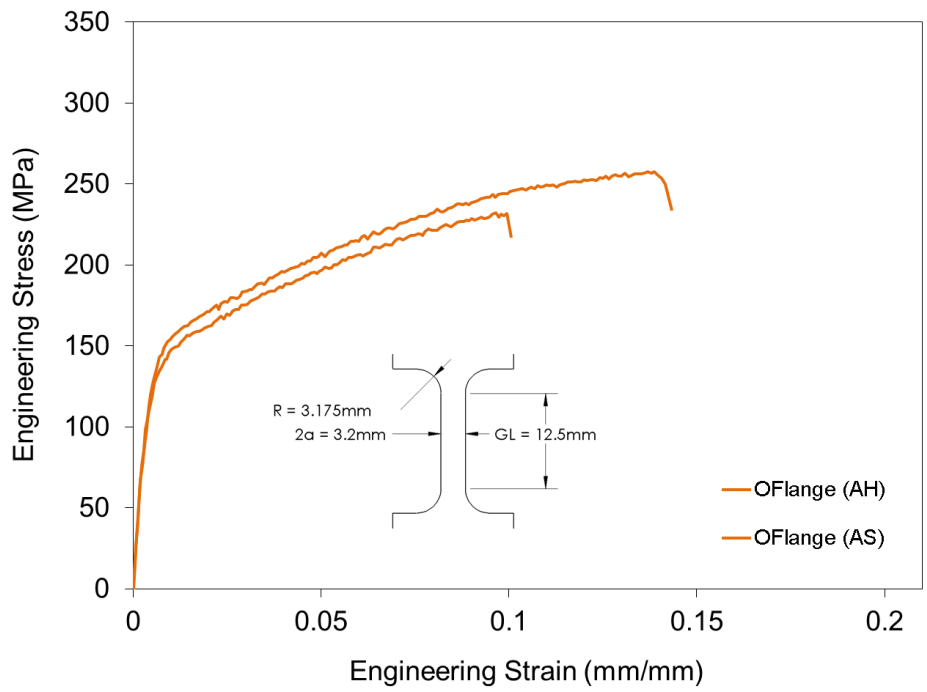
0° uniaxial, Phase I, top location, 10 s⁻¹

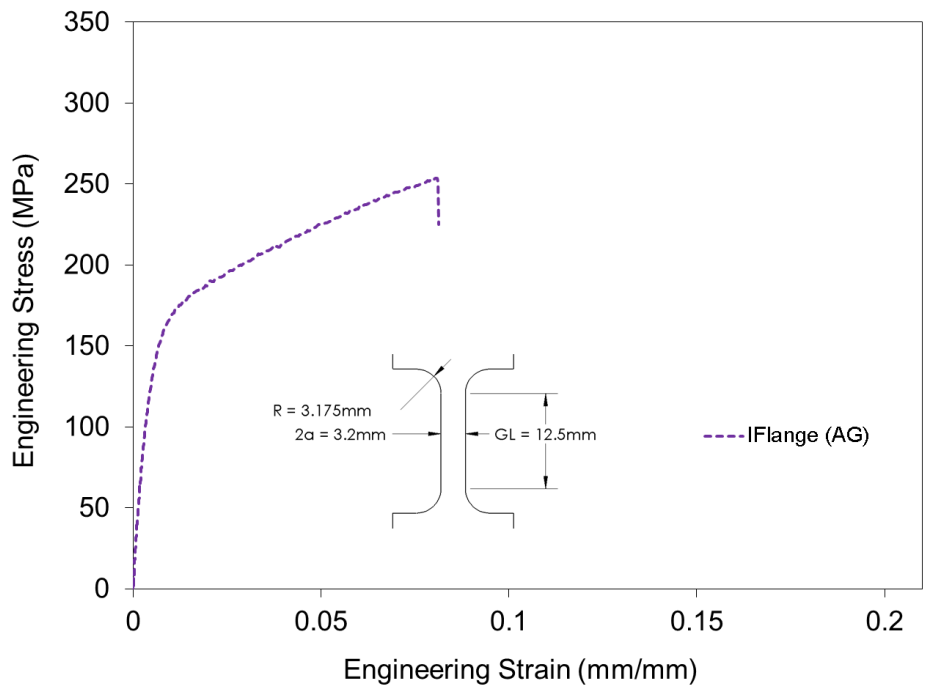


0° uniaxial, Phase I, non-top location stress-strain curves (Strain rates: Solid – 0.001 s⁻¹, Dashed – 10 s⁻¹)

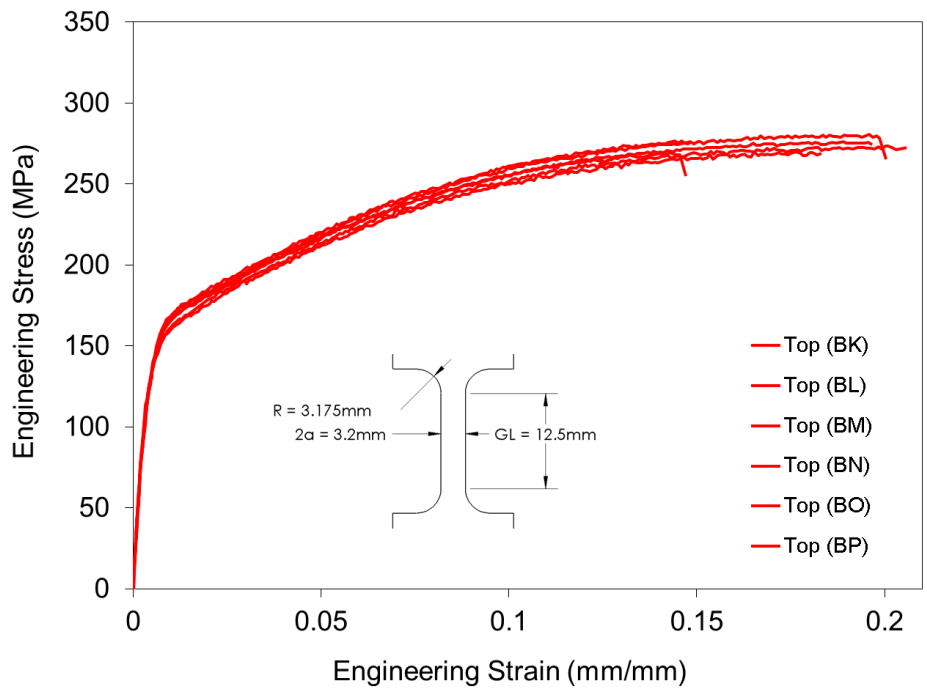




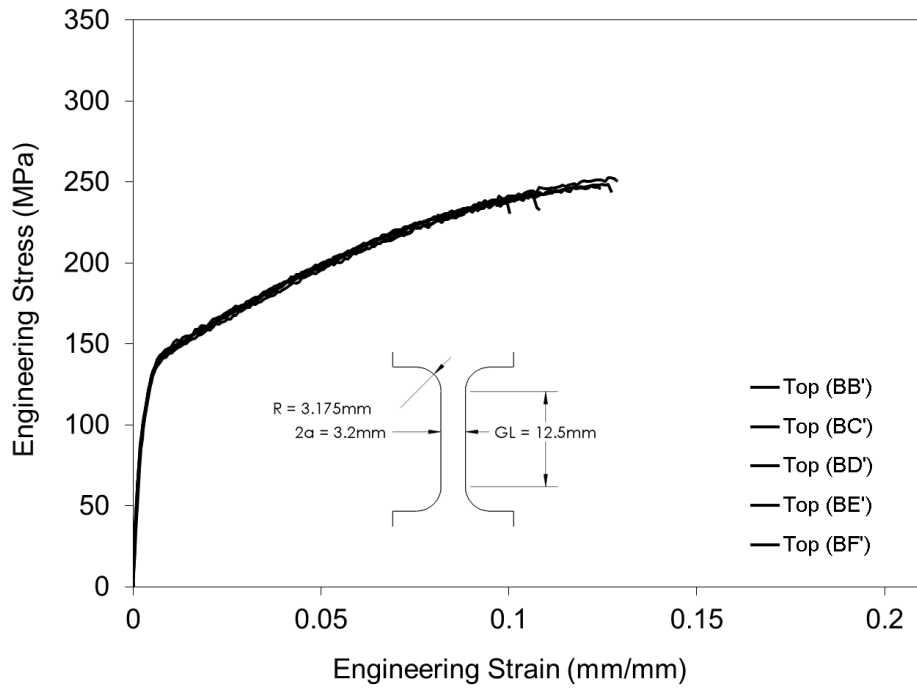




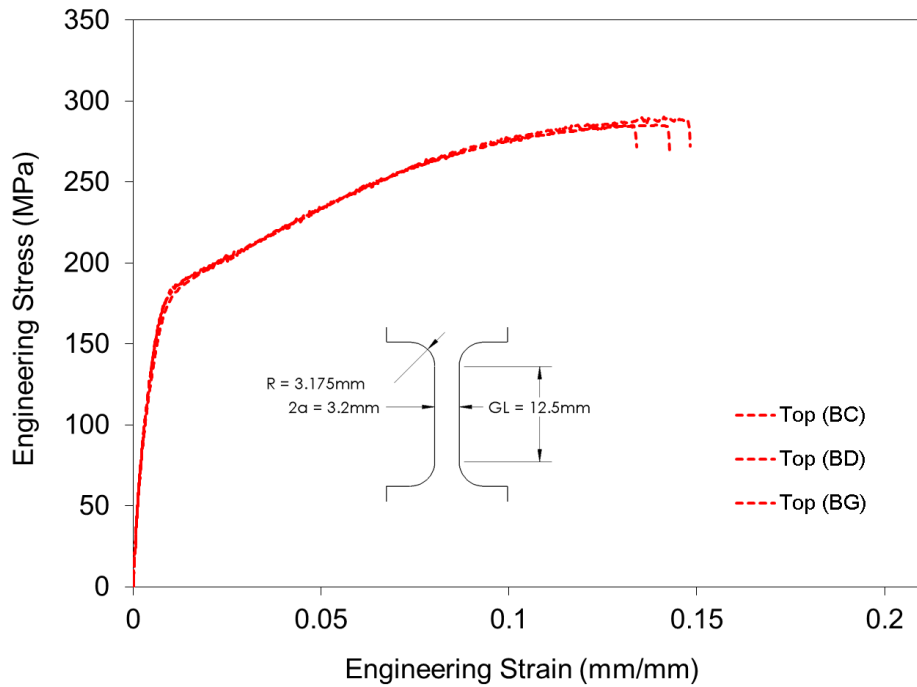
90° uniaxial, Phase I, top location, 0.001 s⁻¹



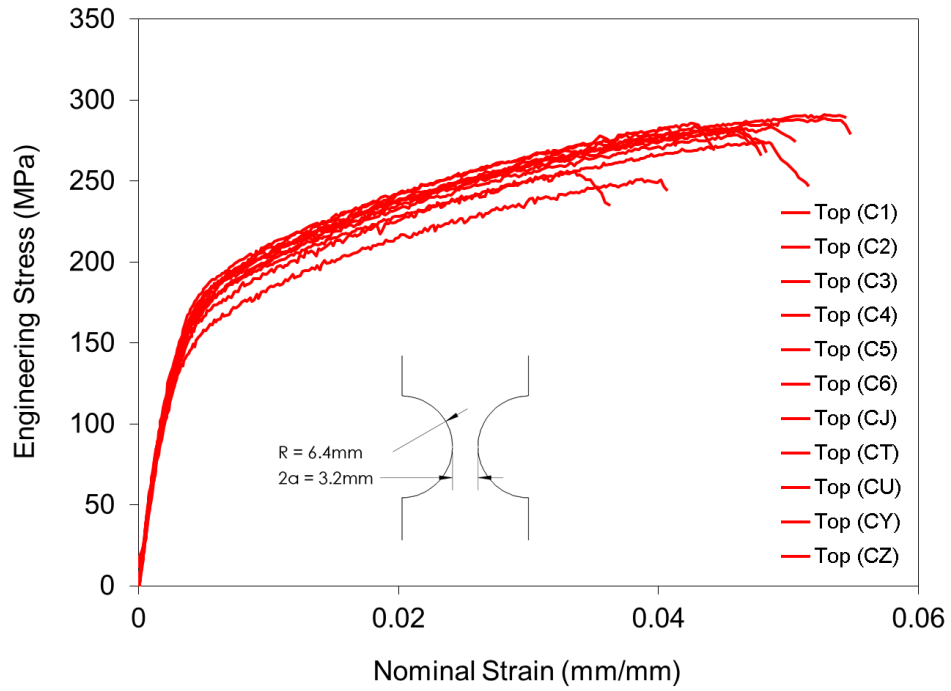
90° uniaxial, Phase II, top location, 0.001 s⁻¹



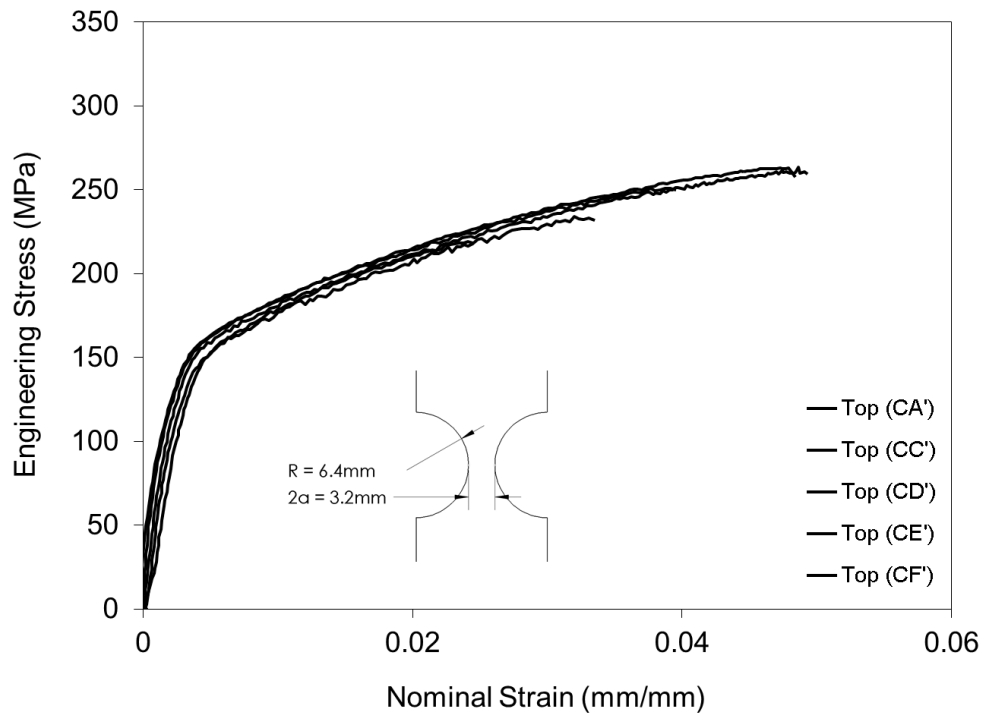
90° uniaxial, Phase I, top location, 10 s⁻¹



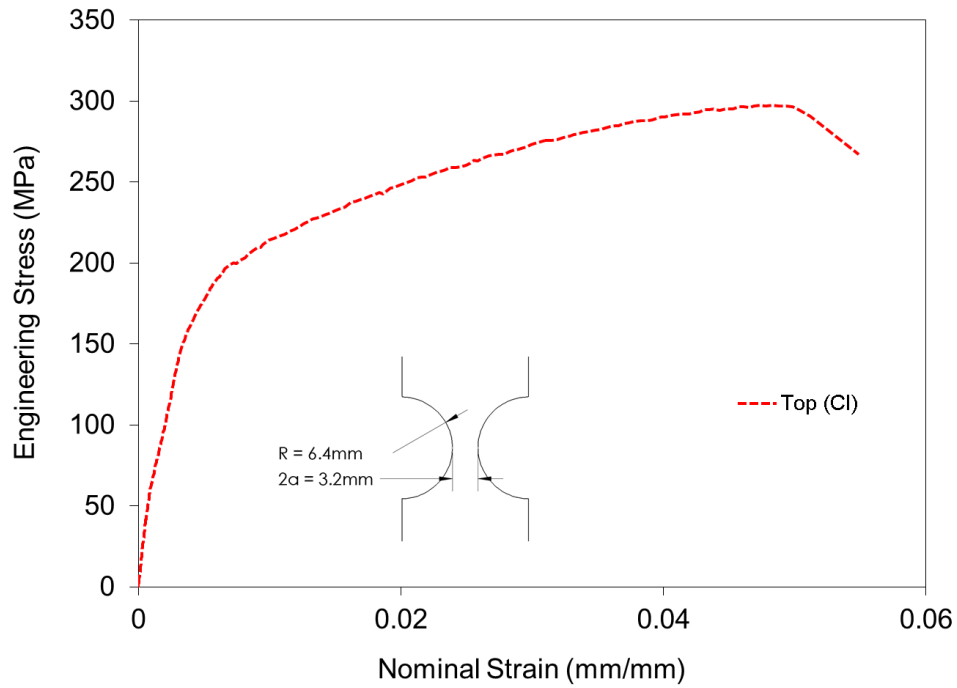
0° a/R=0.25, Phase I, top location, 0.001 s⁻¹



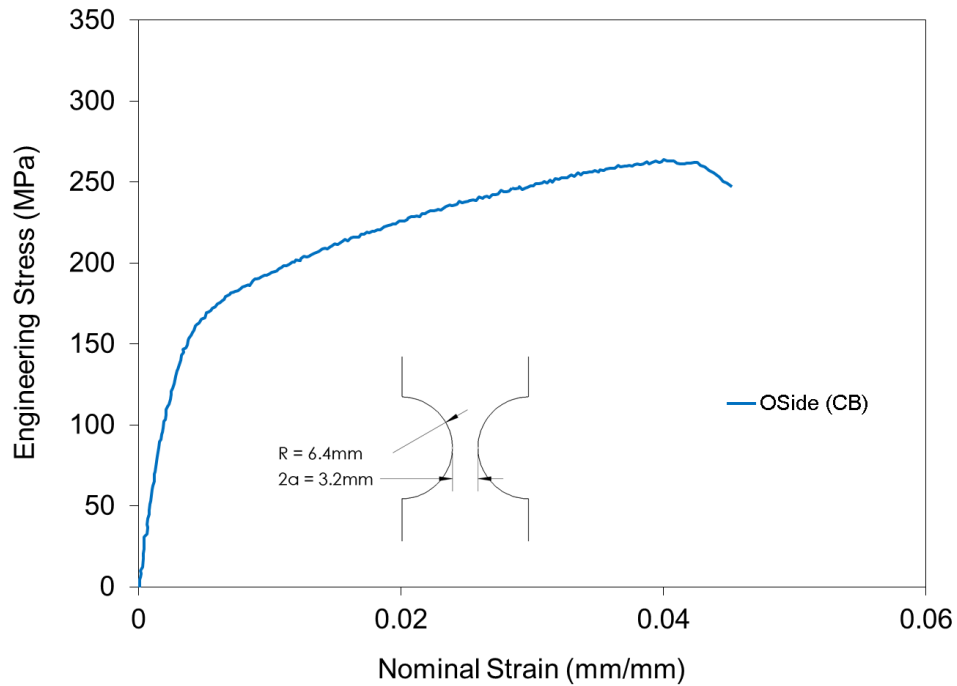
0° a/R=0.25, Phase II, top location, 0.001 s⁻¹

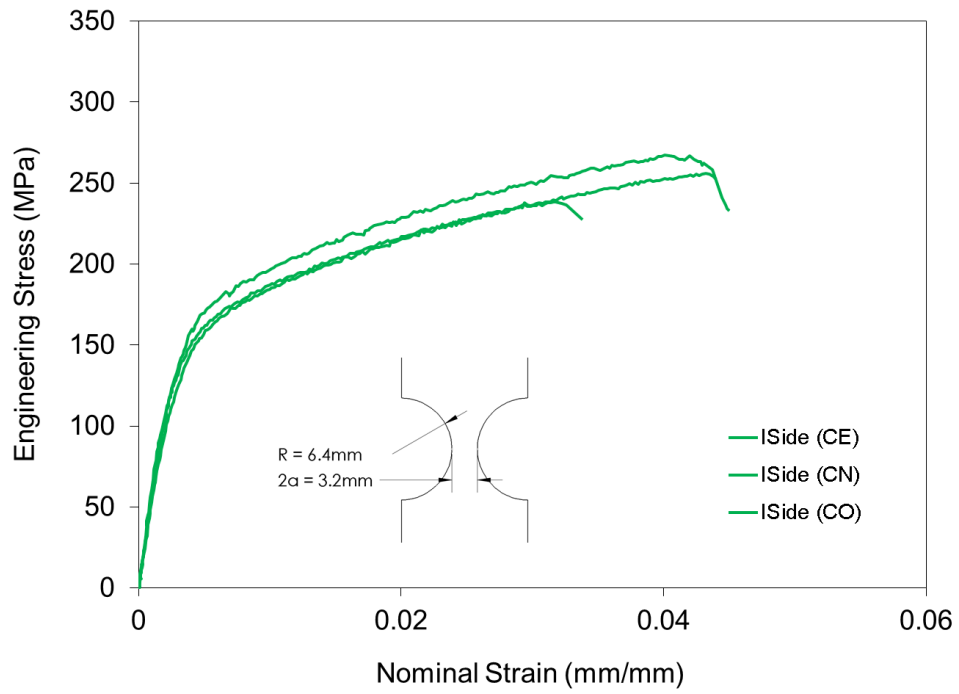
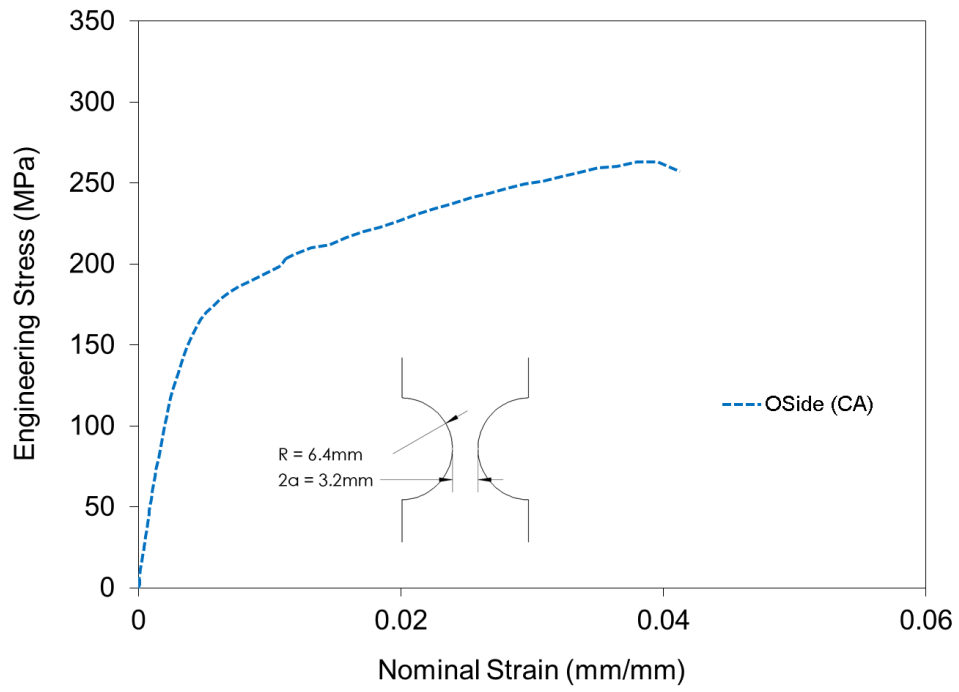


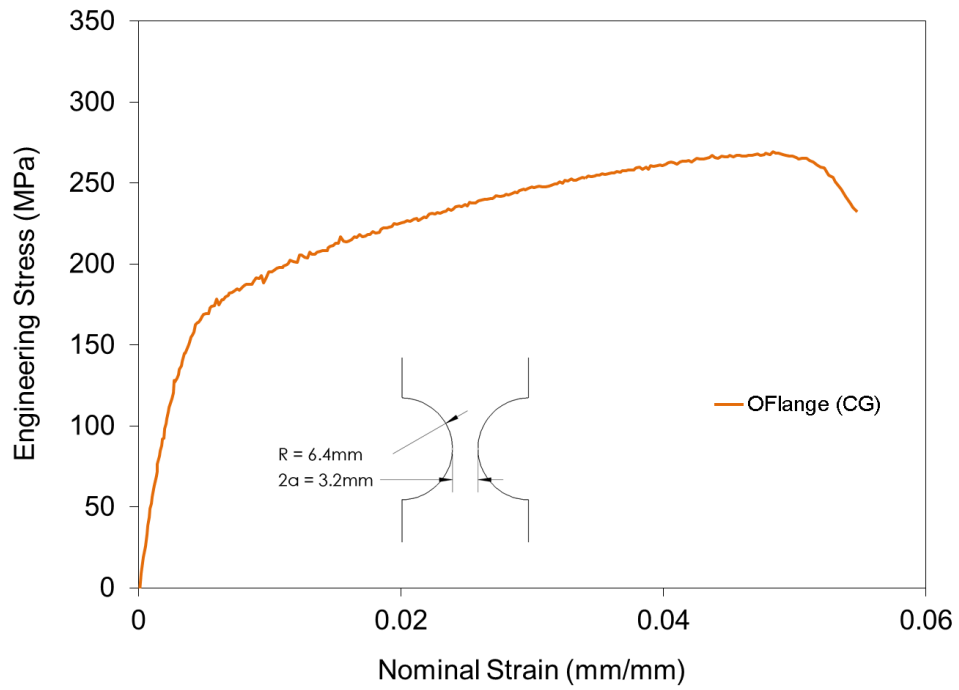
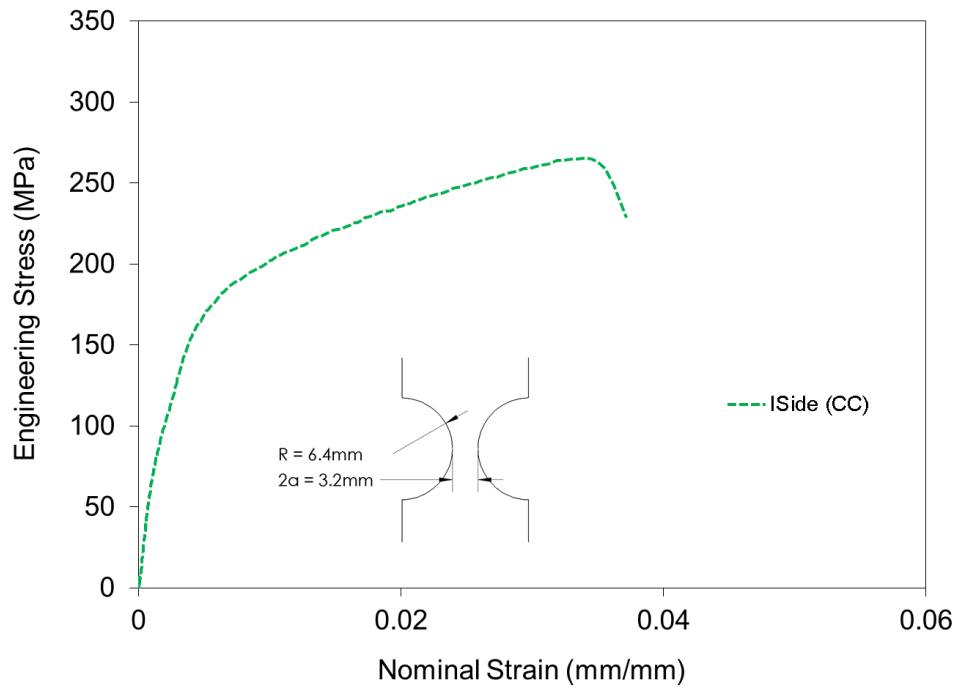
0° a/R=0.25, Phase I, top location, 10 s⁻¹

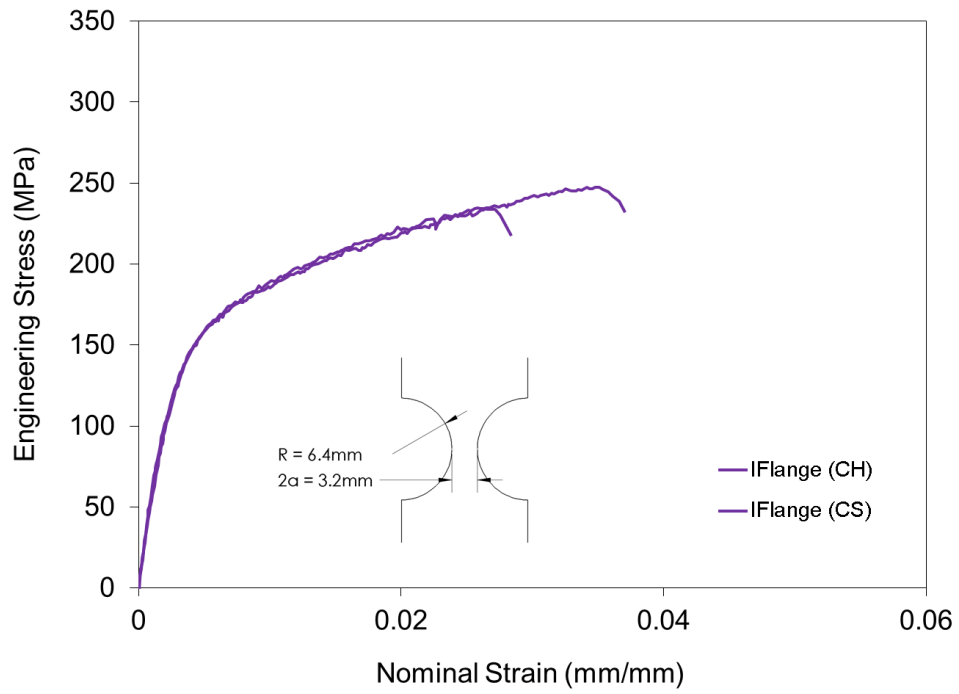
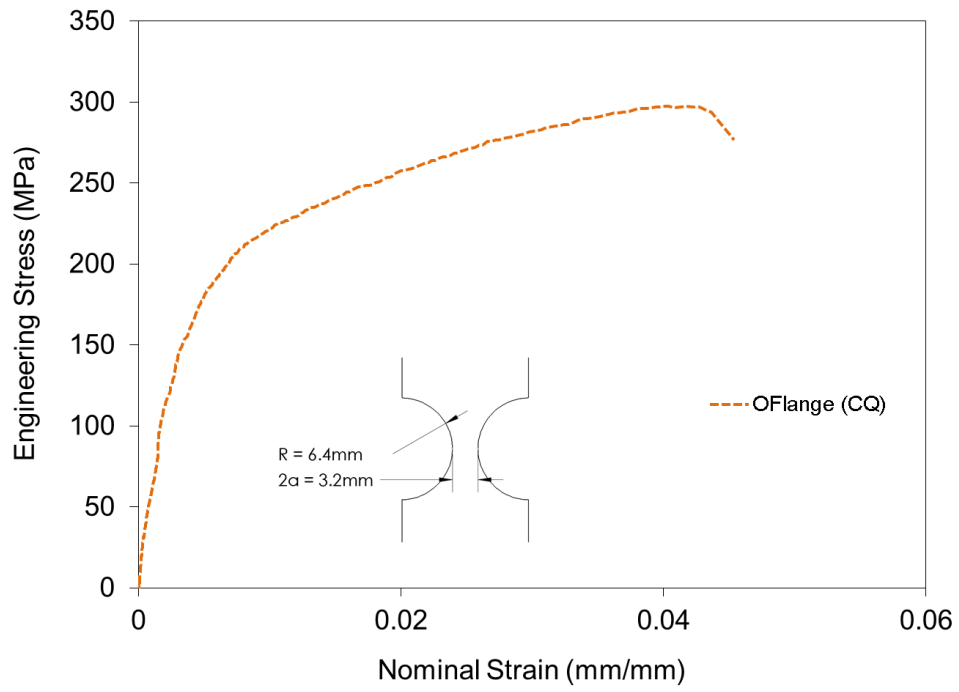


0° a/R=0.25, Phase I, non-top location stress-strain curves (Strain rates: Solid – 0.001 s⁻¹, Dashed – 10 s⁻¹)

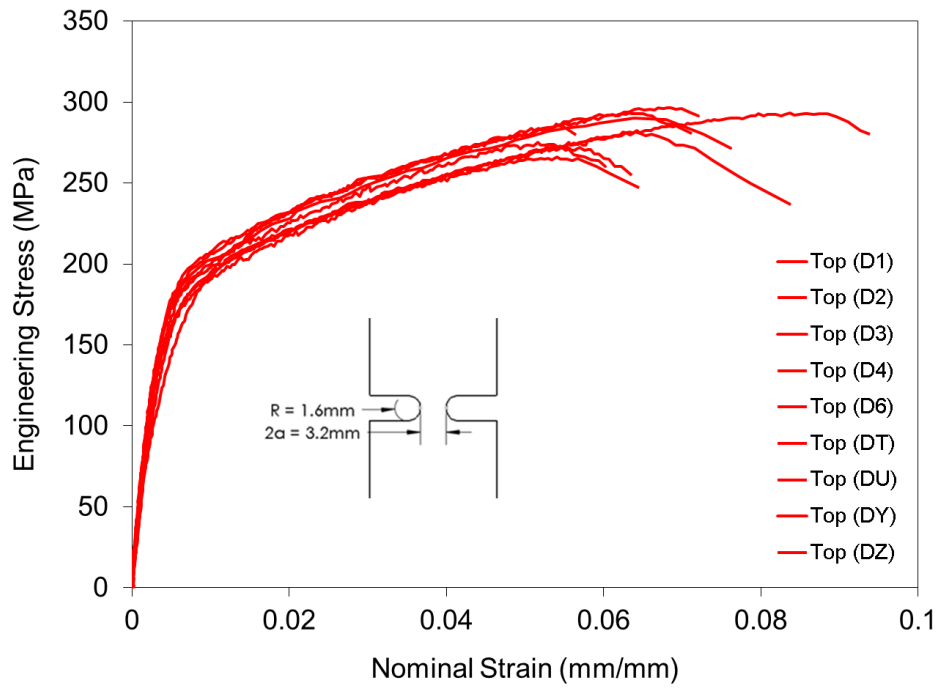




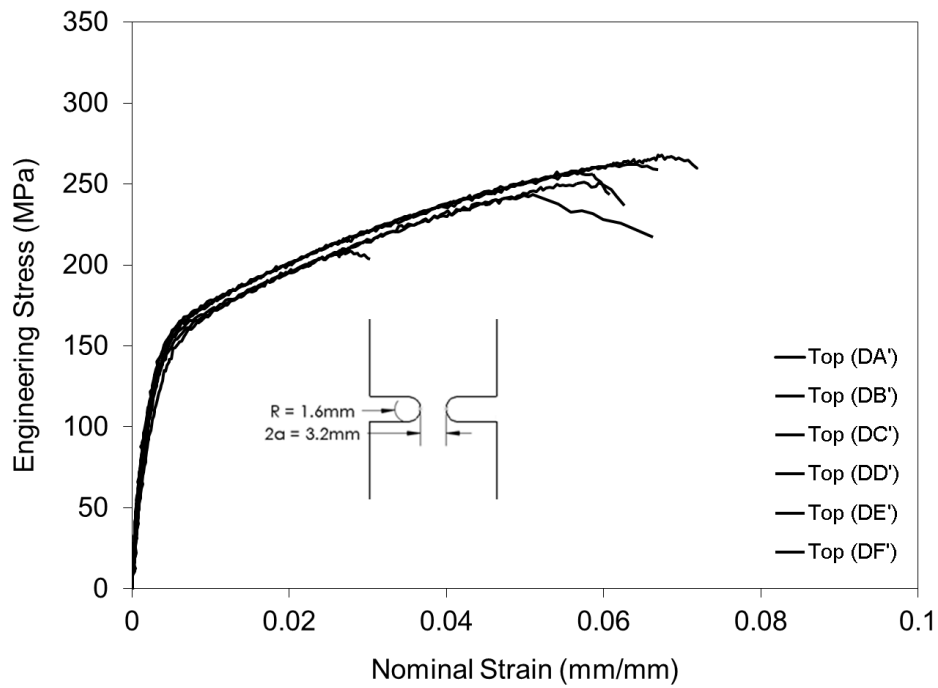




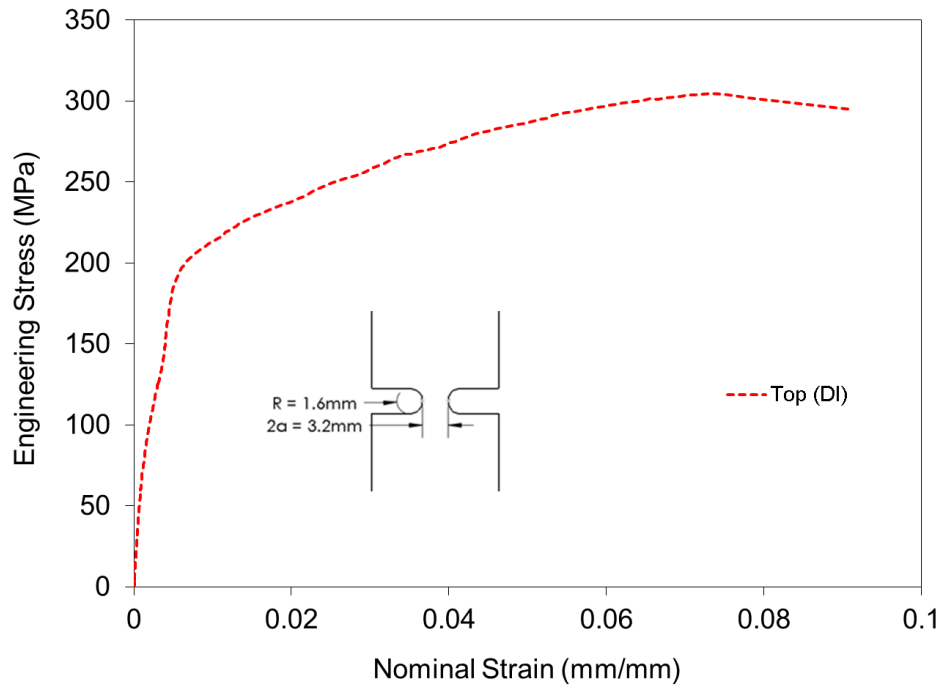
0° a/R=1, Phase I, top location, 0.001 s⁻¹



0° a/R=1, Phase II, top location, 0.001 s⁻¹



0° a/R=1, Phase I, top location, 10 s⁻¹



0° a/R=1, Phase I, non-top location stress-strain curves (Strain rates: Solid – 0.001 s⁻¹, Dashed – 10 s⁻¹)

